MODELING THE IONIZING RADIATION ENVIRONMENT IN EARTH'S ATMOSPHERE

By

PAUL EDWARD INMAN

Bachelor of Science in Physics and Mathematics
Oklahoma Baptist University
Shawnee, OK
2014

Master of Science in Medical Physics
University of Oklahoma Health Sciences Center
Oklahoma City, OK
2016

Submitted to the Faculty of the
Graduate College of the
Oklahoma State University
in partial fulfillment of
the requirements for
the Degree of
DOCTOR OF PHILOSOPHY
May, 2021

MODELING THE IONIZING RADIATION ENVIRONMENT IN EARTH'S ATMOSPHERE

Dissertation Approved:

Dr. Eric Benton

Dissertation Adviser

Dr. Mario Borunda

Dr. John Mintmire

Dr. Ranji Vaidyanathan

ACKNOWLEDGEMENTS

First and foremost, I give glory to God alone for any accomplishments during my time at Oklahoma State University and in all other areas of my life. Many of my scientific questions began as theological ones, and this remains the primary driving factor of my interest in science. The Christian community around me has been a tremendous encouragement throughout my studies. Specifically, I would like to thank my parents for their support throughout my years in graduate school. I would also like to thank Brad Collier, his family, and the Bible study group he hosts for being a source of spiritual guidance and encouragement. Dr. Erik Clary has been another spiritual mentor, and I have deep respect for his well-considered commitment to the truth. Many other friends have been at my side throughout, and I am thankful for them all.

I would like to thank my advisor Dr. Eric Benton for his mentorship and financial support throughout my studies. I likewise thank Dr. Mario Borunda, Dr. John Mintmire, and Dr. Ranji Vaidyanathan for serving on my committee. Dr. Kyle Copeland and Dr. Brad "Buddy" Gersey also deserve thanks for mentoring me during my work. Art and Barb Lucas have been very helpful in providing feedback and insight into my research. I am also thankful for the other past and present members of the Benton research group, Dr. Oliver Causey, Dr. Bryan Hayes, Dr. Rajesh Panthi, Martin Yang, Tristen Lee, and Conner Heffernan. Lastly, thank you to the Oklahoma State University Physics Department, the Federal Aviation Administration, and Los Alamos National Labs.

Name: PAUL EDWARD INMAN

Date of Degree: MAY, 2021

Title of Study: MODELING THE IONIZING RADIATION ENVIRONMENT IN EARTH'S ATMOSPHERE

Major Field: PHYSICS

Abstract: The constant bombardment of the Earth by cosmic radiation leads to an atmospheric radiation environment comprised of many species of energetic secondary particle. Aside from carrying out full Monte Carlo simulations from scratch, no software models currently exist for use to investigate the nature and composition of the ionizing radiation environment, e.g., secondary neutron, electron, positron, and heavy charged particle spectra, as functions of altitude, geomagnetic latitude, time, etc. The FAA has developed a publicly available program, CARI-7, for use in estimating biologically relevant quantities, such as ambient dose equivalent and effective dose, during air travel. CARI-7 is based on extensive simulations of cosmic ray air showers in the atmosphere using the MCNPX radiation transport code, and the MCNPX output files contain secondary particle spectral data. The focus of this research was the development of the Atmospheric Ionizing Radiation Environment Code (AIREC) that uses data from these MCNPX simulations to generate a detailed picture of the structure of the radiation environment in the atmosphere. AIREC takes as inputs global coordinates, a date of interest, and a particle of interest, and returns the corresponding flux energy spectrum. This provides a tool for calculating energy spectra for secondary particles of interest that would be impractical or impossible to measure experimentally. Outputs from AIREC were used as source particles in further MCNP simulations to model radiation detector response to atmospheric radiation.

TABLE OF CONTENTS

Chapter Page

Chapter Page

LIST OF TABLES

Table Page

Table Page

LIST OF FIGURES

Figure Page

Figure Page

Figure Page

Figure Page

CHAPTER I

Introduction

1.1. Overview of Problem

The Earth is constantly being bombarded by ionizing radiation from space. The majority of this radiation originates outside of the Earth's solar system but within the galaxy, and the energetic particles comprising this radiation are referred to as galactic cosmic rays (GCR). These GCR are fully ionized nuclei, the vast majority of which are protons and alpha particles, and generally the heavier the nucleus the rarer it is. GCR enter the top of the Earth's atmosphere, and as they travel through the atmosphere, they undergo nuclear interactions with the nuclei of the air molecules present in the atmosphere, producing additional energetic particles referred to as secondary particles. These secondary particles undergo further interactions, producing additional secondary particles, leading to a particle cascade, also referred to as an extensive air shower (EAS). As an EAS propagates towards the surface of the Earth it increases in size both in terms of volume and total particle number, and the flux at a given altitude initially increases. However, as the initial energy of the GCR primary particle is divided amongst more and more particles, the average kinetic energy of a particle of an EAS falls below the energy required to produce additional secondary particles. This results in the flux of particles of an EAS peaking at an altitude of about

20 kilometers on average, then decreasing as the EAS continues towards the surface of the Earth. As a nearly constant GCR flux is incident on the Earth's atmosphere, many such EAS are present in the atmosphere at any given moment. Together, these EAS produce an ionizing radiation environment consisting of many species of particles across a spectrum of energies in the Earth's atmosphere. For a given location in the atmosphere, these energetic secondary particles have an approximately constant flux when averaged over the course of minutes to hours. This constant flux of secondary particles in the atmosphere is referred to throughout this thesis as the steady state atmospheric ionizing radiation environment (SSAIRE).

The SSAIRE varies as a function of global coordinates (latitude, longitude, and altitude) and solar epoch. Few experiments have been conducted to measure the average behavior of the SSAIRE. Likewise, few computer simulations have been run to study the SSAIRE, and no comprehensive model exists. This lack of knowledge regarding the SSAIRE led to the following research goal: To develop a tool that returns the secondary particle flux given coordinates on the globe, a date, and particle(s) of interest and to analyze the behavior of the flux as these inputs varied. This goal was in large part fulfilled by the development of the software Atmospheric Ionizing Radiation Environment Code (AIREC). AIREC takes as inputs user supplied latitude, longitude, altitude, date, and particle of interest and returns the secondary flux spectrum corresponding to the user inputs. The secondary particle flux has units of

$$\frac{secondary\ particles}{cm^2\ s},$$

and a secondary flux spectrum is formed by dividing the flux into energy bins.

While the SSAIRE has not been studied in detail, cosmic ray physics does have a long and rich history. Cosmic ray physics research has broadly fallen under one of two categories: high energy cosmic ray physics research and radiation safety. A brief review of these fields will provide context for this research and contrast between the typical aims of cosmic ray physics research and the goal of this research. Additionally, data generated from cosmic ray radiation safety research paved the way for the goal of this research to be met.

1.2. Past and Current Cosmic Ray Physics Research

GCR were first discovered in 1912 by Victor Hess [Hess, 1912]. High energy GCR and the particles they produce in the atmosphere have been the topic of much study since that time. In 1932 Carl Anderson’s study of GCR using a cloud chamber lead to the discovery of positrons [Anderson, 1932]. Anderson continued his research of GCR using cloud chambers, and in 1937 he and Seth Neddermeyer discovered muons [Neddermeyer and Anderson, 1937]. In 1938, Pierre Auger’s experiments with coincidence detectors in the atmosphere confirmed that GCR produce EAS [Auger et al., 1939]. In 1947, a group at the University of Bristol, including Cecil Powell, César Lattes, Giuseppe Occhialini, and others, discovered charged pions during GCR experiments using a photographic emulsion technique of detection [Lattes et al., 1947]. In the same year, Clifford Butler and George Rochester discovered the kaon (K meson) during their GCR experiments using cloud chambers [Rochester and Butler, 1947].

In recent years, most novel particle discoveries have resulted from particle accelerator experiments [DONUT Collaboration, 2001; ATLAS Collaboration 2012]. High energy GCR physics remains of interest in part because no particle accelerator can produce particles with nearly as much energy as GCR. The highest energy collisions produced by particle accelerators are 13 TeV [LHC, 2018], but a $(3.2\pm0.9)\times10^8$ TeV GCR was detected in the Fly’s Eye air shower detector, which at the time was the highest energy particle ever detected [Bird et al., 1995]. Currently, high energy cosmic ray physics typically focuses on cosmic rays with energies above 1 TeV. These cosmic rays and their EAS are studied in order to determine where they originated and by what mechanisms. In one of the IceCube collaboration’s experiments, incident cosmic ray directional data was collected from cosmic rays in the TeV to PeV energy range over a period of 6 years. This data was studied to determine the amount of anisotropy in the arrival direction of cosmic rays and what physical processes may be responsible for this anisotropy [Aartsen et al., 2016]. Another group, the Pierre Auger Collaboration, determined that some of the highest energy cosmic rays ($\geq 8\times10^{18}$ eV) have anisotropy in their arrival directions, suggesting extragalactic origins [The Pierre Auger Collaboration, 2007; The Pierre Auger Collaboration, 2017]. The Pierre Auger Cosmic Ray Observatory is currently the world's largest cosmic ray observatory [The Pierre Auger Collaboration, 2015].

The high energy GCR typical of cosmic ray physics research are responsible for many interesting phenomena and are worthy of study. However, these extraordinarily energetic GCR are too rare to consistently contribute to the SSAIRE. The GCR in the energy ranges that are responsible for the GCR are rarely studied, however there are a few groups that have worked to determine the incident GCR energy spectrum, including the International Organization for Standardization (ISO) [ISO, 2004], Badhwar and O'Neill [O'Neill, et al., 2015], and the German Aerospace Center [Matthiä et al., 2013]. The models developed by each of these groups will be further discussed in Chapter 2.

The focus of cosmic ray research for radiation safety purposes is the determination of biologically relevant quantities that result from atmospheric radiation. Such quantities include the absorbed dose and effective dose, which are generally calculated by computer codes that take as inputs a time and geographic location(s). In the production of these radiation dose calculation programs, fundamental physics quantities were calculated, namely the flux energy spectra of various species of particles present in the atmosphere. Fluence to dose conversion factors were applied to this fundamental physics data to calculate biologically relevant quantities. The foremost American code of this kind is CARI-7, which was developed at the Federal Aviation Administration (FAA) by Dr. Kyle Copeland [Copeland, 2017]. CARI-7 was developed from data resulting from numerous simulations conducted using the Monte Carlo radiation transport code Monte Carlo N Particle X (MCNPX) [Copeland, 2017].

1.3. This Research as Distinct from Other Cosmic Ray Research

Neither high energy cosmic ray research nor radiation safety cosmic ray research focus on the fundamental physics of the SSAIRE. Cosmic rays of energy 1 TeV and greater are the focus of high energy cosmic ray physics research, but the vast majority of EAS are generated by GCR with energy ranging from 1 MeV to 1 TeV. Thus, typical high energy cosmic ray research ignores the average behavior of the SSAIRE in favor of studying extraordinary phenomena.

Radiation safety research calculates fundamental physics quantities, but this data is used only as a means to an end, namely the calculation of biologically relevant quantities. Despite the fact that the complicated radiation environment present in the atmosphere is a longstanding problem, there remain significant gaps in fully understanding it.

In contrast, the research of interest in this thesis is that of the average behavior of the SSAIRE. Two approaches to determining the energetic particle flux in the atmosphere as a function of coordinates and date were considered for this project. One of the considered approaches was an experimental approach, which would require collecting secondary particle flux data for all particle species of interest at a variety of coordinates and dates and interpolating this data to determine the secondary particle flux at coordinates and dates for which no measurements were made. The other considered approach was a computer model approach, which would require running computer simulations of the SSAIRE and recording the simulated secondary particle flux data. Interpolations to determine the secondary particle flux at coordinates and dates for which no simulations were run could be conducted as with the experimental approach.

Unfortunately, most experiments to measure EAS due to ≤1 TeV cosmic rays range from impractical to effectively impossible. For example, there are many challenges to determining the secondary proton flux at an altitude of 40 kilometers. At this altitude the secondary proton flux is low and would require months of constant measurements to acquire statistically significant data. The detector used in such measurements would need to be capable of discriminating between protons and other charged particles. Additionally, the detector would have to be able to distinguish between protons of varying energies. Such a detector would be large and require a flight apparatus capable of maintaining its position for the months needed to collect data. Such an experiment would only yield the secondary proton spectrum for that time and location. Because the secondary particle flux is a function of global coordinate and solar epoch, the experiment would need to be repeated for different particle species, altitudes, latitudes, longitudes, and dates in order to gain a clear understanding of the SSAIRE. With these obstacles in conducting experiments, the most viable solution for the study of the SSAIRE is a computer based model.

The MCNPX data used in the development of CARI-7 by Dr. Kyle Copeland was made available for the work of this thesis. This MCNPX data contained secondary particle flux values at several different altitudes due to GCR of different energies and species. For example, the MCNPX data contained the neutron flux spectrum at 30 kilometers due to a single 100 GeV GCR proton. While the FAA used this data for the calculation of biologically relevant quantities in order to understand the risks to frequent fliers, there remained untapped data on the secondary particle flux present in the atmosphere. This previously untapped fundamental physics data was repurposed to develop AIREC.

1.4. Potential Applications of AIREC

The AIREC output secondary flux spectrum can be used in the study of a number of practical problems. For example, in the field of avionics, a common objective is to determine is to quantify the probability of electronic failure due to incident radiation [Zaczyk, 2013]. Ionizing radiation is capable of interacting with a single transistor, flipping its state, which can cause total electronic failure [Nowicki, 2017]. Radiation interaction with circuitry can also permanently burn out a transistor. Such errors are referred to as single event effects [Zaczyk, 2013; Dyer and Truscott, 1999]. The error rate is proportional to the ionizing radiation flux [Cooper, 2012], hence AIREC output spectra could be used in modeling the failure rate of electronic equipment.

The Irradiation of Chips and Electronics (ICE) House at the Los Alamos Neutron Science Center (LANSCE) has a neutron beam that mimics the shape of the cosmic ray secondary neutron spectrum at aircraft altitudes, but with an intensity that is orders of magnitude larger. How much more intense the LANSCE beam is than atmospheric neutrons depends upon the global coordinate being considered. The LANSCE beam allows equipment to be exposed to several years' worth of naturally occurring cosmic ray induced neutron flux in less than an hour [Nowicki, 2017]. Using the facility's neutron beam, tests have been conducted to measure the error rate on printed circuit boards [Wender, 2019]. A comprehensive model of secondary neutron spectra would give electronic component manufacturers and users a more precise expectation of device error rate for a given location and time of use.

Radiation detectors have variable detection efficiency depending on the particle species and particle energy [Tsoulfanidis, 1995; Knoll, 2010]. Typically, a detector is calibrated using sources with known particle type and energy. In experiments to measure the radiation present in the atmosphere knowing the particle species present and the energy of those particles allows for better interpretation of the detector response, and this information is provided by AIREC.

As with radiation detectors, the effectiveness of radiation shielding materials depends upon the particle species and particle energy. For example, lead is one of the best materials for shielding charged particles, but there are much better materials, such as polyethylene, available for shielding neutrons. For high energy particles shielding can actually do more harm than good due to the production of secondary particles within the shielding. These secondary particles may contribute to radiation dose or electronic failure rate than the initial particle. Whether shielding passengers on an aircraft or electronic equipment, knowing the radiation present informs the decision on how or whether to shield and how effective that shielding will be.

The AIREC output spectra can also be used as inputs in radiation transport models, particularly Monte Carlo simulations. Monte Carlo simulation will be discussed in more detail in later chapters, but in brief, the Monte Carlo method of radiation transport is a method of simulating the movement of energetic particles through matter. A secondary particle flux energy spectrum produced by AIREC can be used as a radiation source in radiation transport models of the irradiation of radiation detectors, electronics, shielding materials, or the human body.

Another motivation for modeling the secondary electron spectrum is the potential insight into lightning initiation. It was believed that the flux of cosmic ray secondary particles was too low to play a role in lightning generation until [Gurevich et al., 1992] proposed that secondary electrons could produce more electrons via an avalanche effect, that is, secondary electrons originating from cosmic rays could be accelerated by the electric field present during a thunderstorm and further ionize the surrounding air, creating more free electrons that will likewise be accelerated and lead to more ionization [Gurevich et al., 1992]. The natural radioactivity (i.e. from terrestrial sources) in the atmosphere produces electrons of neither sufficient number nor energy to explain the x-rays emitted during thunderstorms, giving further credence to the idea that secondary electrons play a vital role in lightning initiation [Lindy, 2018].

Sub-orbital flights are a future step towards space tourism, and the radiation environment encountered during these flights differs significantly from both background radiation on the surface of the earth and the radiation environment typical for commercial airline flights. AIREC can be used to map the radiation environment that would be encountered on such flights.

In an effort to increase global access to the internet and mobile communications, efforts have been made to provide network connections via weather balloons stationed at an altitude of 20 km and outfitted with antennas and electronic equipment [Nagpa, 2017]. One of the challenges involved with the operation of these balloons is the effect of radiation present in the atmosphere [Loon, 2021]. AIREC could be used to calculate the radiation environment that these balloons would encounter.

1.5. Review of Atmospheric Radiation Experiments and Model Simulations

Though study of the SSAIRE has not been undertaken to the same extent as high energy cosmic ray physics and radiation safety, a limited number of studies have been conducted. Neutron ground monitors are present at several different sites including Thule, Greenland. These detectors are used to record neutron flux at the surface of the Earth over the course of several decades. The neutron flux at the surface of the Earth varies with the galactic cosmic ray (GCR) flux at the top of the atmosphere, and the GCR flux at the top of the atmosphere varies inversely with solar activity. Thus, the neutron monitor data can be used to track solar activity.

Bonner sphere spectrometer (BSS) experiments are the primary method of measuring the neutron flux energy spectrum present in the atmosphere. One such neutron spectral experiment using a BSS was conducted at the High Altitude Research Station in Jungfraucjoch, Switzerland by [Mares et al., 2020] in order to determine the secondary neutron spectrum. The research facility is in the mountains 3.585 km above sea level, which has a considerably higher neutron flux than the neutron flux at sea level. A similar experiment was conducted by [Schraube et al., 1997] to determine the secondary neutron spectrum at the summit of Mt. Zugspitze. The results of the BSS measurement were compared to those of a model simulation conducted in the Monte Carlo radiation transport code FLUKA [Schraube et al., 1997]. Another neutron spectral study using a BSS was conducted by [Goldhagen et al., 2004]. In these experiments the neutron spectrum was determined aboard a NASA ER2 flight at an altitude of 20 kilometers, which provided a higher neutron flux than either of the BSS experiments conducted in the mountains.

There have also been studies using model simulations. One such study was conducted by [Lindy et al., 2018] using the CORSIKA Monte Carlo radiation transport code. Simulations were run to determine the secondary electron energy spectrum in the atmosphere at various altitudes above Stillwater, OK. Another set of simulations were conducted by [Ferrari et al., 2001] using the FLUKA Monte Carlo radiation transport code. In these simulations the total flux versus altitude was determined for each of protons, electrons, photons, muons, pions, and neutrons with varying geomagnetic field strengths and solar activities.

Each of these studies is analyzed in more detail and compared to the results of Atmospheric Ionizing Radiation Environment Code (AIREC), the code developed for this thesis, in Chapter 5.

CHAPTER II

REVIEW OF THE PHYSICS UNDERLYING THE ATMOSPHERIC IONIZING RADIATION ENVIRONMENT

Due to the constant flux of galactic cosmic rays (GCR) incident on the top of the Earth's atmosphere, for a given location within the atmosphere (latitude, longitude, altitude) there exists a steady state atmospheric radiation environment (SSAIRE) over time periods on the order of minutes to hours. The interactions of primary GCR particles with atmospheric air nuclei produce secondary particles, and these secondary particles can undergo further interactions, producing additional secondary particles. The primary particles as well as the much more numerous secondary particles compose the SSAIRE. This chapter discusses the nature of these primary and secondary particles, factors affecting the intensities of these particles, and the models used to represent these physical phenomena in AIREC.

2.1. Galactic Cosmic Rays

GCR were first discovered in 1912 by Victor Hess when he placed electroscopes on balloon flight experiments and found an increase in ionization as the altitude increased from the surface of the Earth, indicating that the cause of the ionization was of extraterrestrial origin [Rao et al. 1998, Blasi 2011]. After Hess's discovery many other scientists became interested in cosmic ray studies and one group found that after the initial increase in ionization with altitude the ionization began to decrease at still higher altitudes, thus showing a peaked ionization versus altitude curve. The maximum level of ionization displayed by this curve is now known as the Pfotzer maximum [Regener, 1933; Carlson and Watson, 2014].

The majority of GCR particles are believed to originate outside the solar system, but within the galaxy and are thought to be accelerated by supernovae remnants (SNR) [Beatty, 2017; Blasi, 2011; Drury, 2012]. However, there is ambiguity as to where and how exactly GCR originate. GCR particle trajectories cannot be traced back to a specific SNR, as the interstellar magnetic field deflects the GCR, removing information as to their origin. As a result of this interstellar magnetic deflection, upon arrival at Earth, the GCR intensity is nearly isotropic [Amenomori et al., 2006]. The small amount of anisotropy in the arrival of a small number of high energy GCR particles ($> 8 \times 10^{18}$ eV) at Earth has been measured and indicates that these particles actually have extragalactic origin [Auger Collaboration, 2017]. Other possible sources of GCR particles include neutron star collisions [Kimura, 2018], gamma-ray bursts [Mészáros, 2006], and the interacting winds of massive stars [Aharonian, 2019].

Figure 2.1 displays the GCR energy flux spectrum. On the log-log plot there is an approximately linear relationship between the flux and the energy beyond 10^{10} eV with changes in the slope at the knee ($\sim 10^{16}$ eV) and at the ankle ($\sim 10^{18}$ eV). At lower energies the curve plateaus, as less energetic GCR particles are more easily attenuated and deflected by both the solar wind and interstellar magnetic field. It can be seen in the figure that high energy extragalactic particles are rare, reaching the top of Earth's atmosphere at a rate of only about one particle per kilometer squared per year [Cronin, 1999; Auger Collaboration, 2017]. Note that the flux decreases by 32 orders of magnitude as the energy increases by 13 orders of magnitude [Castellina et al., 2013; Cronin, 1999]. At the high end of the energy spectrum, GCR particles are the most energetic particles known in the universe [Cronin, 1999], making them a subject of great interest to astrophysicists. However, because of the rapid decrease in GCR intensity with increasing GCR energy, high energy GCR particle contribution to the SSAIRE is negligible. Thus for this work, primary GCR energies above 10^{12} eV were not considered. This energy corresponds to approximately one particle per meter squared every three hours.

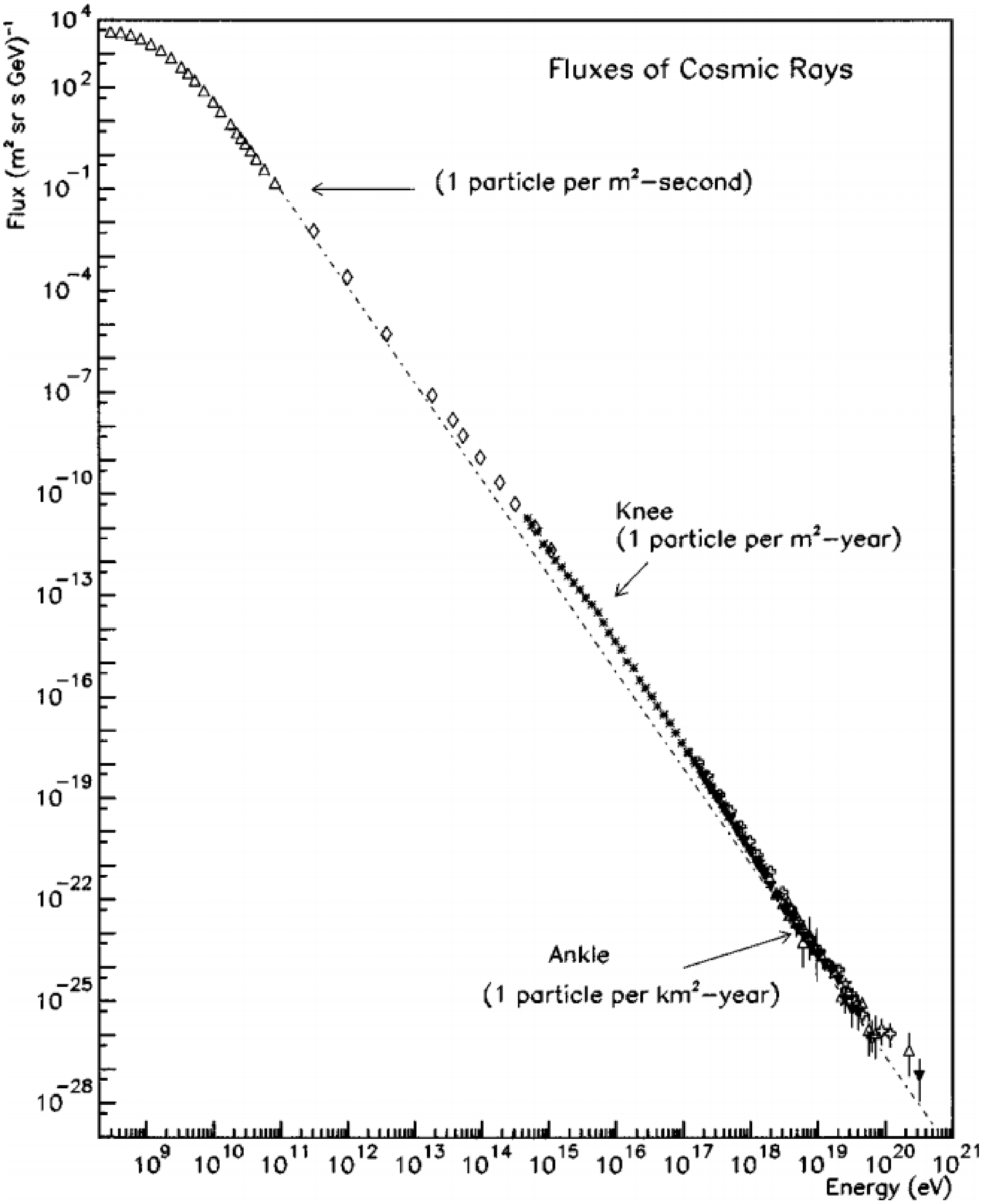

Figure 2.1: The GCR primary flux versus energy [Cronin, 1999].

The majority of the GCR primary particles are fully ionized nuclei. On arrival at Earth GCR primary particles are composed of 85% protons, 12–14% α-particles, and 1% heavier nuclei ($Z \geq 3$) [Benton, 2001; Copeland, 2014]. With exceptions, the heavier the nucleus, the rarer it is. Although the nuclei heavier than alpha particles comprise only 1% of the total GCR flux, they are responsible for producing a significant number of secondary particles, and the heavy nuclei up to iron are included in the GCR flux considered in this work. Figure 2.1 displays the GCR flux for various GCR nuclei, demonstrating the general trend of decrease in GCR flux with increasing atomic number. The Figure 2.2 legend displays the various experiments that were conducted to collect the data [Beatty et al., 2019].

There is also an electromagnetic component to the GCR primary particles, including electrons, positrons, and photons. While this electromagnetic component contains vital information for understanding the origins of GCR particles, its contribution to the SSAIRE is negligible [Blasi, 2011], i.e. it does not produce large quantities of secondary particles. As a result of the minimal electromagnetic GCR flux contribution to the SSAIRE, electromagnetic GCR primary particles are not considered in this work.

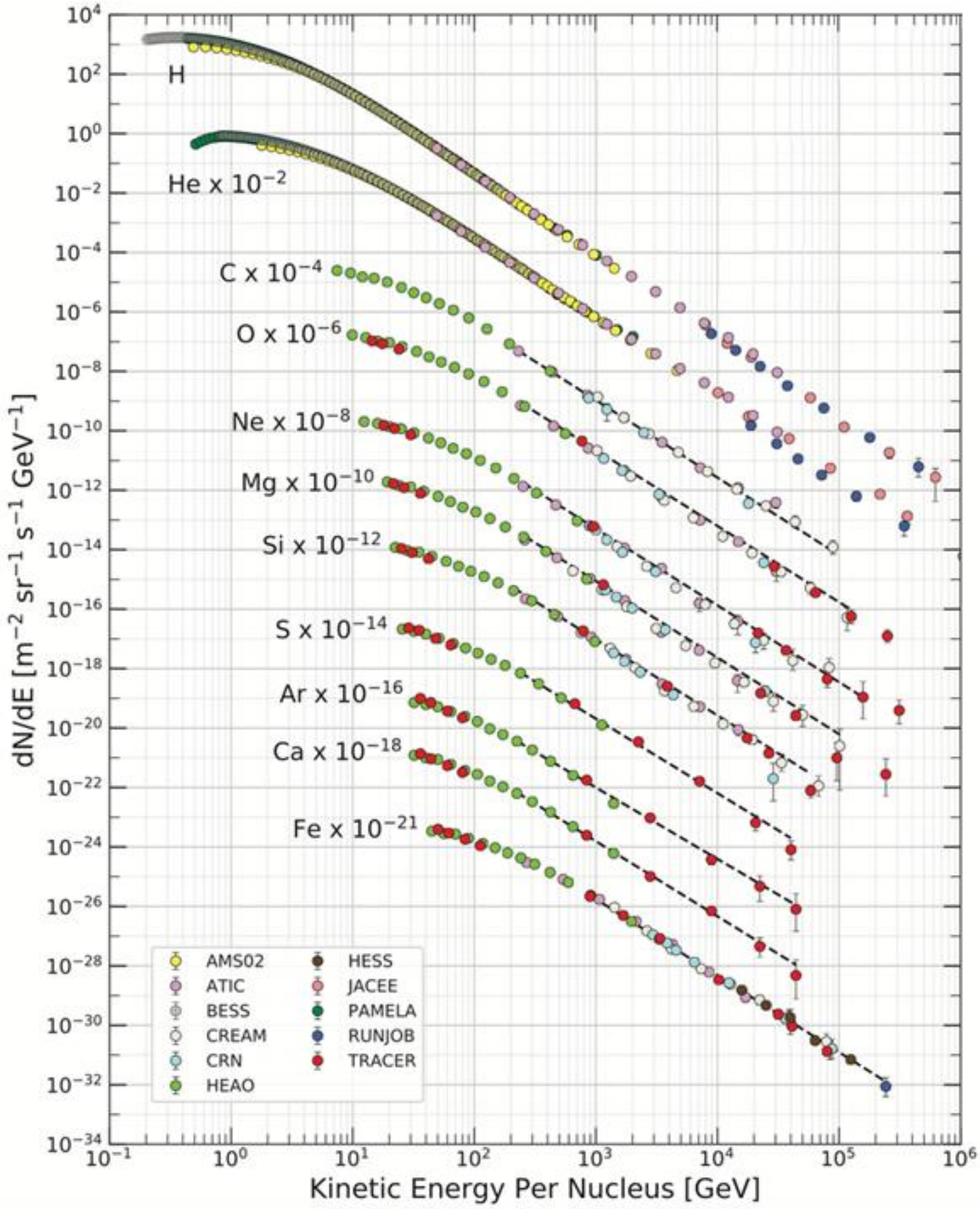

Figure 2.2: GCR primary flux for different GCR nuclei as measured by various experiments [Beatty et al., 2019].

The GCR primary particles are subject to solar modulation, i.e. time dependent change in intensity due to deflection by the solar wind. The sun constantly emits charged particles from its corona in the form of solar wind [Jokipii, 1971], and these particles travel throughout the solar system to form the heliosphere [Parker, 1958; Owens, 2013]. The solar wind is a magnetized plasma that carries with it the interplanetary magnetic field [Beatty, 2017; Solanki, 2000]. The sun has a 22-year solar cycle, which contains two 11-year cycles of roughly sinusoidal variation in solar intensity [ISO, 2004; Solanki, 2000]. Both the solar wind intensity and the number and area of sunspots, dark, visible regions of heightened magnetic activity, vary with the solar cycle, peaking at solar maximum and minimizing at solar minimum [Solanki, 2000]. Because the sunspots vary with solar intensity, the solar cycle can be seen from the sunspot number versus date plot in Figure 2.3.

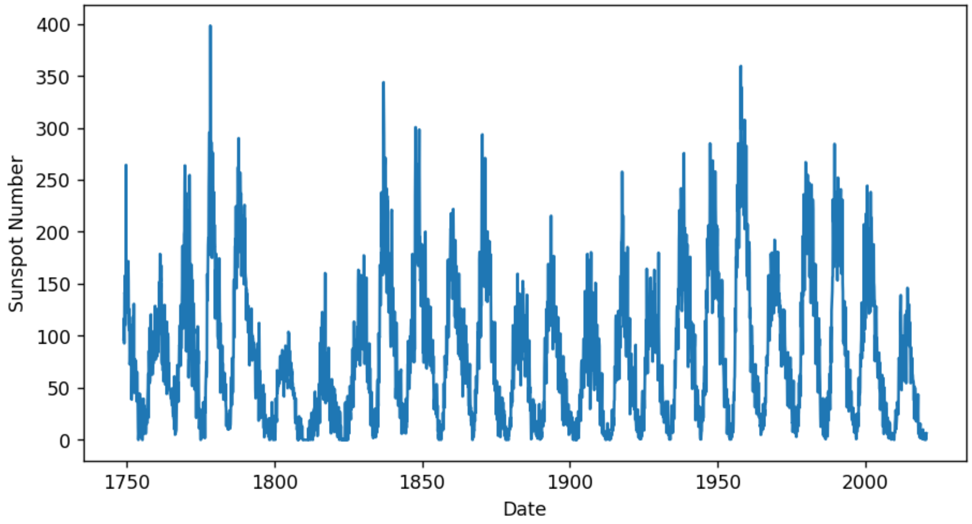

Figure 2.3: Sunspot number versus time [SILSO, 2020].

GCR flux incident on Earth’s atmosphere is inversely proportional to the intensity of solar activity, and low energy GCR are most susceptible to this modulation [Jokipii, 1971]. The GCR proton flux during a period of maximum solar intensity in 2000 compared with the GCR proton flux during a period of minimum solar intensity of 2008 as calculated using the International Organization for Standardization (ISO) GCR model is displayed in Figure 2.4. The effect of solar modulation on GCR protons flux of energy above 10 GeV is negligible. The ISO model is used for all GCR flux calculations in AIREC. The ISO model parameterizes the GCR spectral flux as a function of magnetic rigidity, which quantifies the effect of the heliospheric magnetic field upon the incident GCR particles [ISO, 2004; Norman et al., 2016]. The rigidity has units of voltage and is used to determine whether a GCR primary has sufficient energy to continue through the heliosphere, rather than being deflected away from the Earth. The strength of the heliospheric magnetic field and GCR spectral rigidity vary in intensity with the 22-year solar cycle. These ISO model GCR spectral rigidity functions describe the solar modulation of the GCR primary particles [ISO, 2004; Norman et al., 2016]. The ISO model uses the Wolf number, which is derived from the sunspot number, as a proxy for solar activity [ISO, 2004]. The sunspot number (SSN) has been recorded for centuries and new data is collected by both observatories and amateur astronomers. This sunspot data has been accumulated and is maintained by the Royal Observatory of Belgium, Brussels [SILSO, 2020].

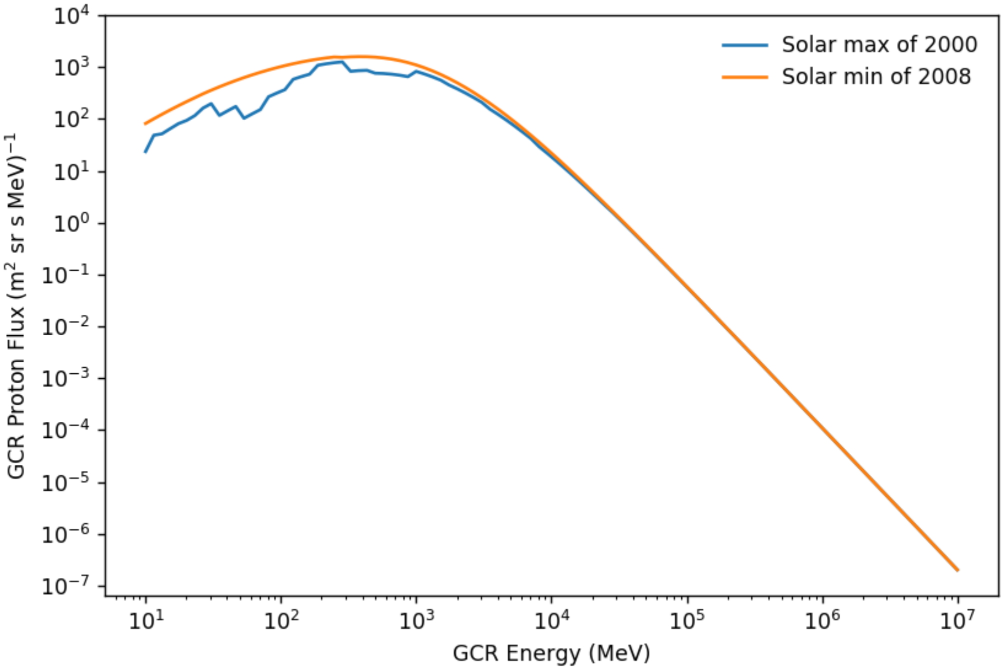

Figure 2.4: GCR proton flux spectra during solar maximum of 2000 and solar minimum of 2008 [ISO, 2004].

Alternative GCR primary models are also available, including the Badhwar-O'Neill model (BO2014) and the German Aerospace Center (DLR) model [Norman et al., 2016]. The BO2014 model incorporates GCR data collected from detectors aboard balloons and satellites [O'Neill, et al., 2015]. The DLR model is a modified version of the ISO model that incorporates GCR data acquired by the Cosmic Ray Isotope Spectrometer (CRIS) aboard the Advanced Composition Explorer (ACE) spacecraft [Matthiä et al., 2013]. A comparison of the ISO, BO2014, and DLR models are displayed in Figure 2.5. Note that above 1 GeV per nucleon the fluxes predicted by the models are nearly identical. GCR primary particles with energies greater than 1000 MeV per nucleon are the majority contributors to secondary particle flux at aviation altitudes, thus the differences among models below 1000 MeV per nucleon are minimal when used to determine the secondary flux at aviation altitudes.

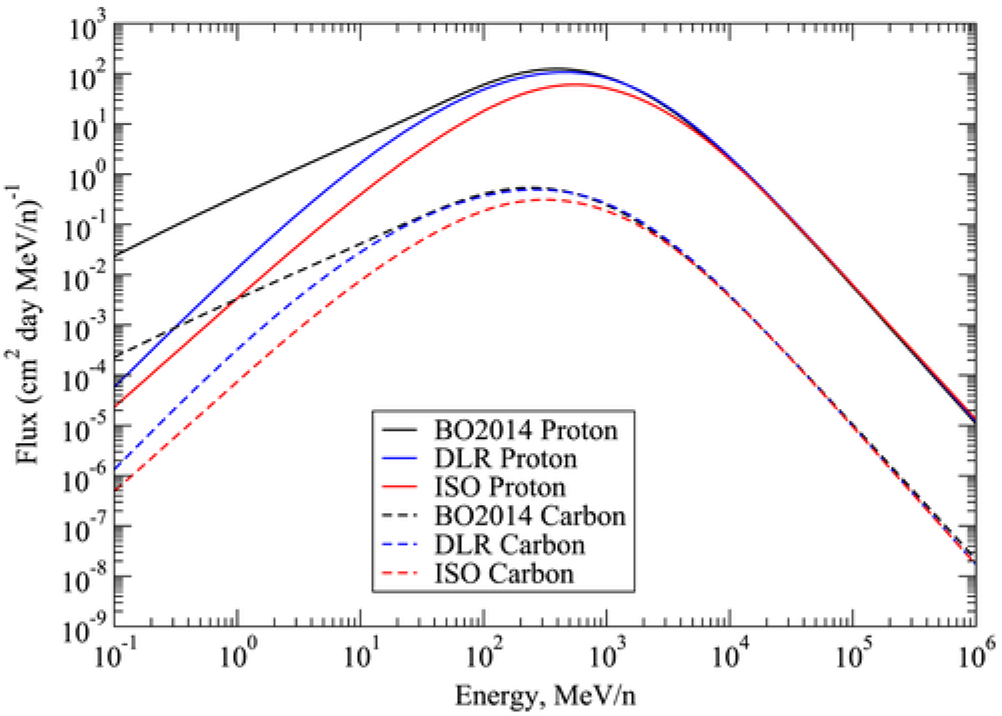

Figure 2.5: A comparison of the Badhwar-O'Neill 2014 (BO2014), International Organization for Standardization (ISO), and German Aerospace Center (DLR) GCR primary models for GCR protons and GCR carbon nuclei [Norman et al., 2016].

2.2. Solar Primary Particles

Although the solar wind modulation of the GCR flux is included in this work, the solar particles that enter the Earth's atmosphere, generate particle cascades, and contribute to the atmospheric radiation environment are not. The solar wind largely consists of the same species charged particles as the GCR primary particles. However, the solar wind particles are on average of significantly lower energy than the GCR primary particles. The flux spectrum of solar wind particles peaks between 1 and 5 keV, and the solar wind contains a negligible number of particles with kinetic energy greater than 35 keV [Cliver, 1990]. Such low energy particles are almost entirely deflected by the geomagnetic field and those that reach the atmosphere of Earth generate very few secondary particles relative to the number of secondary particles generated by GCR primary particles.

The sun can emit higher energy particles that are capable of penetrating the geomagnetic field and generating a large number of secondary particles during solar particle events (SPE). SPE consist of high-energy particles emitted from the sun, and these events can last in the time period from hours to days [Reames, 2020]. SPE can be caused by either solar flares or coronal mass ejection driven shocks [Reames, 2020]. SPE with proton fluence $\Phi(\geq 30 \text{ MeV}) \geq 10^6 \text{ cm}^{-2}$ occur about three to four times per year on average, and SPE with fluence $\Phi(\geq 30 \text{ MeV}) \geq 6.1 \times 10^9 \text{ cm}^{-2}$ occur only about once per solar cycle [Shea and Smart, 1990; Miroshnichenko and Nymmik, 2014]. Theoretically, the occurrence of a large SPE could result in secondary particle fluxes of greater magnitude than the SSAIRE due to the GCR primary particles. However, the frequency of SPE are highly unpredictable, and there is no known method to reliably predict when they occur. Additionally, unlike the GCR flux which is approximately uniform across the Earth (neglecting geomagnetic effects), SPE disproportionately affect different regions of the Earth, i.e. one part of the atmosphere may have a much higher secondary flux due to a SPE than another [Cane, 2003]. Currently, there are no available methods to reliably model the coordinate dependent increase in secondary flux due to a SPE. The unavailability of adequate SPE models led to the exclusion of SPE from AIREC. However, developing a model for the inclusion of SPE in AIREC is an area of interest for future research.

2.3. Geomagnetic Field

The geomagnetic field alters the primary GCR flux by deflecting low energy particles, preventing them from entering the atmosphere. The magnitude of the force on a GCR charged particle moving in the geomagnetic field is described by the equation

$$F = q \left\| \vec{v} \; X \; \vec{B} \right\| = qvBsin\theta, \tag{2.1}$$

where q is the charge of the GCR primary, $\vec{v}$ is its velocity, $\vec{B}$ is the geomagnetic field, and θ is the angle between vectors $\vec{v}$ and $\vec{B}$. The direction of the force is perpendicular to the directions of both the velocity and geomagnetic field vectors.

By consideration of only the component of the geomagnetic field that is perpendicular to the GCR particle velocity, $B_\perp$, a useful quantity called the magnetic rigidity, or simply the rigidity, can be derived. The rigidity is used in two ways. Rigidity quantifies the GCR primary particle's resistance to geomagnetic deflection; higher rigidity corresponds to higher resistance to deflection, and vice versa. Rigidity can also refer to the strength of the geomagnetic field at a location on Earth, and in this use it is called cutoff rigidity. The force produced by $B_\perp$ acting upon an energetic GCR particle traveling in the geomagnetic field results in uniform circular motion. Rearranging equation 2.1,

$$F = m\frac{dv}{dt} = m\frac{v^2}{r} = q\left\|\vec{v}\ X\ \overrightarrow{B_\perp}\right\| = qvB_\perp$$

$$B_\perp = \frac{mv}{qr}$$

$$R = rB_\perp c = \frac{mvc}{q} = \frac{pc}{Ze}, \qquad (2.2)$$

where r is the radius of the charged particle's trajectory, p is the momentum of the charged particle, c is the speed of light, Z is the atomic number, e is the charge of an electron, and R is the rigidity, which has units of volts [Beaujean, 1993; Bütikofer, 2017; Smart and Shea, 1985]. The quantity $rB_\perp c$ can be used to calculate the geomagnetic rigidity at a global coordinate. The radius used in the calculation is typically the radius that would deflect the GCR charged particle sufficiently to prevent it from entering the Earth's atmosphere at that location. The quantity $\frac{pc}{Ze}$ is used to calculate the GCR charged particle cutoff rigidity. The GCR charged particle cutoff rigidity is often instead calculated as a function of its kinetic energy, charge, and rest mass by rearranging two equations for relativistic energy:

$$E^2 = p^2c^2 + m^2c^4 = (T + mc^2)^2$$

$$p^2c^2 + m^2c^4 = T^2 + 2Tmc^2 + m^2c^4$$

$$p^2c^2 = T^2 + 2Tmc^2$$

$$\frac{p^2c^2}{(Ze)^2} = \frac{1}{(Ze)^2}[T(T + 2mc^2)]$$

$$R^2 = \frac{1}{(Ze)^2}[T(T + 2mc^2)]$$

$$R = \tfrac{1}{Ze}\sqrt{T(T + 2mc^2)} \qquad (2.3)$$

In these equations *E* is the total relativistic energy, *T* is the kinetic energy, and the other terms are as before.

Generally, the velocity of the GCR charged particle is not exactly perpendicular to the geomagnetic field, and the geomagnetic field is not uniform. These variations result in a helical GCR particle trajectory, rather than uniform circular motion. Particles with the same rigidity have the same trajectory in a given magnetic field. Therefore, the cutoff rigidity is used to order the trajectories of different species of GCR primary particles traveling through the geomagnetic field.

To arrive at a particular coordinate, a GCR particle must follow an allowed path, otherwise it is deflected away from the Earth. The rigidity necessary for a GCR charged particle to enter the atmosphere at a given coordinate is dependent upon both the zenith and azimuth angles of the arriving GCR charged particle, considerably complicating the cutoff rigidity calculation. Because of this complication a more commonly used quantity is the vertical cutoff rigidity (VCR), which is the minimum rigidity that arriving GCR charged particles with a velocity vector normal (vertical) to the atmosphere must have in order to enter the atmosphere [Smart and Shea, 2003; Smart and Shea, 2005].

In order to calculate the VCR for a location on Earth, the geomagnetic field strength at that location must be known. In a simplified model the geomagnetic field can be approximated as a magnetic dipole, that lies at an 11.7° angle with respect to the Earth's axis of rotation. The geomagnetic poles are opposite the geographic poles, i.e. the geomagnetic north pole is near the geographic south pole and vice versa, as displayed in Figure 2.6 [Lang, 2010].

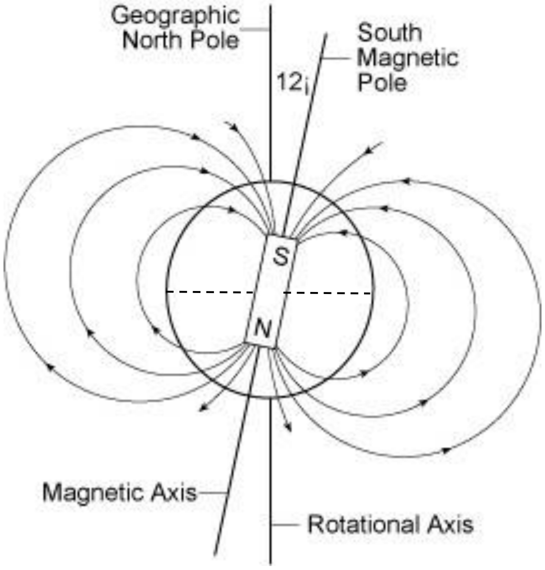

Figure 2.6: The Earth's magnetic field approximated by a magnetic dipole [Lang, 2010].

The geomagnetic field lines are normal to the surface of the Earth near the poles and parallel near the equator, which according to equation 2.1 results in the strongest geomagnetic deflection of the GCR primary particles near the equator (sin(90°) = 1), while the geomagnetic deflection near the poles is negligible (sin(0°) = 0).

In reality, the simple magnetic dipole model of the geomagnetic field is insufficient in describing GCR particle deflection. In the absence of the Earth itself, the geomagnetic dipole model is largely accurate, however the Earth represents a large mass within the magnetic dipole field. As the geographic poles do not align with the magnetic poles, the Earth's mass is asymmetrically distributed throughout the geomagnetic field, further complicating the problem [Lowes, 1994; Copeland, 2014]. The Earth's rotation causes motion in the liquid core, which produces electric current, adding more complexity to the problem [Lowes, 2007]. The geomagnetic field also shifts over time, i.e. there is modulation of the geomagnetic field, making a static model of the field incomplete [Lowes, 2007].

The International Geomagnetic Reference Field (IGRF) is a series of mathematical models that give a more complete description of the geomagnetic field than a magnetic dipole model. The IGRF model includes higher order terms than does the dipole model and is updated regularly to account for new data as the geomagnetic poles shift [Thébault, 2015]. The IGRF model is considered the standard geomagnetic model in the research community [NOAA, 2020; Oehler et al., 2018] and was selected to calculate the VCR for this project.

2.4. Extensive Air Showers

The GCR particles that are unattenuated by the solar wind and have sufficient energy to pass through the geomagnetic field enter the Earth's atmosphere. Upon entering the atmosphere, each primary GCR can initiate a particle cascade. A single GCR primary typically has sufficient energy to produce a large number of secondary particles upon interaction with the nuclei of air molecules present in the atmosphere (predominately N_2, O_2, and Ar), and these secondary particles often have sufficient energy to generate additional secondary particles through further nuclear interactions. After the initial GCR primary particle nuclear interaction, all particles in an

EAS are secondary particles. Collectively, an initial GCR primary and all secondary particles that it generates are referred to as an extensive air shower (EAS) [Grieder, 2010; Rao, 1998]. Because there is a continuous flux of GCR primary particles incident on the Earth's atmosphere, at any given time and geographic location there are multiple EAS developing in the atmosphere. Collectively, these EAS overlap to form the SSAIRE.

An EAS propagates longitudinally, i.e. towards the surface of the Earth, along the direction of the momentum of the initial GCR primary particle. There is a bias in the GCR primary particle incidence angle towards the surface of the Earth, as GCR primary particles that are directed away from the Earth are largely shielded by the Earth itself. As an EAS propagates to greater depths in the atmosphere, it increases in size both in terms of total particle number and in the total volume encompassed by the EAS. More energetic GCR primary particles are capable of producing EAS that have larger numbers of particles and sweep out a larger volume. A highly energetic GCR primary particle can generate an EAS containing billions of secondary particles. The area of the front edge of the EAS grows larger as the shower develops and can sweep out an area of several square kilometers in size. The lateral spread of an EAS is approximately symmetrical about the shower axis along the initial GCR primary particle's direction of initial momentum, so an EAS develops into a conical shape with the vertex where the GCR primary particle first interacted [Benton, 2004]. However, variations in both the geomagnetic field and the density of the atmosphere result in asymmetry of the EAS. The geomagnetic deflection has a greater effect on low energy particles, displacing the lower energy secondary particles more than the higher energy ones, causing asymmetry in an EAS [Greider, 2010]. A GCR primary particle that enters the atmosphere at an angle with respect to the direction normal to the surface of the Earth, produces an EAS that develops laterally at different altitudes. The density of the atmosphere increases exponentially with decreasing altitude, so the portion of the EAS at higher altitude propagates in a less dense medium, which means that there are fewer particles per volume with which to interact.

Generally, this leads to a slower rate of particle generation in the portion of the EAS at higher altitude, leading to asymmetry of the EAS.

The whole of an EAS with the individual components each denoted by a different color is displayed in Figure 2.8. This EAS resulted from a simulation conducted using the CORSIKA Monte Carlo cosmic ray transport code, and the figure shows a track for each created particle. This figure shows a two-dimensional cross section of the lateral spread that occurs as an EAS travels through the atmosphere. In three dimensions the EAS is conical. The size and shape of the EAS depends upon the species, energy, angle of entry, and height of first interaction of the GCR primary particle [Grieder, 2010].

Also shown in the figure is that the flux of particles present in an EAS initially increases, but decreases at greater depths. The total energy of the EAS is mostly the kinetic energy of the initial GCR primary particle, and this energy is conserved. As more secondary particles are produced the total energy becomes divided among more particles, and the average energy per particle decreases. Once the average energy per particle is below the energy necessary to generate additional secondary particles, the flux of the EAS begins to decrease. The altitude at which

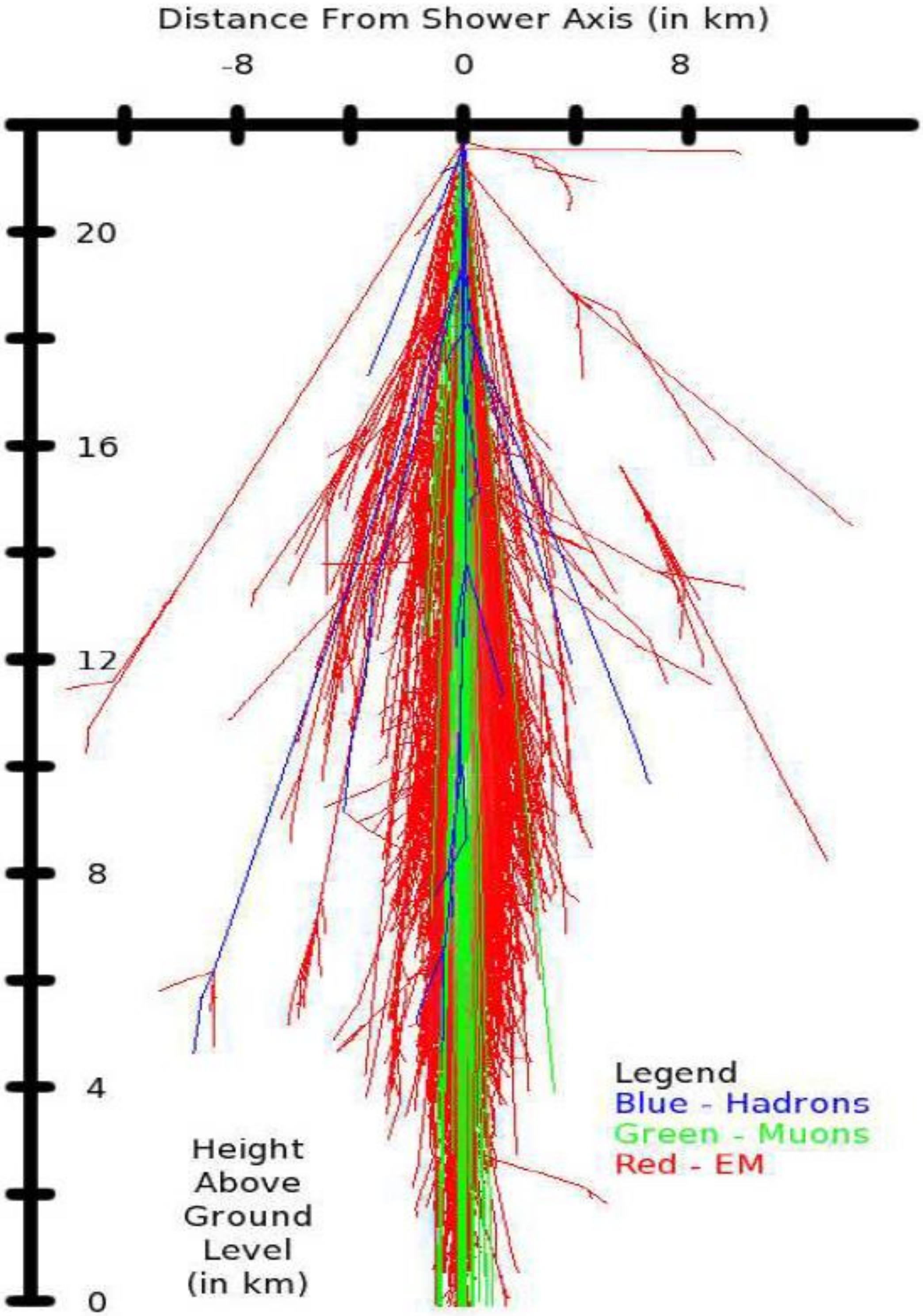

Figure 2.7: The secondary particle tracks resulting from a vertical 1 TeV GCR proton primary [Lindy, 2014].

an EAS has the highest flux of secondary particles depends upon the initial energy of the GCR primary particle, species of the GCR primary particle, altitude of first interaction of the GCR primary particle with atmospheric nuclei, and the angle of entry into the atmosphere of the GCR primary particle. Higher energy GCR primary particles, an angle of entry closer to vertical, and a greater depth of first interaction generally lead to EAS with maximal flux at an altitude nearer to sea level, and vice versa for maximal flux at higher altitudes.

The particles produced as an EAS propagates through the atmosphere depend upon the reaction cross sections of both the GCR primary particle and secondary particles with atmospheric nuclei as they travel through the atmosphere, and these reaction cross sections correspond to the probability of an interaction taking place [Dupree, 2002; Krane, 1988]. The reaction cross section depends upon the energetic particle species, energetic particle energy, and target particle species. Additionally, the rate at which interactions take place depends upon the density of the material. As an example, a GCR primary proton traveling through the atmosphere can undergo a nuclear interaction with a nitrogen nucleus, and there are different possible ways in which the nucleus could fragment. It is also possible for other particles, such as pions or kaons, to be produced from this proton-nitrogen nuclear interaction. Each of these possible interactions has a probability of occurring, which is determined by its reaction cross section. The energy of the proton will dictate whether these interactions are possible and, if so, how probable, i.e. the reaction cross section is dependent upon the energy of the projectile particle traversing the target nucleus. A denser atmosphere means there are more target nuclei per volume, which presents more opportunities for an interaction to take place, increasing the rate at which interactions take place.

Figure 2.7 also displays that the secondary particles that constitute the EAS can be considered to consist of independent components: the hadronic component, the muonic component, and the electromagnetic component. The individual particles comprising each component are shown in more detail in Figure 2.8. The initial GCR primary particles considered in this project are hardrons, and an EAS is generated by a primary hadron that undergoes nuclear interactions to produce additional hadrons, including protons, neutrons, pions, kaons, and heavier nuclear fragments. The pions and kaons decay to produce the muonic component of an EAS. The pions and muons decay to produce the electromagnetic component of an EAS. Ionization of the air by hadrons also contributes to the electromagnetic component of an EAS. Thus, there is some level of interdependence among the three components, as the hadronic component generates the muonic component, and both the hadronic and muonic components generate the electromagnetic component, but after this initiation, interactions among the three components are negligible, so in practice they can be considered independent from one another. Also shown in Figure 2.8 is the Pfotzer maximum, which is the average altitude of maximum secondary particle flux for all EAS for a given latitude and longitude.

Each component is described in more detail in the following sections. Throughout the discussion on each component reference is made to Table 2.1, which lists the mean life time and decay modes for common unstable secondary particles in the atmosphere.

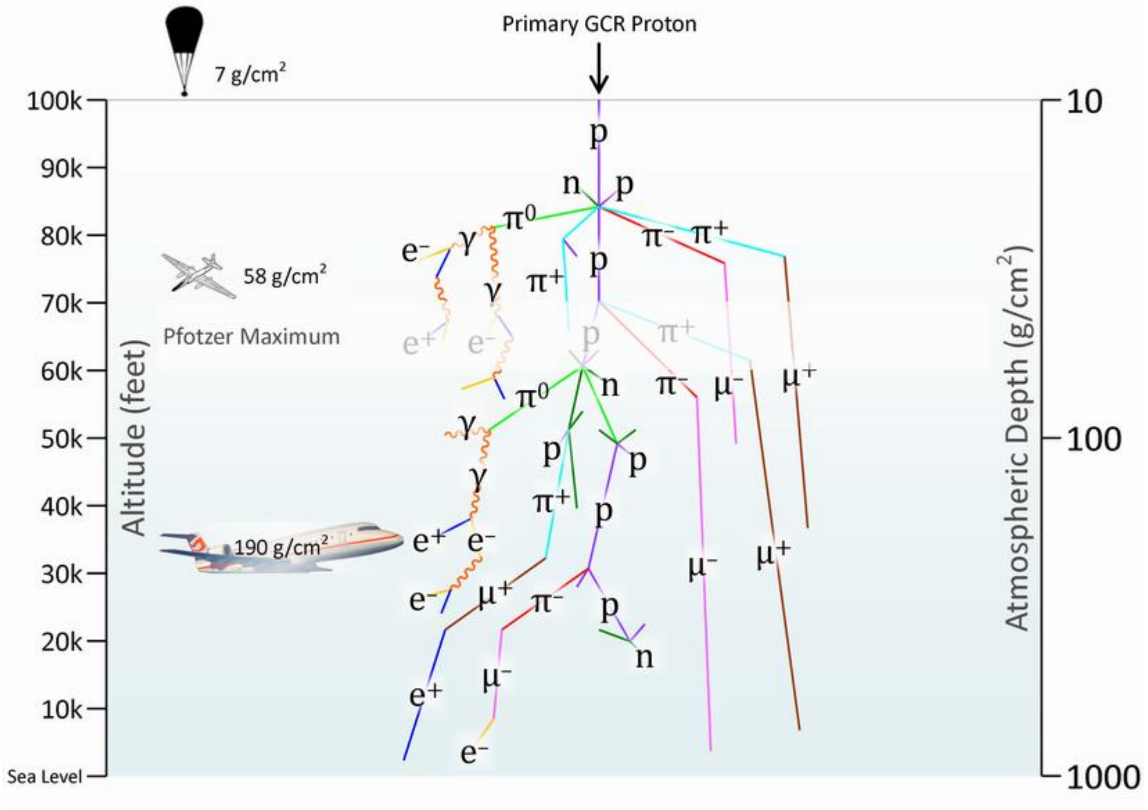

Figure 2.8: The major components of an extensive air shower and the Pfotzer maximum [E.V. Benton RPL, 2019].

Particle	Mean Lifetime (s)	Decay Modes (Branching Ratio)
Neutrons (n)	880.0 ± 0.9	$n \rightarrow p + e^- + \bar{\nu}_e$
Charged Pions ($\pi^\pm$)	(2.6033 ± 0.0005) × 10^{-8}	$\pi^+ \rightarrow \mu^+ + \nu_\mu$
		$\pi^- \rightarrow \mu^- + \bar{\nu}_\mu$
Neutral Pions (π^0)	(8.52 ± 0.18) × 10^{-17}	$\pi^0 \rightarrow 2\gamma$ (~99%)
		$\pi^0 \rightarrow e^+ + e^- + \gamma$ (~1%)
Charged Kaons ($K^\pm$)	(1.2380 ± 0.0021) × 10^{-8}	$K^+ \rightarrow \mu^+ + \nu_\mu$ (~64%)
		$K^+ \rightarrow \pi^+ + \pi^0$ (~20%)
		$K^+ \rightarrow \pi^0 + l^+ + \nu_l$ (~8%)
		$K^+ \rightarrow \pi^+ + \pi^+ + \pi^-$ (~6%)
		$K^+ \rightarrow \pi^+ + \pi^0 + \pi^0$ (~2%)
		$K^- \rightarrow \mu^- + \bar{\nu}_\mu$ (~64%)
		$K^- \rightarrow \pi^- + \pi^0$ (~20%)
		$K^- \rightarrow \pi^0 + l^- + \bar{\nu}_l$ (~8%)
		$K^- \rightarrow \pi^- + \pi^- + \pi^+$ (~6%)
		$K^- \rightarrow \pi^- + \pi^0 + \pi^0$ (~2%)
K-Long (K_L^0)	(5.116 ± 0.021) × 10^{-8}	$K_L^0 \rightarrow \pi^\pm + e^\mp + \nu_e$ (~40.5%)
		$K_L^0 \rightarrow \pi^\pm + \mu^\mp + \nu_e$ (~27%)
		$K_L^0 \rightarrow \pi^0 + \pi^0 + \pi^0$ (~19.5%)
		$K_L^0 \rightarrow \pi^+ + \pi^- + \pi^0$ (~12.5%)
K-Short (K_S^0)	(8.954 ± 0.0004) × 10^{-11}	$K_S^0 \rightarrow \pi^0 + \pi^0$ (~31%)
		$K_S^0 \rightarrow \pi^+ + \pi^-$ (~69%)
Muons ($\mu^\pm$)	(2.196981± 0.000002) × 10^{-6}	$\mu^- \rightarrow e^- + \bar{\nu}_e + \nu_\mu$
		$\mu^+ \rightarrow e^+ + \nu_e + \bar{\nu}_\mu$

Table 2.1: The mean lifetime and decay modes for common unstable particles in the atmosphere. Neutral kaons can be either long lived (K-Long) or short lived (K-Short) [Tanabashi et al., 2018; Beringer et al., 2012; Lindy, 2014].

2.4.1. Hadronic Component

The hadronic component of EAS consists of protons, neutrons, pions, kaons, deuterons, tritons, helions, alpha particles, and heavier nuclear fragments and is generated by nuclear interactions via the strong force of the GCR primary and secondary hadrons with atmospheric nuclei [Grieder, 2001]. Secondary hadrons with sufficient energy can undergo further nuclear interactions with the nuclei present in the air, generating even more hadrons. This process creates a hadron cascade [Grieder, 2001]. Hadrons such as pions and kaons are on average short lived, and their decay contributes to the muonic and electromagnetic components of an EAS [Grieder, 2001]. Because the GCR primary particles have such high kinetic energy and the air density at the top of the atmosphere is low, the majority of hadronic interactions take place at an altitude range of 15 to 35 kilometers after the primary particle has already traveled dozens of kilometers into the atmosphere [Engle et al., 2011].

The hadrons are typically the most energetic portion of an EAS. Due to both the high energy and momentum of the hadronic component, it remains near the core of the EAS, i.e. the hadronic component does not account for the majority of the lateral spread of an EAS [Grieder, 2010]. Hadrons, particularly charged hadrons, also do not typically reach the atmospheric depths that other particles do. Pions and kaons have mean lifetimes on the order of 10^{-8} seconds or shorter, making it much more probable for them to decay in the atmosphere rather than to reach the surface of the Earth before decaying. At the surface of the Earth, only about 1% of the detected particles are hadrons (predominately neutrons) [Greider, 2010; Greider, 2001].

The hadronic component of the EAS generates both the muonic and electromagnetic components. As shown in Table 2.1, charged pions decay via weak interactions into like charged muons, and charged kaons decay via weak interactions predominately into either charged pions or charged muons, although a non-negligible percentage decay into neutral pions [Tanabashi et al., 2018; Griffiths, 1987]. Neutral pions decay electromagnetically into a pair of gamma rays ~99% of the time, although they can also decay into an electron positron pair along with a single gamma ray. Neutral kaons can be either long lived or short lived. A long lived neutral kaon, referred to as a K-long, can decay to produce charged pions, neutral pions, electrons, positrons, and muons, according to the decay modes listed in Table 2.1. A short lived neutral kaon, referred to as a K-short, has a mean lifetime three orders of magnitude shorter than the of a K-long. A K-short can decay into either a pair of neutral pions or a positive-negative pion pair [Tanabashi et al., 2018].

2.4.2. Muonic Component

The muonic component of an EAS is formed from the decays of pions and kaons in the hadronic component. Each charged pion decays into a muon of the same charge and a corresponding muon neutrino. Each charged kaon can decay into either a muon of the same charge or a pion of the same charge. Neutral kaons decay into either a positive, negative pion pair or a neutral pion. Muons create ionization in the air, and they decay via the weak force. Muons originate from hadrons (pions and kaons), and there are minimal amounts of electromagnetic interactions between the muonic and hadronic EAS components. However, muons do not interact via the strong force, meaning they undergo no nuclear interactions, and the effect of the hadronic component on muon trajectories is negligible. Therefore, the muonic component of an EAS can be considered as independent from the hadronic component.

Because muons do not undergo nuclear collisions as hadrons do, there is reduced lateral spread of the muonic component of an EAS. Additionally, muons are about 200 times more massive than electrons, so their trajectories are deflected minimally by electromagnetic interactions. This results in the muonic component of an EAS having the least amount of lateral spread of the three EAS components, as displayed in Figure 2.7.

Muons often have sufficient energy to reach the surface of the Earth before they decay. At the surface of the Earth, about 10% of the detected particles are muons [Greider, 2010; Greider, 2001]. Positive/negative Muons that do not reach the surface of the Earth decay into a positron/electron, an electron neutrino/anti-neutrino, and a muon anti-neutrino/neutrino.

2.4.3. Electromagnetic Component

The electromagnetic component of EAS is produced primarily by neutral pions, but muon decay, ionization of the air by charged hadrons and muons, and Coulombic forces on charged particles that produce Bremsstrahlung radiation contribute as well. Neutral pions decay into a pair of gamma rays, and these gamma rays produce additional photons, electrons, and positrons through different processes. Gamma rays produce additional photons via Compton scattering; electrons via Compton scattering, the photoelectric effect, and pair production; and positrons via pair production. The gamma rays in EAS are typically high energy, and pair production is the dominate interaction in this energy region. The produced photons, electrons, and positrons can produce additional particles. Both the electrons and positrons ionize the atmospheric atoms and emit Bremsstrahlung photons. A positron-electron pair annihilates on collision, forming a pair of gamma rays. Together, these generated particles form an electromagnetic cascade. Each neutral pion initiates a new electromagnetic cascade, and the whole of the electromagnetic component of an EAS can be thought of as the sum of independent electromagnetic cascades.

While neutral pions are the primary contributors to the electromagnetic component of an EAS, other contributors include slower moving muons and muons moving at a lateral trajectory, i.e muons that do not reach the surface of the Earth. These muons decay into an electron or a positron, matching the charge of the muon. After the initial generation from hadronic and muonic components of an EAS, the electromagnetic portion of the EAS interacts minimally with the other two components and is considered to be independent of them.

Electrons and positrons have much lower mass than the constituents of the hadronic and muonic components of an EAS, and they are therefore much more susceptible to deflection. Massless photons can change directions as a result of Rayleigh and Compton scattering. As a result, the electromagnetic portion of the EAS laterally spreads out from the core of the EAS much more than do either the hadronic or muonic components and is responsible for the majority of the conical volume encompassed by an EAS. The electromagnetic component represents not only the largest EAS component by volume but also by total number of particles. 90% or more of particles detected at the surface of the Earth are electrons and positrons, and these percentages exclude photons [Greider, 2010; Greider, 2001].

2.4.4. The Steady State Atmospheric Radiation Environment

GCR primary particles are constantly entering the top of the Earth's atmosphere at a range of angles. Each of these GCR primary particles has the potential to produce an EAS, so there are simultaneously many EAS throughout the atmosphere at any moment. These EAS overlap with one another to produce the SSAIRE. For example, a GCR primary particle entering vertically at the top of the atmosphere will most often produce an EAS that propagates directly beneath the GCR primary particle's point of entry, as shown in Figure 2.7 of the CORSIKA simulation. A GCR primary particle arriving at a different location at the top of the atmosphere but at an angle with respect to a vector normal to the surface of the top of the Earth's atmosphere could produce an EAS that intersects with that of the vertically entering GCR primary particle. The EAS resulting from each of these GCR primary particles as well as many others overlap to produce the total SSAIRE for a given location.

As previously stated, each EAS has an altitude at which the maximum number of ionizations occur. The average altitude of maximum ionization, weighted by the size of each EAS, yields the altitude of maximum ionization for the SSAIRE as a whole. This location is known as the Pfotzer maximum. The Pfotzer maximum is at an altitude of approximately 18 kilometers [Hands et al., 2016]. Figure 2.9 displays both a measurement and a model of the dose rate as well as the altitude as functions of time [Benton, 2004]. The Liulin-4 mobile dosimetry unit, consisting of a Mobile

Dosimetry Unit (MDU) was used to detect the dose rate aboard a flight, while the Atmospheric Ionizing Radiation (AIR) model computer code was used to model the same flight [Benton, 2004]. The dose rate increases with the altitude, as the aircraft reached altitudes corresponding to the Pfotzer maximum.

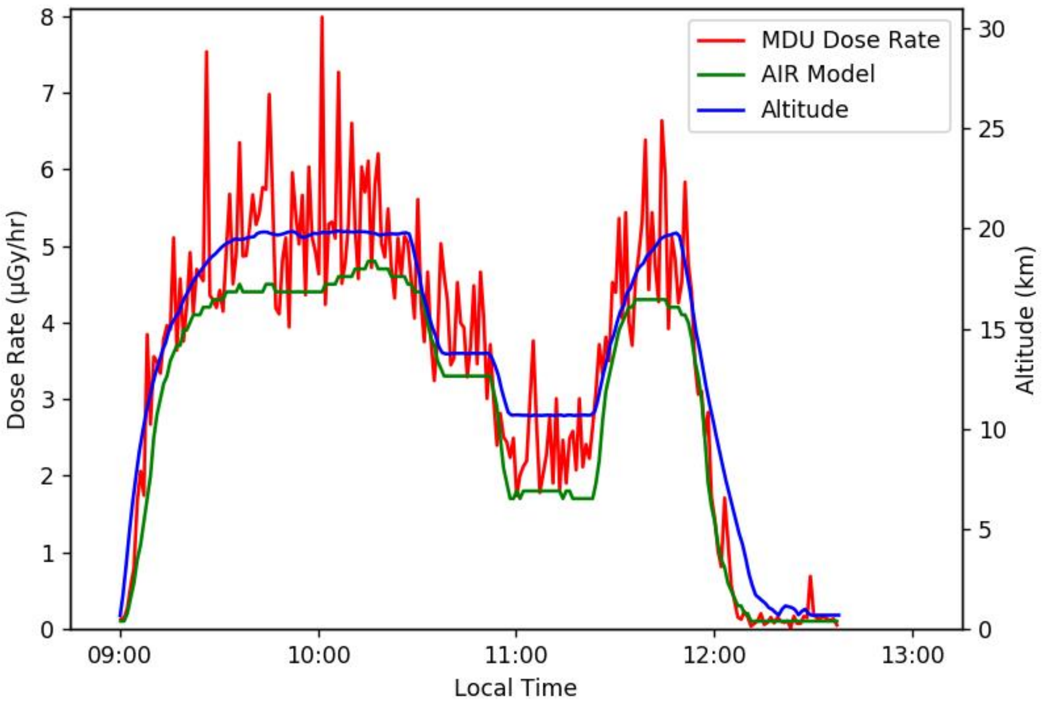

Figure 2.9: Dose rates as measured by the Liulin-4J MDU and recorded by the AIR model alongside the altitude, all plotted as a function of time [Benton, 2004].

The SSAIRE is the constant particle flux present in the atmosphere over the course of minutes to hours. Over shorter time intervals, an individual EAS causes significant variation in the second to second particle flux. For example, a rare, high energy GCR primary could enter the atmosphere, resulting in a high flux EAS in a region, but this high flux would not be representative of the average flux of the region. There are predictable variations to the SSAIRE over longer time periods. Over the course of a day, there is diurnal variation in atmospheric secondary particle flux, i.e. a noticeable change in the secondary particle flux during day time versus during night time. Over the course of months and years there is variation in solar wind intensity, resulting in solar modulation of GCR primary intensity. Within the time frame of minutes to hours, the SSAIRE is created by GCR primary particles with energies ranging from about 10 MeV to 1 TeV. GCR primary particles with energy below 10 MeV have high flux, but they contribute to the SSAIRE only at the top of the atmosphere, having insufficient energy to generate EAS that reach aviation altitudes (~12 km). GCR primary particles with energy of 1 TeV are incident upon the Earth at a rate of 1 particle per meter squared every three hours, and higher energy GCR primary particles are rarer. Figure 2.10 displays the neutrons per area per GCR proton versus GCR proton energy for several different altitudes.

The bulk of cosmic ray research has focused on GCR primary particles with energy above 1 TeV and these primary particles are the source of a wealth of interesting physics. However, such energetic primary particles are too rare to consistently contribute to the SSAIRE and are therefore not considered this work.

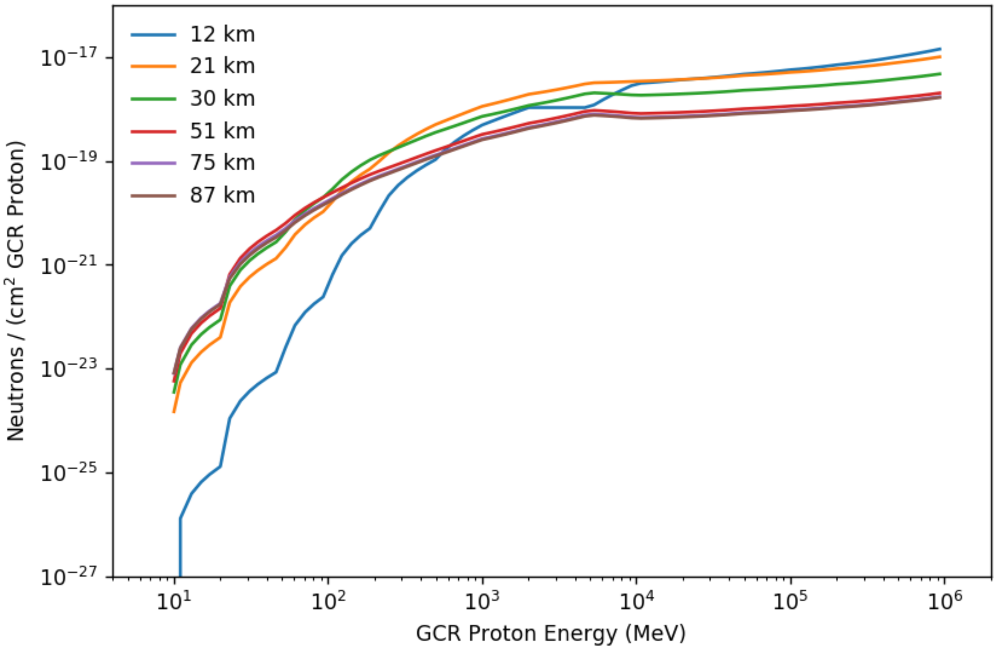

Figure 2.10: Neutrons per area per GCR proton versus GCR proton energy at several altitudes.

The radiation transport code Monte Carlo N Particle (MCNP) was used to model EAS. MCNP is a Monte Carlo based radiation transport code, and the use of such codes is standard for modeling the interaction of radiation in the atmosphere. Features such as the species, energy, and angle of entry of the GCR primary were accounted for in the MCNP model. Likewise, given the composition and density of the atmosphere, MCNP contains databases of energy dependent cross sections for each particle species, giving the probabilities for different interactions. Given the importance of the Monte Carlo method of radiation transport and MCNP to this work, a more complete discussion of each is given in chapter 4.

2.5. Conclusions

The models of the physical phenomena discussed can be combined in order to determine the secondary particle flux in the atmosphere. The ISO GCR primary model is used to determine the GCR flux at the top of Earth's atmosphere absent the geomagnetic field. The IGRF geomagnetic field model gives the particle rigidity for different locations on the Earth, which dictates the minimum kinetic energy the GCR primary particles from the ISO model need to traverse the geomagnetic field and interact in the atmosphere. The MCNP air shower models are used to describe how the GCR primary particles that reach the top of the atmosphere and their secondary particles interact. A full description of how the models of the physical phenomena were combined to determine the secondary particle flux in the atmosphere is the subject of chapters 3 and 4.

CHAPTER III

SECONDARY FLUX ENERGY SPECTRUM IN THE ATMOSPHERE

3.1. Capabilities of the Code

The goal of this project was to develop a software tool to generate flux energy spectra from ionizing secondary radiation produced in the atmosphere as a result of cosmic ray air showers, given an altitude, latitude, longitude, and date/time. The finished code is called AIREC – Atmospheric Ionizing Radiation Environment Code. In practice, AIREC takes a user input file containing a set of coordinates for one date and one secondary particle type and returns a secondary flux energy spectrum for each of the user coordinates. The flux energy spectrum has units of

$$\frac{secondary\ particles}{cm^2\ s}$$

The spectrum is formed by dividing the secondary particles into energy bins. An example of such a secondary flux energy spectrum is displayed in Figure 3.1. This figure displays the secondary flux energy spectrum at 10 kilometers above Stillwater, OK in November of 2010.

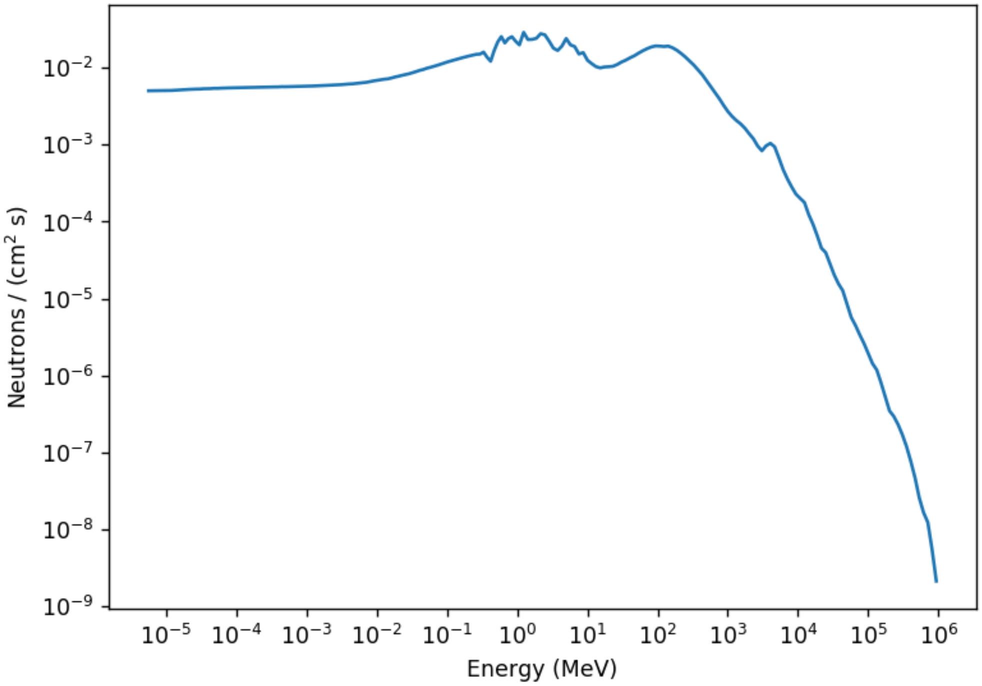

Figure 3.1: The secondary neutron flux spectrum at 10 kilometers above Stillwater Oklahoma during November 2010.

Two broad areas of study can be addressed using the output secondary particle flux spectra generated by AIREC: 1) details regarding the particular aspects of the radiation environment present in Earth's atmosphere, and 2) particle spectra for simulations of the effect of this radiation on avions, materials, radiological dose, etc. In the study of particular particle types and/or physical dependences within the radiation environment, secondary flux spectra such as that shown in Figure 3.1 can be generated from AIREC given any latitude, longitude, altitude, date, and particle of interest within the following limits:

1. The altitude must be within the range 0 kilometers to 100 kilometers.

2. The latitude must be from -90 degrees north to 90 degrees north.

3. The longitude must be from 0 degrees east to 360 degrees east.

4. The date must be from January 1, 1752 to the latest date for which sunspot data is available, generally one month prior to the present.

5. The particle of interest must be one of the following: neutrons, photons, electrons, positrons, positive or negative muons, protons, positive or negative pions, deuterons, tritons, helions, alphas, or any heavy ion from lithium to iron.

From the simulation of these particle spectra for specific sets of conditions, broad trends in the atmospheric radiation environment can be ascertained. Such trends include the change in flux as functions of the latitude, longitude, altitude, and date on a variety of temporal and spatial scales.

AIREC generated spectra can be used as input to other computer models, to investigate the effects of the radiation present in the atmosphere on various materials and electronics, or for use in models that simulate various types of atmosphere phenomena. One example is the determination of absorbed dose rates and effective dose rates from a radiation protection point of view produced by particular particle species under varying conditions. AIREC can be used to get the spectra for each particle species at specified coordinates and a date, and the spectrum for each particle species can be converted to dose or effective dose rates using the appropriate fluence to dose conversion coefficients. Fluence to dose conversion coefficients have been determined using Monte Carlo radiation transport simulations of particles incident on a humanoid phantom. In these simulations both the particle fluence across the phantom and the absorbed dose to the phantom are recorded, allowing for the calculation of fluence to dose conversion coefficients [Ferrari et al., 1997]. Similarly, the effectiveness of various shielding materials when exposed to atmospheric radiation can be tested by using the AIREC output as an input in a Monte Carlo simulation of the absorbed dose behind such shielding. Alternatively, the response of a particular radiation detector to various components of the atmospheric radiation environment can be simulated using an appropriate AIREC particle spectrum as input to a Monte Carlo simulation of the detector's geometry. A detailed example of using an AIREC output spectrum to further explore the atmospheric dose rate, the effectiveness of shielding materials, and a comparison with a physical detector is given in Chapter 6.

3.2. Necessary Components of the Code

The development of AIREC required models of the following physical phenomena: the GCR flux at the top of the Earth's atmosphere, the transport of GCR particles and the secondary particles that they produce as they travel through the atmosphere, and the geomagnetic field. Data for these models in large part already exist from the development of the CARI-7 code. CARI-7 was developed by the Federal Aviation Administration (FAA) as a means of calculating the effective dose to pilots, flight attendants and aircraft passengers due to atmospheric radiation that results from GCR. The transport of GCR particles and their secondary particles through the atmosphere is a particularly computationally intensive problem, requiring millions of CPU core hours of computation time to simulate. This particle transport data resulted from MCNP (Monte Carlo N Particle) code simulations run in the course of developing the CARI-7 software [Copeland, 2014; Copeland, 2017]. MCNP was selected for this task in large part for its accurate treatment of neutrons, as neutrons at aviation altitudes are responsible for about half of the total dose equivalent [Nakamura, 2008]. MCNP's handling of neutrons has been widely tested against experimental results and has returned satisfactory results within statistical uncertainty across a variety of problem types [Whalen et al., 1991; Little, 2012].

The MCNP output data resulting from the development of CARI-7 was in the form of energy binned secondary particle flux values at discrete altitudes due to GCR particles of discrete energies being propagated into the atmosphere. The secondary flux units were in terms of

$$\Phi_{MCNP} = \frac{secondaries}{cm^2\ GCR}.$$

Here, Φ_{MCNP} denotes the MCNP flux with the above units. The secondary flux data was recorded in terms of secondary particles per centimeter squared at a specific altitude due to a given species of GCR of a discrete energy. This secondary flux was divided into energy bins to form a secondary flux spectrum. In all, 26 species of particles from hydrogen (Z=1) to iron (Z=26) were transported as primary GCR, and for each of these GCR particles 19 different starting energies at the top of the atmosphere were simulated, i.e. 26×19=494 unique MCNP simulations were conducted. For each simulation the secondary particle flux for each of several species of particles was recorded at 19 different altitudes logarithmically spaced from 0 to 100 kilometers. Figure 3.1 displays the discrete energies used for the GCR particles in the MCNP simulations as red lines superimposed on a graph of the continuous GCR spectrum.

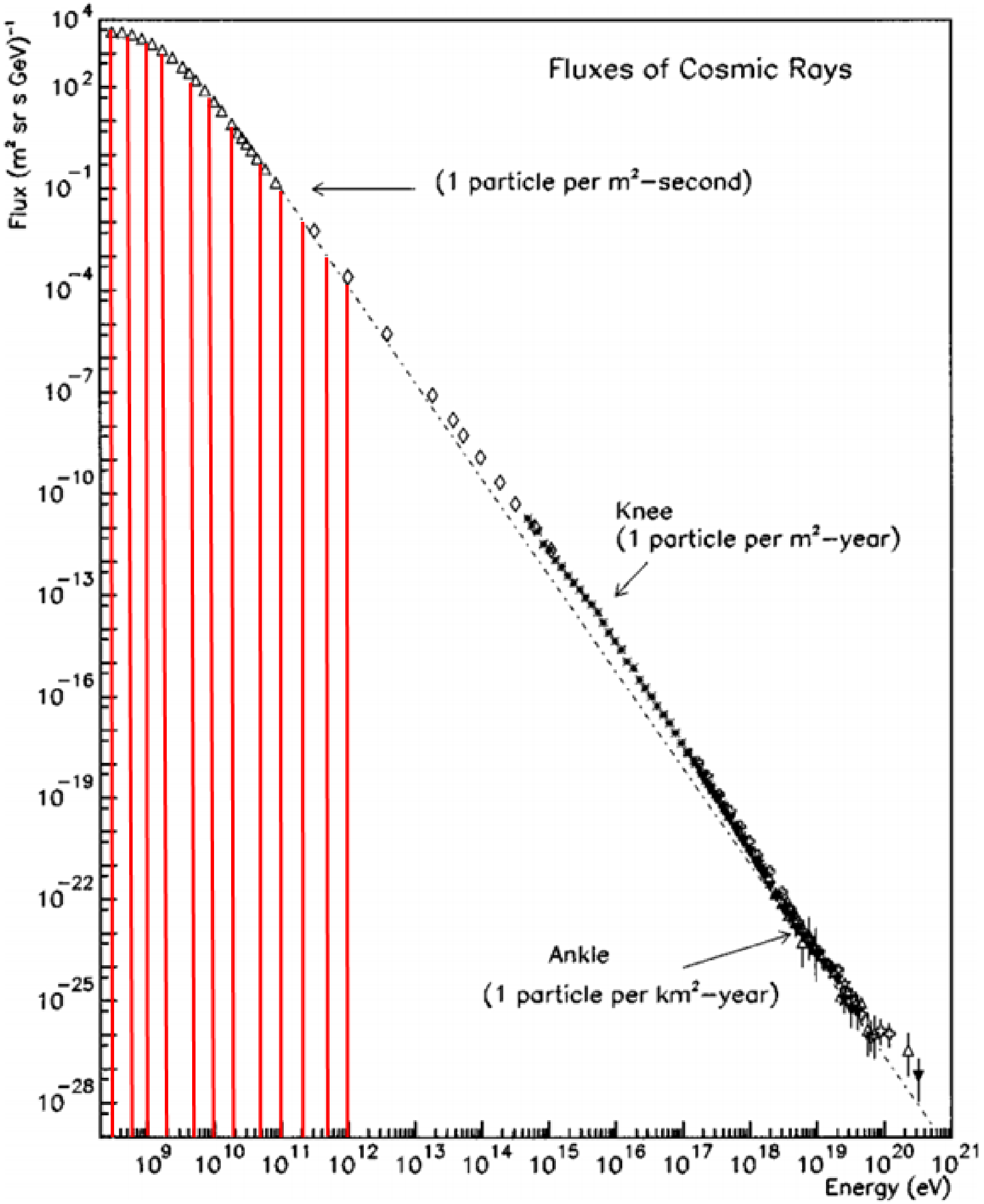

Figure 3.2: The GCR spectrum with the GCR energies run in MCNP marked with red lines [Cronin, 1999].

Note that while the GCR spectrum is continuous, discrete energies were used for MCNP simulations. Secondary fluxes due to different primary GCR energies were acquired by interpolating between the discrete GCR energies used in simulations. The method of interpolation is detailed in Chapter 4. Note also that the MCNP simulations did not take into account the magnitude of the GCR flux at different energies. The secondary fluxes in the output were given on a per starting particle basis, i.e. the number of secondary particles per centimeter squared for each GCR particle of a given energy incident on the top of the atmosphere. The MCNP output files describe the average secondary flux average simulating millions of each species of GCR of a discrete energy.

The transition from Φ_{MCNP} (units of $\frac{secondaries}{cm^2\ GCR}$) to an approximation of the secondary flux actually present in the atmosphere (denoted Φ with units of $\frac{secondaries}{cm^2\ s}$) required an incident GCR flux in terms of GCR per second. Multiplying the MCNP secondary flux output by the GCR flux

$$\Phi_{MCNP} \times \Phi_{GCR} = \Phi = \left(\frac{secondaries}{cm^2\ GCR}\right)\left(\frac{GCR}{s}\right) = \frac{secondaries}{cm^2\ s}.$$

Another way of representing the secondary flux commonly seen in the literature is via the differential flux. The differential flux is obtained by dividing the flux of each energy bin by the energy bin width. Thus,

$$Differential\ Flux = \frac{d\Phi}{dE} = \frac{(MCNP\ output)\times(GCR\ Flux)}{Energy\ Bin\ Width} = \frac{secondaries}{cm^2\ s\ MeV}.$$

In the literature the flux is also represented by the lethargy $\left(E \cdot \frac{d\Phi}{dE}\right)$. Given a plot of differential flux versus energy, the lethargy is calculated by multiplying each differential flux by its corresponding energy, i.e. the lethargy a new set of y values calculated by multiplying each original y value by its corresponding x value.

$$Lethargy = E \cdot \frac{d\Phi}{dE} = \frac{(MCNP\ output)\times(GCR\ Flux)}{Energy\ Bin\ Width} \times (Average\ Bin\ Energy) = \frac{secondaries}{cm^2\ s}.$$

Note that the units of lethargy $\left(E \cdot \frac{d\Phi}{dE}\right)$ are the same as those of the secondary flux Φ, but these are not identical quantities. The secondary flux is a more fundamental quantity that describes the rate at which secondary particles cross a detector divided by the area of the detector. The lethargy is generally used as a visualization tool. It magnifies differences in features of a spectrum that would otherwise be missed in a secondary flux or differential flux representation.

While the product of the MCNP flux and the GCR flux does return the atmospheric secondary particle flux with the correct units, there is a further complication. The GCR flux is altered by the geomagnetic field. The geomagnetic field deflects incident GCR according to the Lorentz force law (equation 2.3). Because the geomagnetic field varies at different geographic coordinates, the intensity of the GCR flux likewise varies, which in turn alters the atmospheric secondary particle flux.

In all, the accurate calculation of the secondary particle flux in Earth's atmosphere required a model of the GCR spectrum at the top of Earth's atmosphere, a model of the interactions of the GCR with the atmosphere, and a model of the geomagnetic field, all of which will be discussed in chapter 4. The necessity and interplay of these three models are demonstrated in the flowchart of Figure 3.3.

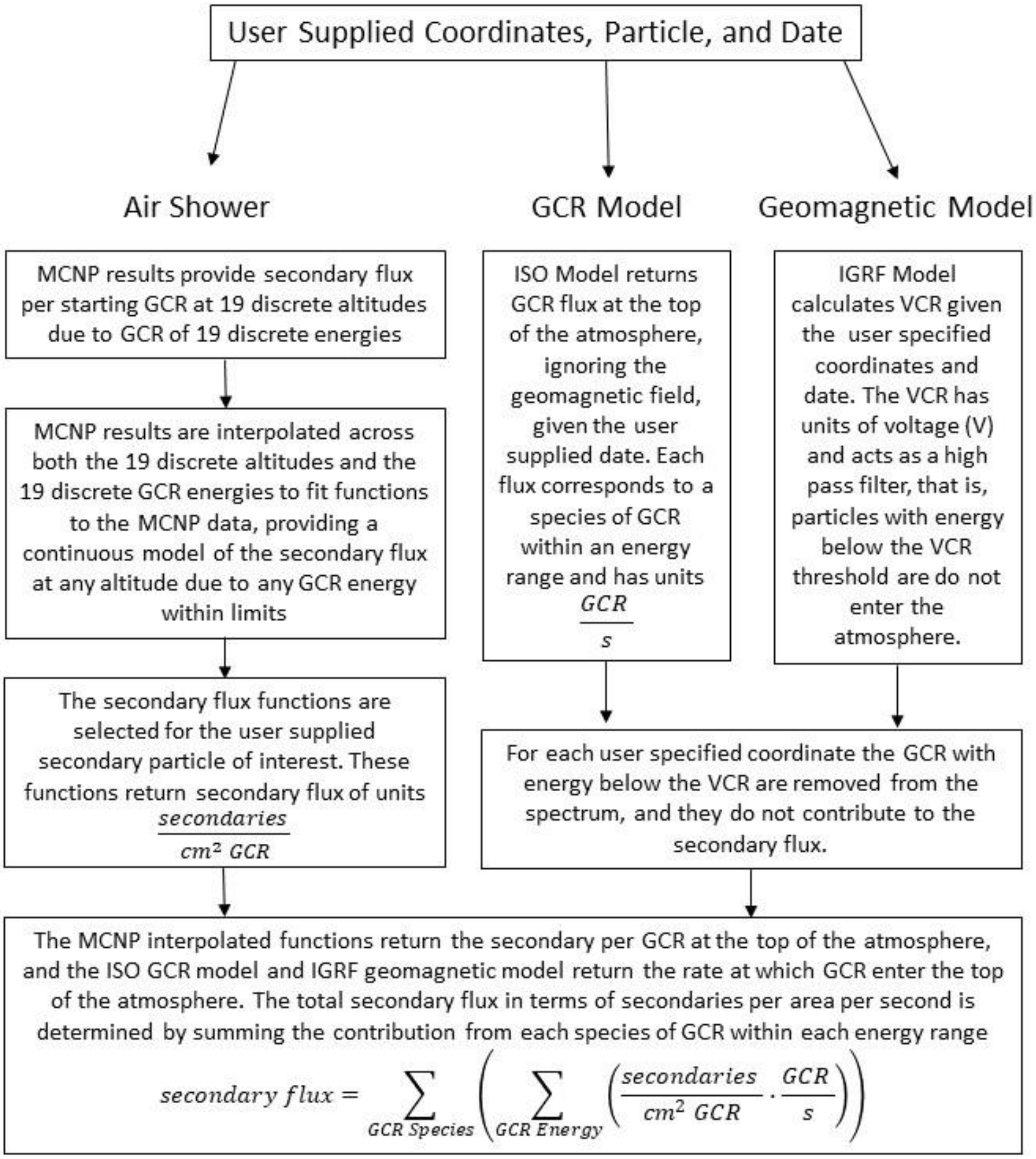

Figure 3.3: A flowchart describing the interaction of the models used in developing AIREC

3.3. Limitations of AIREC

AIREC estimates the average features of the ionizing radiation environment in the atmosphere for a given location, altitude, and date. AIREC is not able to simulate a number of either rare or subtle events. Here are described phenomena that were not included in AIREC. Each is a potential area for further improvement of AIREC.

As shown in Figure 3.2, the MCNP data used in developing AIREC resulted from MCNP simulations that did not considered GCR with energies greater than 1 TeV. While interesting events can result from these higher energy GCR, these events are sufficiently rare that they do not significantly contribute to the average secondary flux and were not considered in this thesis work. MCNP is not well suited for transporting particles with energies above 1 TeV, thus further work in this area would require a different means of investigation [Mashnik, 2017]. The documentation for the Monte Carlo based radiation transport code FLUKA records transport limits of up to 20 TeV for all particle types, making it a possible candidate for simulations of GCR primary particles above 1 TeV [Böhlen et al., 2014; Ferrari et al., 2005].

Secondary flux contributions from GCR with atomic number greater than 26 were not accounted for in AIREC. These high Z GCR are sufficiently rare that they have negligible impact on the average atmospheric radiation environment. GCR iron primary flux is many orders of magnitude lesser than that of GCR hydrogen primaries, and generally, GCR flux is inversely proportional to the atomic number, making GCR primaries of higher atomic number than iron exceedingly rare [Beatty et al., 2019].

As discussed in section 2.2, atmospheric secondary flux resulting from solar particle events (SPE) are likewise not incorporated into AIREC. The SPE contribution to the atmospheric secondary flux is rare and localized [Cane, 2003], meaning that the average radiation environment in minimally affected. While it is true that large SPE can result in secondary particle fluxes that are of greater magnitude than the SSAIRE due to GCR primary particles, there do not exist models of the SPE that could be incorporated into AIREC. If the flux at the top of Earth's atmosphere of each particle species in a SPE were known, then the flux of these particles could be added to the

GCR primary particle flux, and the resulting secondary particle flux due to both GCR and SPE could be determined.

There is a diurnal variation in secondary flux, i.e. a difference in the atmospheric secondary flux during the daytime versus nighttime. This is a subtle but detectable variation with the nighttime flux exceeding the daytime flux by approximately 0.2% to 0.8% [Brunberg and Dattner, 1953; Parker, 1964]. There is not a consensus view on the cause of the diurnal variation of the secondary flux, but one theory is that it is due to the interaction of the solar wind with the geomagnetic field, modulating the geomagnetic field strength over the course of a day [Stassinopoulos, 1987]. Currently, no model of the diurnal variation exists, and it is not part of AIREC calculations. Future work could include using experimental data to develop a model of the diurnal variation of the secondary particle flux.

Another limitation of AIREC is that the highest altitude for which a secondary flux spectrum can be calculated is 100 kilometers. The 1976 US Standard Atmosphere model does include atmospheric data for up to 1,000 kilometers, however the density of the atmosphere at 100 kilometers is on the order of 10^{-10} g/cm^3, and this density decreases to a magnitude on the order of 10^{-18} g/cm^3 at 400 km [NOAA, 1976]. At such low atmospheric densities the incident GCR are largely unaffected. At most locations on the globe, the geomagnetic field has already attenuated the low energy GCR that potentially would be attenuated by the atmosphere from 400 km to 100 km. Thus, AIREC assumes the flux in this region of the atmosphere to be constant.

CHAPTER IV

MODELING AND ANALYZING COSMIC RAY INDUCED AIR SHOWERS IN EARTH'S ATMOSPHERE

4.1. Approach to the Problem of Modeling Radiation Transport through the Atmosphere

Modeling the transport of GCR through the atmosphere was accomplished using the results from the MCNP (Monte Carlo N Particle) radiation transport code generated in the course of developing the previously described CARI-7 computer model developed by Copeland [Copeland, 2014; Copeland, 2017]. A description of MCNP, the Copeland MCNP input files, and the contents and analysis of the MCNP output files are discussed in the following sections.

4.2. Description of MCNP

MCNP is a software code developed by Los Alamos National Laboratory that models the transport of radiation through matter using the Monte Carlo method. The Monte Carlo method of radiation transport is a means of simulating the passage of energetic particles through matter. A particle moving through matter can interact with the matter in a number of ways depending on the species of particle, the energy of the particle, and the composition of the matter through which the particle travels. MCNP contains databases of cross sections for a multitude of different projectile particles, particle energies, and target materials that were determined from theory and experiment. These cross sections correspond to the probability of an interaction, i.e. each possible interaction for a particle of a given energy traveling through a medium has a cross section describing the probability of the interaction occurring [Dupree, 2002; Krane, 1988]. For a given particle, particle energy, and medium through which the particle travels, MCNP breaks the particle's trajectory into small distances, or steps. For each step MCNP looks up the relevant cross sections and calculates the probability for each of the possible interactions the particle could undergo in that step. Each of these interaction probabilities is mapped to a sub interval of numbers between 0 and 1 where the sub interval size is equal to the size of the interaction probability [X-5 Monte Carlo Team, 2003; Knuth, 1981]. Note that there must also be an interval associated with no interaction taking place, and all sub intervals must sum to 1. A random number on the interval [0, 1] is then generated. If the random number falls within an interval corresponding to a given interaction, the transported particle is treated as though that interaction occurred. The particle's energy and velocity vector are updated, and the particle moves to the next step. If any additional particles were created as a result of the interaction they are banked, i.e. stored in memory and transported after the current particle's history is completed. If the interaction annihilates the particle or if the particle exits the user defined bounds of the problem, MCNP continues to the next particle to be simulated. This process is used to simulate a number of individual particles moving through matter and record some aspect of their average behavior. The resulting average particle behavior is also called the tally [X-5 Monte Carlo Team, 2003].

As an example, consider the radiation transport simulation of neutrons moving through a slab of material as shown in Figure 4.1. Suppose the average particle behavior of interest here is the number of secondary photons crossing Surface 2 for every neutron of a given energy crossing

Surface 1. Surface 2 is a tally surface, and every photon that crosses it will be recorded. At the conclusion of the simulation the total number of photons that crossed Surface 2 is divided by the total number of starting neutrons, giving the average number of photons crossing Surface 2 for each starting neutron. The simulation of one starting particle and all of the secondary particles that it produces is known as a particle history. Figure 4.1 shows a hypothetical history for one starting neutron. In the initial steps the neutron undergoes no interactions. At event 1 the neutron inelastically scatters, producing a secondary photon. The photon is banked, meaning MCNP stores it in memory, but its movement through the material is not simulated until after simulating the neutron's movement. The scattered neutron continues until event 2 at which point the neutron is captured, and is thus terminated by MCNP. The motion of the banked photon from event 1 through the slab is then simulated. This photon moves through the slab without interaction until event 3, Compton scattering of the photon. The electron produced by the Compton scattering is banked, and the photon continues without interaction until event 4, the photon's exit of the problem bounds. Because this photon crossed Surface 2, it is tallied. The electron banked from the earlier Compton scattering is then transported and is subject to Coulomb forces in the material through which it is traveling, resulting in the production of two Bremsstrahlung photons, events 5 and 6. At event 7 the electron exits the problem bounds. The two banked Bremsstrahlung photons are then transported one after the other, each exiting the problem bounds in events 8 and 9 and each photon is tallied when crossing Surface 2 [X-5 Monte Carlo Team, 2003].

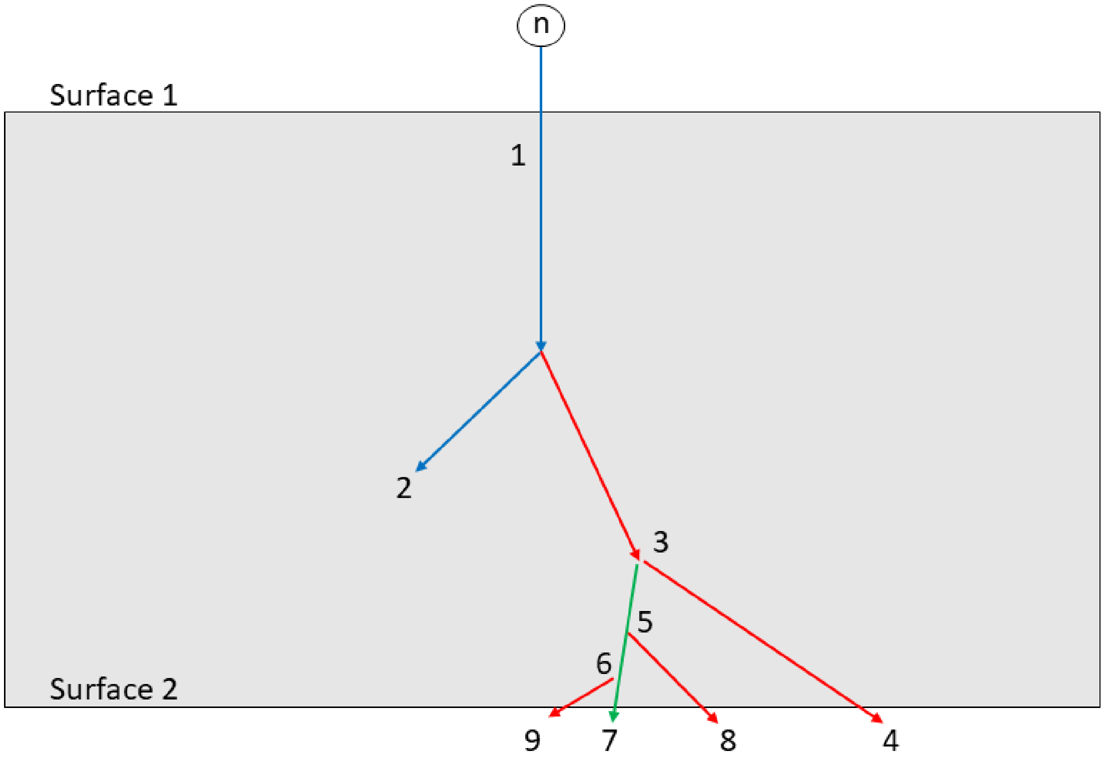

Figure 4.1. *One history of a neutron moving through matter. The event log is as follows:*

1. *The incident neutron inelastically scatters, producing a photon, which is banked.*
2. *The neutron is captured, resulting in its termination.*
3. *The banked photon undergoes Compton scattering, producing an electron, which is banked.*
4. *The photon exits the problem bounds and is terminated.*
5. *The electron banked from the earlier Compton scattering loses energy due to Coulomb interactions, producing a Bremsstrahlung photon that is banked.*
6. *The electron produces another Bremsstrahlung photon that is banked.*
7. *The electron exits the problem bounds and is terminated.*
8. *The first of the banked Bremsstrahlung photons exits the problem bounds and is terminated.*
9. *The second of the banked Bremsstrahlung photons exits the problem bounds and is terminated.*

Note that the scenario of Figure 4.1 describes only a single starting particle history. For just this history the Surface 2 tally is 3, as three photons crossed Surface 2 for this starting neutron. However, in order to be confident that the tally accurately represents the average behavior of photons crossing Surface 2 for each neutron crossing Surface 1, there should be a sufficient number of starting neutrons simulated such that the tally converges to a constant value. In general, the number of starting particles required depends on how common the tallying event is. The problem may require thousands, millions, or billions of starting particles, and in practice, MCNP returns statistics on the confidence level of the tally that indicate whether or not a sufficient number of starting particles were used. For the MCNP simulations of interest for this thesis work, the transport of GCR and the secondary particles produced by GCR through the Earth’s atmosphere was simulated and the secondary particle fluxes and energy spectra were tallied when crossing surfaces at 19 different altitudes.

Running the MCNP code requires an input file that contains a description of a geometry and materials, source particles, tallies of interest, and various particle transport options [Shultis, 2011; Werner, 2017]. MCNP simulates the radiation transport given conditions described in the input file and returns an output file with tally results and statistics on the confidence level of the results. In the following sections each feature of the input file and the interpretation of the output file are described. Specific examples relevant to this thesis work of the transport of radiation through the atmosphere are presented.

4.2.1. MCNP Input Geometry and Materials

The MCNP input file contains a geometry section, which describes a model of the physical matter in the radiation transport scenario of interest in the simulation. The user first defines surfaces such as planes, spheres, cylinders, and cones. From these surfaces different cells, i.e. volumes, are defined. Materials must likewise be specified and when defining the cells these materials are referenced and a density is provided. To limit the scope of the problem, there must be a boundary surface containing the entire simulation, and any particles that cross this boundary are terminated [Shultis, 2011; Werner, 2017].

The MCNP geometry of interest for this project needed to accurately represent the geometry of the Earth and especially its atmosphere. Simplistically, the Earth could be represented as a sphere of water surrounded by a second sphere of gas comprising the atmosphere. However, the atmosphere cannot be treated as a constant, as the density of the atmosphere at altitude 0 kilometers is more than 6 orders of magnitude greater than that of the density of the atmosphere at 100 kilometers [NOAA, 1976], i.e. the density of the atmosphere decreases exponentially with increasing altitude. Such a difference in density results in a great difference in interaction probabilities for particles traversing the medium. Thus, the Earth was modeled as a sphere of water surrounded by 100 concentric shells each with radius 1 kilometer greater than the last as shown in Figure 4.2. This provided enough data points for the atmosphere density and particle interaction probabilities at each altitude to be a reasonable approximation of reality. The atmosphere was modeled according to the 1976 standard atmosphere [Copeland, 2014; Copeland, 2017; NOAA, 1976]. Each 1 km thick shell of the atmosphere had a constant density and composition corresponding to the 1976 Standard Atmosphere description of the middle altitude of the shell. For example, the shell from 75 km to 76 km had density and composition corresponding to 75.5 km.

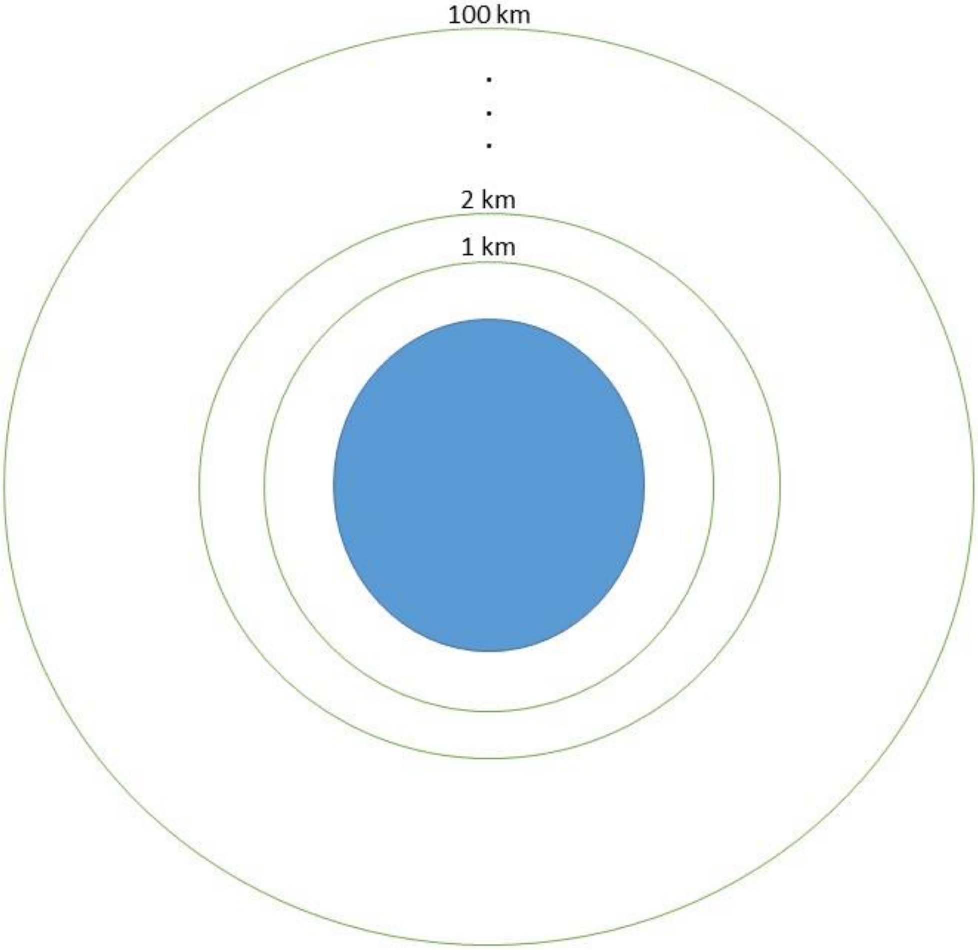

Figure 4.2: Displayed is the MCNP Geometry of the Earth and its atmosphere. The Earth was modeled as a sphere of water, and 100 concentric spheres surrounded it. Each spherical shell contains a different atmospheric composition and density as calculated from the 1976 U.S. Standard Atmosphere [NOAA, 1976].

4.2.2. MCNP Input Source Particles

The MCNP source particles are defined by position, particle type, starting energy, direction of flight, and several other less commonly adjusted default parameters. The particle starting position, particle type, starting energy, and direction of flight can be set as a single, constant value or as a distribution values. Hence, the position of starting particles could be a single point, defined across a surface, or defined throughout a volume. The particle type could be a single species or multiple species. Particles can be monoenergetic, defined across a discrete spectrum, or defined across a continuous spectrum. The direction of flight can be defined as isotropic, monodirectional, or by a function describing the probabilities of different directions of flight [Shultis, 2011; Werner, 2017].

For the input files of interest in this project, separate simulations were run for different GCR primary particles ranging from Hydrogen (Z=1) to Iron (Z=26). The starting particles were generated uniformly across the inner surface of the 100 kilometer altitude sphere with initial direction uniformly distributed from cos(-90°) to cos(90°) where the angle is taken with respect to a normal vector pointing to the center of the sphere. For each GCR a unique simulation was run for each of 19 discrete energies logarithmically spaced from 1 MeV to 1 TeV. Thus, 26×19 = 494 unique input files were used for simulations. Additional input files were constructed for further runs to verify results and to improve statistics.

4.2.3. Quantities Determined by MCNP Simulations

While it is possible to track every particle movement in MCNP, the user generally uses one of the standard tallies available in the program. A tally refers to counting, i.e. keeping tally, of the events of interest. The following table lists the standard MCNP tallies.

Tally Mnemonic	**Description**	**Units**
F1	Surface current	particles
F2	Surface flux	particles/cm^2
F4	Track length estimate of cell flux	particles/cm^2
F5	Flux at a point or ring detector	particles/cm^2
F6	Track length estimate of energy deposition	MeV/g
F7	Track length estimate of fission energy deposition	MeV/g
F8	Pulse height Tally	pulses

Table 4.1: Tally quantities available in MCNP [X-5 Monte Carlo Team, 2003].

The F1, F2, F6, and F8 tallies were of primary interest in this project. Note that these are all recorded in the MCNP output file in terms of per starting particle, i.e. each tally is divided by the number of starting particles. The F1 tally provides the total number of a species of particle crossing a surface, then divides this result by the total number of starting particles. The F2 tally is the F1 tally divided by the area of the surface of interest. The F6 tally is used to determine the total energy deposited in a cell divided by the total number of starting particles. The F8 tally is used to create an energy spectrum of the energy deposited in a cell. The F8 tally can be used to model a physical detector [X-5 Monte Carlo Team, 2003; Wilcox, 2014; Hughes, 2014].

For each of the simulations carried out for this work, an F2 type tally for surface flux per starting particle was used at 19 different altitudes, i.e. 19 of the spherical surfaces in Figure 4.2 were used as tallying surfaces. The tallied particles were neutrons, photons, electrons and positrons, positive and negative muons, protons, positive and negative pions, deuterons, tritons, helions, alphas, and heavy nuclei including lithium (Z=3) to iron (Z=26). Each particle tally was divided into energy 100 logarithmically spaced energy bins from 1 MeV to 1 TeV. For neutrons and photons an additional 100 logarithmically spaced energy bins from 10 eV to 1 MeV were included.

Note that electrons and positrons were tallied together, as were positive and negative muons, and positive and negative pions. These particles were separated later into negative and positive components using results from prior experiments and theory. Positive and negative electron fluxes were determined using the charge ratios as a function of energy presented in [Grieder, 2001] and then multiplying the total electron flux by the appropriate ratio. Figure 4.3 displays experimental and theoretical results for the electron to positron ratio at different atmospheric depths as provided by [Grieder, 2001].

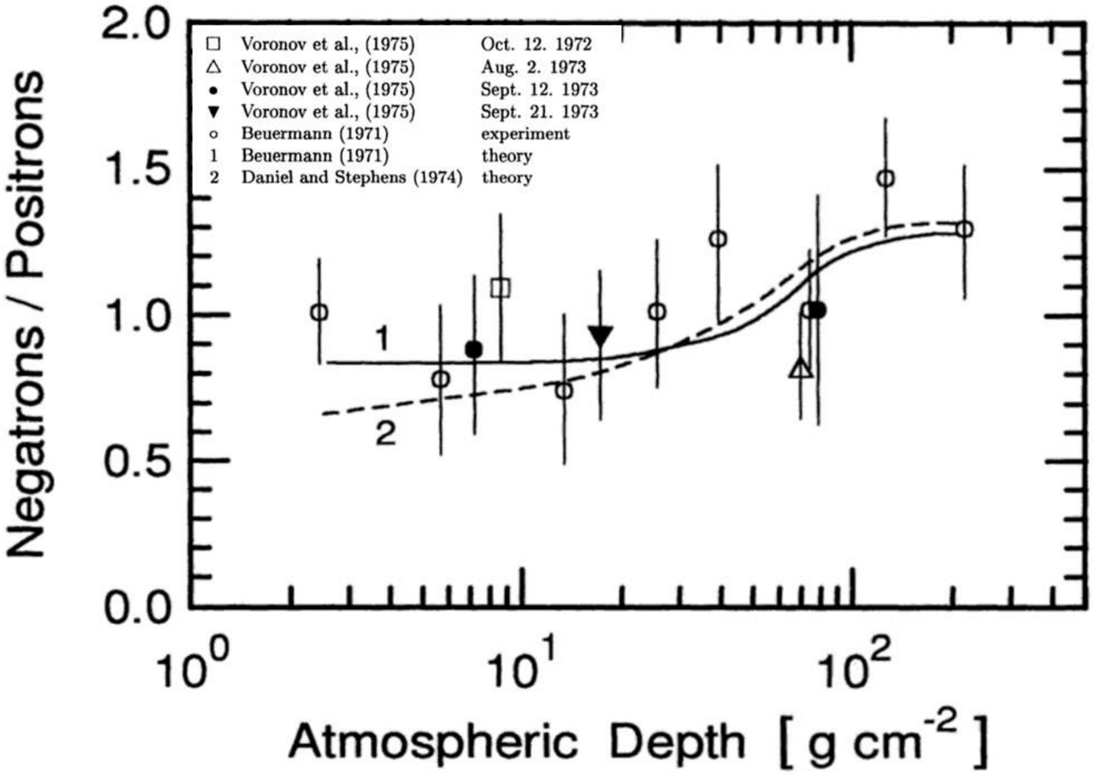

Figure 4.3: The charge ratio of electrons and positrons as found from different experimental and theoretical methods versus atmospheric depth [Grieder, 2001].

The relative flux of positive and negative muons was determined based on the muon charge ratios in different energy regions at different atmospheric depths given in [Grieder, 2001] and displayed in Figure 4.4.

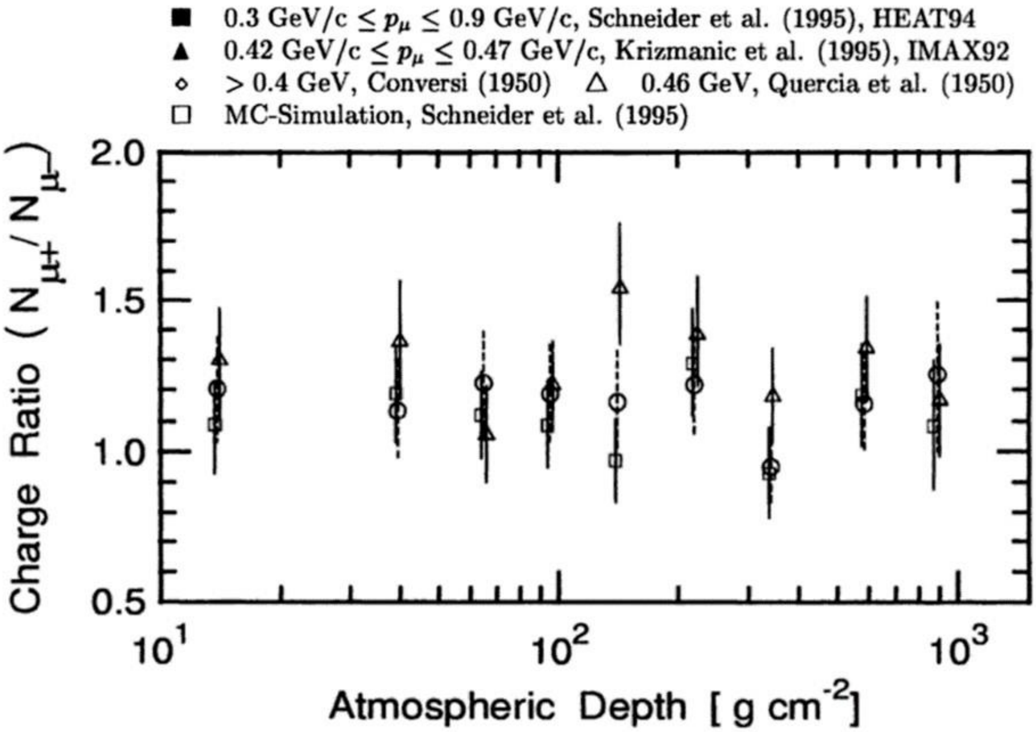

Figure 4.4: The charge ratio of positive to negative muons in different energy regions versus atmospheric depth [Grieder, 2001].

Although there exists no experimental data of the pion charge ratio in the atmosphere, from the chapter 2 discussion on air showers it was seen that the charged pions decay to muons with the same charge. This indicates that the pion charge ratio is likely nearly the same as the muon charge ratio. Therefore, the charge ratio data for muons shown in Figure 4.4 was also used to separate the pion flux into positive and negative portions.

4.2.4. MCNP Physics Options

MCNP is able to transport many particle types including neutrons, photons, electrons, positrons, protons, muons, pions, and heavy ions. Neutrons can be transported to a minimum energy of 0 eV, photons to 1 eV, electrons to 10 eV, and most other particles to 1 keV. Because experimental cross section data does not exist for every particle at every energy, physics models must be used to determine the probabilities of interactions for some cases. The maximum energy to which particles can be transported while maintaining reliable results is 1 TeV [Mashnik et al., 2017]. Figure 4.5 displays the different models and experimental data MCNP uses for each particle in different energy ranges [Waters, 2020]. These energies can be adjusted by the user, causing MCNP to neglect particles above or below an energy threshold. For the MCNP input files of this work, the maximum energy was raised to allow for the transport of 1 TeV particles.

The handling of particle collisions is another physics option that can be adjusted in MCNP. By default, MCNP does not propagate light ions that result from neutron nuclear collisions, where MCNP defines light-ions to be protons, deuterons, tritons, helions, and alphas [Werner, 2017]. For the MCNP simulations of this work, light ion recoil from neutron nuclear interactions was enabled.

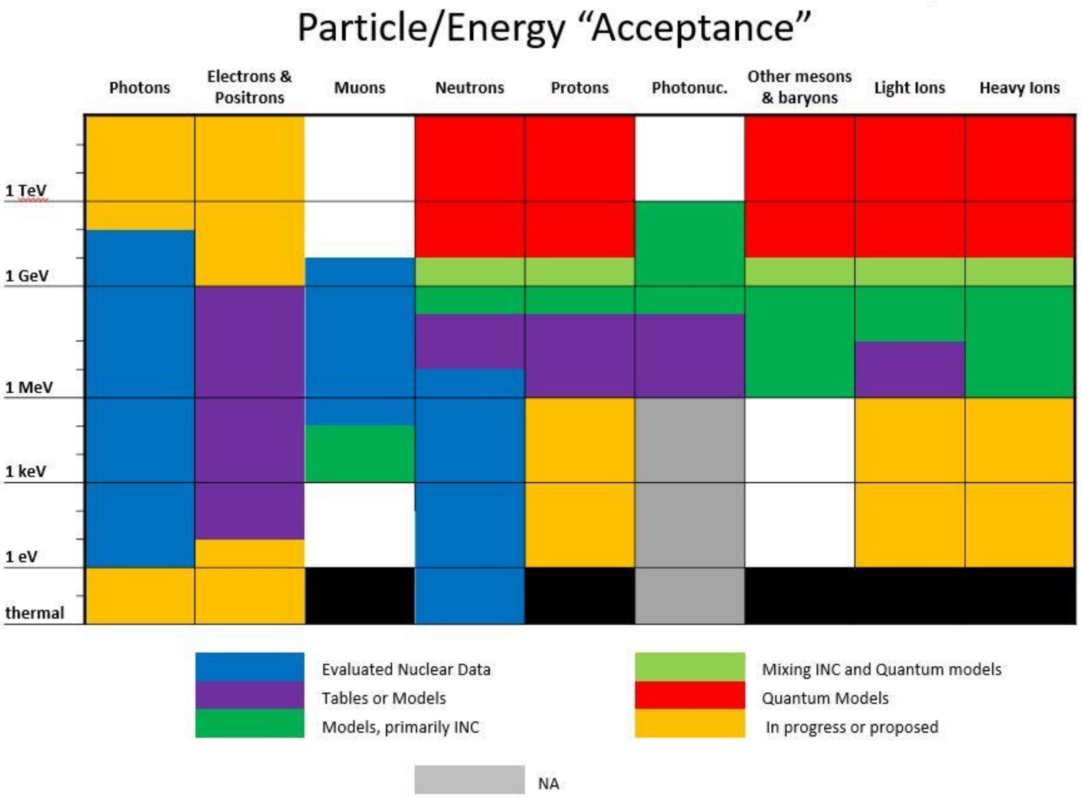

Figure 4.5: MCNP collision model used for particles in different energy ranges [Waters, 2020].

4.2.5. MCNP Statistics

In MCNP each starting particle history is treated as independent of all others. The distribution of each starting particle’s contribution to each tally is assumed to be identical, i.e. if x represents the contribution of a single starting particle history to a tally, then all starting particles have the same probability density function $f(x)$. Under these assumptions the central limit theorem (CLT) applies to the MCNP tally results. The true mean μ is given by

$$\mu = E(x) = \int x f(x) dx. \qquad 4.1$$

In practice the true mean is generally unknown and is approximated by the sample mean, defined as

$$\bar{x} = \frac{1}{N}\sum_{i=1}^{N} x_i. \qquad 4.2$$

Here, $\bar{x}$ is the sample mean, N is the number of starting particles, and x_i is the contribution to the tally from the i^{th} history. The variance of the population of x values is $Var(x)$, and is given by

$$Var(x) = \sigma^2 = \int \left(x - E(x)\right)^2 f(x)dx = E(x^2) - (E(x))^2. \qquad 4.3$$

Here, σ is the standard deviation of the population of x values. As is the case with the expected value, the true value of the variance is rarely known and is estimated by

$$S^2 = \frac{\sum_{i=1}^{N}(x_i - \bar{x})^2}{N-1} \approx \overline{x^2} - \bar{x}^2. \qquad 4.4$$

Here, S^2 is the estimated variance, S is the estimated standard deviation, and , $\bar{x}$, N, and x_i are as previously defined. The remaining term $\overline{x^2}$ is defined by

$$\overline{x^2} = \frac{1}{N}\sum_{i=1}^{N} {x_i}^2. \qquad 4.5$$

The true variance of the mean is denoted ${\sigma_{\bar{x}}}^2$ where $\sigma_{\bar{x}}$ is the true standard deviation of the mean. The true variance of the mean is given by the equation

$${\sigma_{\bar{x}}}^2 = \frac{\sigma^2}{N}. \qquad 4.6$$

In practice the true variance of the mean is generally unknown, and an estimate of the variance of the mean is used. The estimated variance of the mean is denoted ${S_{\bar{x}}}^2$ and is given by the equation,

$${S_{\bar{x}}}^2 = \frac{S^2}{N}. \qquad 4.7$$

Hence, the estimated standard deviation of the mean is $S_{\bar{x}}$. By the CLT the random variable,

$$Z_N = \frac{\bar{x} - \mu}{\sigma/\sqrt{N}} = \frac{\bar{x} - \mu}{\sigma_{\bar{x}}}, \qquad 4.8$$

converges to the standard normal random variable as N goes to infinity. The denominator contains the term for the true standard deviation of the mean, but when calculating the probability that $\bar{x}$ lies within an interval, the estimated standard deviation of the mean is used. Hence, the confidence that a tally $\bar{x}$ lies within two constant values a and b is given by,

$$\Pr[a < \bar{x} < b] = \Pr\left[\frac{a-\mu}{\sigma_{\bar{x}}} < \frac{\bar{x}-\mu}{\sigma_{\bar{x}}} < \frac{b-\mu}{\sigma_{\bar{x}}}\right] = \frac{1}{\sqrt{2\pi}}\int_{c}^{d} e^{-t^2/2}\, dt \approx$$

$$\Pr\left[\frac{a-\mu}{S_{\bar{x}}} < \frac{\bar{x}-\mu}{S_{\bar{x}}} < \frac{b-\mu}{S_{\bar{x}}}\right]. \qquad 4.9$$

Here the constants of integration c and d represent $\frac{a-\mu}{\sigma_{\bar{x}}}$ and $\frac{b-\mu}{\sigma_{\bar{x}}}$, respectively. MCNP reports uncertainty in terms of the estimated relative error R, defined as,

$$R = {}^{S_{\bar{x}}}\!/_{\bar{x}}. \qquad 4.10$$

The MCNP tally, along with its uncertainty, is reported as,

$$\bar{x}(1 \pm R). \qquad 4.11$$

This gives a one standard deviation confidence interval, meaning that if the MCNP simulation were rerun many times then 68% of the time the tally is expected to fall within the reported confidence interval. This does not indicate that a real world experiment of the same type as the MCNP simulation would result in a mean value within the interval from $\bar{x} - R$ to $\bar{x} + R$ 68% of the time.

By the CLT definition, Z_N only behaves as a standard normal random variable as N goes to infinity. In practice an infinite number of contributions to the tally is impossible, so the following table provides general guidelines for how many tallies must be recorded to achieve different values for R.

n	1	4	16	25	100	400
R	1	0.5	0.25	0.2	0.1	0.05

Table 4.2: Estimated relative error R vs. number of identical tallies n for large number of starting particle histories N [X-5 Monte Carlo Team, 2003].

The MCNP guidelines for acceptable values of R are given in the following table:

Range of R	Quality of the Tally
0.5 to 1	Garbage
0.2 to 0.5	Unreliable
0.1 to 0.2	Questionable
< 0.10	Generally reliable

Table 4.3: Guidelines for Interpreting the Relative Error R [X-5 Monte Carlo Team, 2003].

In the MCNP simulations of this work, the majority of the relative errors were below 0.10, putting them within the MCNP “generally reliable” range. However, some energy bins collect counts from rare events, and do not receive adequate counts to have reliable statistics. Rare events are inevitable in large scale MCNP simulations such as those of this project, but they have negligible effect on the average state of the atmospheric radiation environment. Thus, the small number of energy bins with “questionable,” “unreliable,” or even “garbage” quality tallies did not invalidate the overall results of the simulations. These MCNP reported uncertainties are only statistical uncertainties, i.e. they describe only the counting statistics of the tallies recorded by MCNP simulations, not the uncertainty of physical reality.

4.3. Interpolating the MCNP Results

For each of the 26 GCR species from hydrogen to iron, a unique MCNP simulation was run for each of 19 discrete energies logarithmically spaced from 1 MeV to 1 TeV. Thus, 26×19 = 494 unique input files were used for simulations. In each of these simulations, the secondary flux spectrum per GCR, i.e. Φ_{MCNP} had units of $\left(\frac{secondaries}{cm^2\ GCR}\right)$ and was tallied for 37 different secondary particle species (neutrons, photons, electrons and positrons, positive and negative muons, protons, positive and negative pions, deuterons, tritons, helions, alphas, and heavy nuclei including lithium to iron) at 19 discrete altitudes. The MCNP simulation geometry and tallies are shown in Figure 4.6.

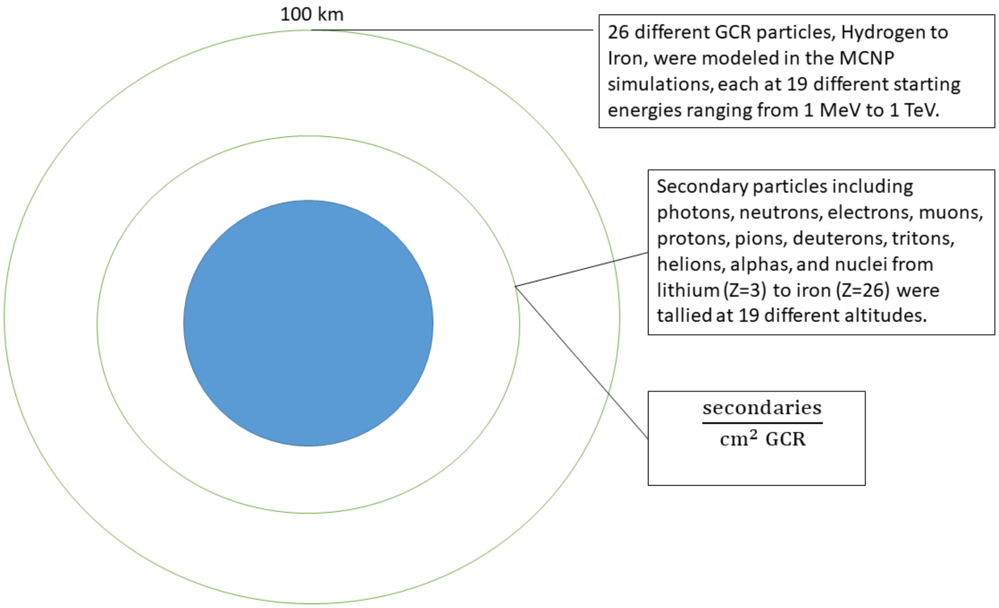

Figure 4.6: The geometry and tallies of the MCNP simulations. Each simulation used one monoenergetic GCR particle species as source particles and tallied each of the secondary particle species crossing spherical surfaces at 19 different altitudes.

Although in MCNP simulations a discrete number of monoenergetic GCR particles were simulated, in reality the GCR flux spectrum is continuous. The red vertical lines from Chapter 3 Figure 3.2 display the 19 discrete energy values simulated in MCNP along with the actual continuous spectrum. While any continuous phenomenon requires a discrete approximation to model, the 19 energy values were insufficient to adequately represent the GCR flux spectrum. In order to determine Φ_{MCNP} due to any GCR energy in the interval from 1 MeV to 1 TeV at each of the 19 discrete altitudes, a continuous model was fit to the discrete data. Linear spline interpolation was used to fit the 19 GCR energies and their corresponding Φ_{MCNP}, yielding functions that were used to determine Φ_{MCNP} due to any intermediate GCR energy, for a given the GCR particle species and altitude. Using for loops in code, this process of fitting the MCNP data of Φ_{MCNP} versus GCR energy with a linear spline interpolation was repeated for each GCR particle species and each of the 19 MCNP altitudes used for tallying. One example of results from the linear spline interpolation of Φ_{MCNP} versus GCR energy is displayed in Figure 4.8. Here, the MCNP data contained Φ_{MCNP} of neutrons at 21 kilometers due to GCR protons of 1×10^5 MeV and of 2×10^5 MeV. Using linear spline interpolation, the neutron Φ_{MCNP} due to GCR protons of 1.52×10^5 MeV was found.

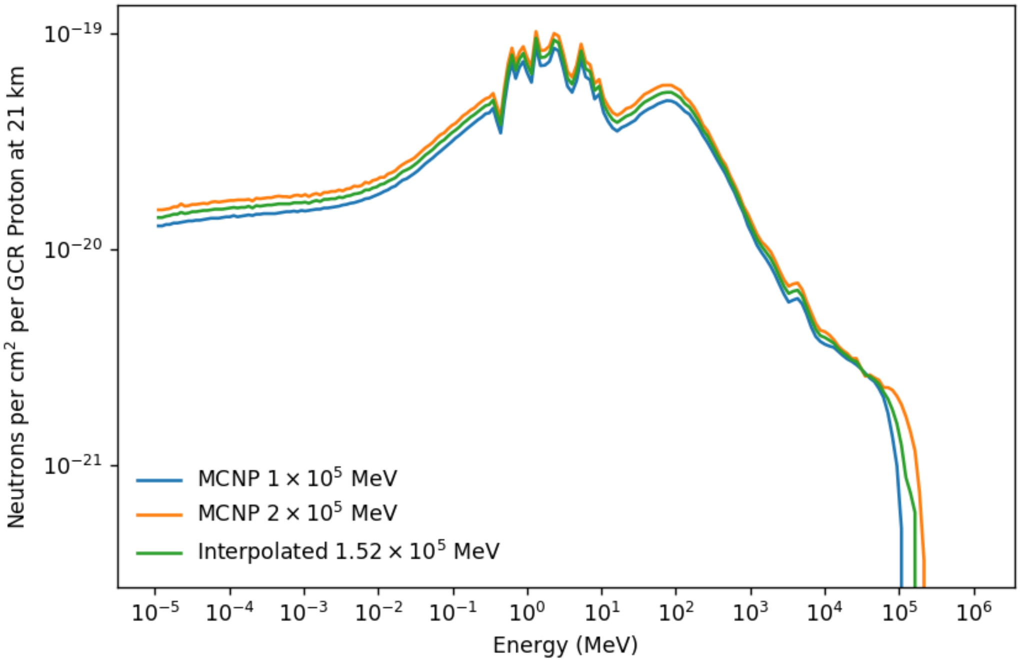

Figure 4.7: At an altitude of 21 kilometers the neutron Φ_{MCNP} due to GCR protons of different initial energies.

For most GCR species Φ_{MCNP} was found as described above. However, for the cases in which the GCR species and secondary species were the same, e.g. the proton Φ_{MCNP} due to GCR protons, a different approach was taken. The secondary flux spectra per GCR of the same species as the GCR particle often contained a significant number of GCR particles that retained almost all of their initial energy, resulting in a spike in Φ_{MCNP} in the energy bin corresponding to the GCR energy. This phenomenon of GCR primaries causing a spike in Φ_{MCNP} is displayed in Figure 4.7. Here, both 1×10^5 MeV GCR protons and of 2×10^5 MeV GCR protons were simulated in MCNP, and the proton Φ_{MCNP} was tallied at an altitude of 21 kilometers. Note that the proton Φ_{MCNP} due to 1×10^5 MeV GCR protons has a spike in the energy bin containing 1×10^5 MeV, indicating that many of the GCR protons retain the vast majority of their energy from the top of the atmosphere to an altitude of 21 kilometers. The same feature is present in the proton Φ_{MCNP} due to 2×10^5

MeV GCR protons. Also shown is the linear spline interpolation for the proton Φ_{MCNP} due to GCR protons with energy between the two GCR energies simulated in MCNP. This linear spline interpolation was performed while treating all Φ_{MCNP} energy bin values identically. However, this spectrum does not match the shape of either of the spectra resulting from the MCNP simulations. Given GCR energy of 1.52×10^5 MeV the resulting secondary proton flux spectrum should have a spike in flux in the bin containing 1.52×10^5 MeV.

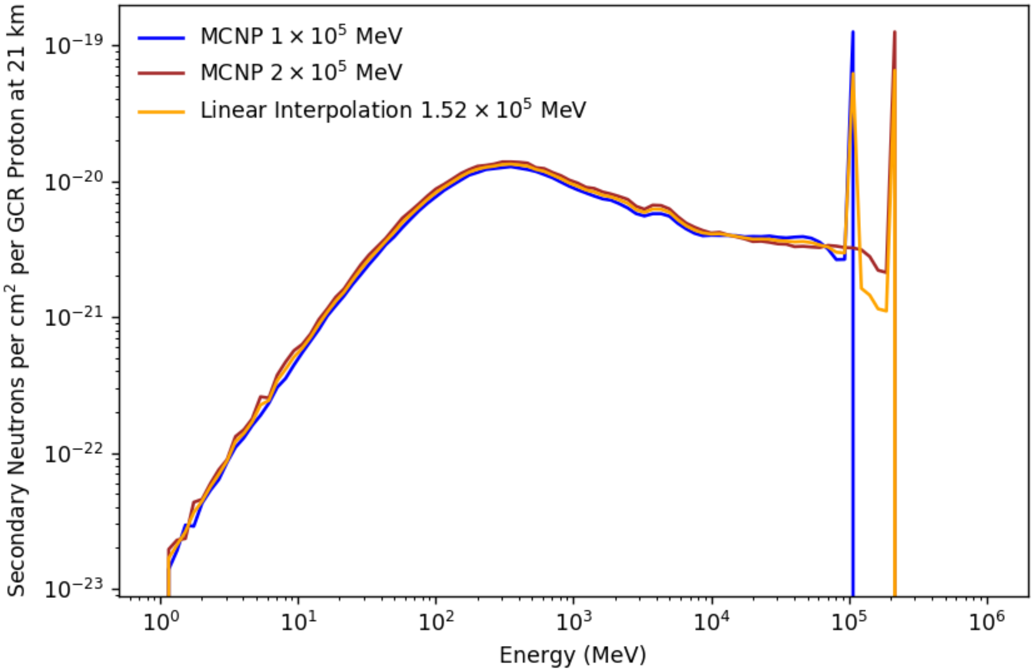

Figure 4.8: Secondary proton flux spectra from MCNP and an incorrect interpolated spectrum.

To correct the spectral shape, the secondary flux bin containing the GCR energy, as well as the three nearest lower energy neighbors, were each interpolated separately from the other secondary flux bins. Rather than interpolating the peak based on the secondary bin values from the MCNP produced spectra, the peak was interpolated based on the peak values from the MCNP spectra, regardless of which secondary bins contained those peaks. The corrected spectrum is displayed in Figure 4.9.

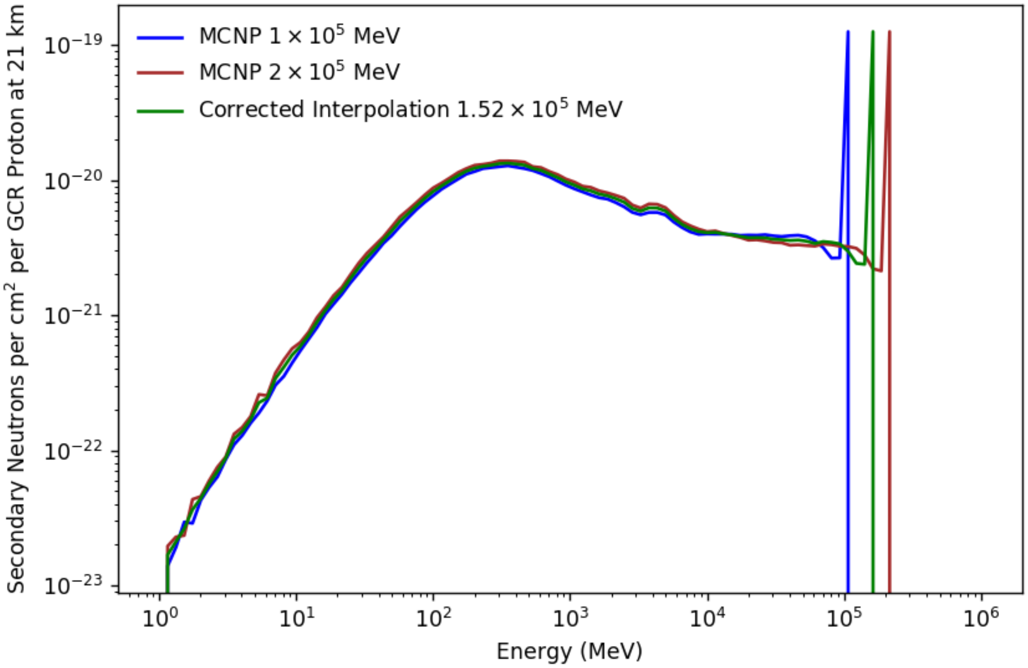

Figure 4.9: The proton Φ_{MCNP} and the corrected interpolated spectra formed by separately interpolating the peak and the other secondary bins.

Using the functions acquired by interpolating the Φ_{MCNP} versus GCR energy data, the 19 MCNP simulated GCR energies were expanded to 100 GCR energies, i.e Φ_{MCNP} was determined at 19 different altitudes due to 26 different GCR species each of 100 different starting energies. These 100 GCR energies were a much closer approximation to the continuous GCR flux spectrum than were the 19 MCNP simulated energies.

The Φ_{MCNP} for each secondary particle species were made at 19 discrete altitudes. However, Φ_{MCNP} at any altitude from 0 km to 100 km is of interest. A continuous model was fit to the discrete data at 19 altitudes to determine Φ_{MCNP} at any altitude. Cubic spline interpolation was used to fit the 19 MCNP simulated altitudes and their corresponding Φ_{MCNP}, yielding functions that were used to determine Φ_{MCNP} at any intermediate altitude due to any of the 26 simulated GCR particle species and any of the 100 interpolated GCR energies. The actual altitude for which Φ_{MCNP} was calculated depended upon the user input. For each altitude specified by the user, AIREC uses a for loop to fit the Φ_{MCNP} versus altitude data for every GCR particle and energy. Figure 4.8 displays an example interpolation for the total neutron Φ_{MCNP}, i.e. the integrated spectrum, resulting from 100 GeV GCR protons versus altitude. A single interpolated neutron Φ_{MCNP} spectrum compared to simulated Φ_{MCNP} spectra is displayed in Figure 4.9.

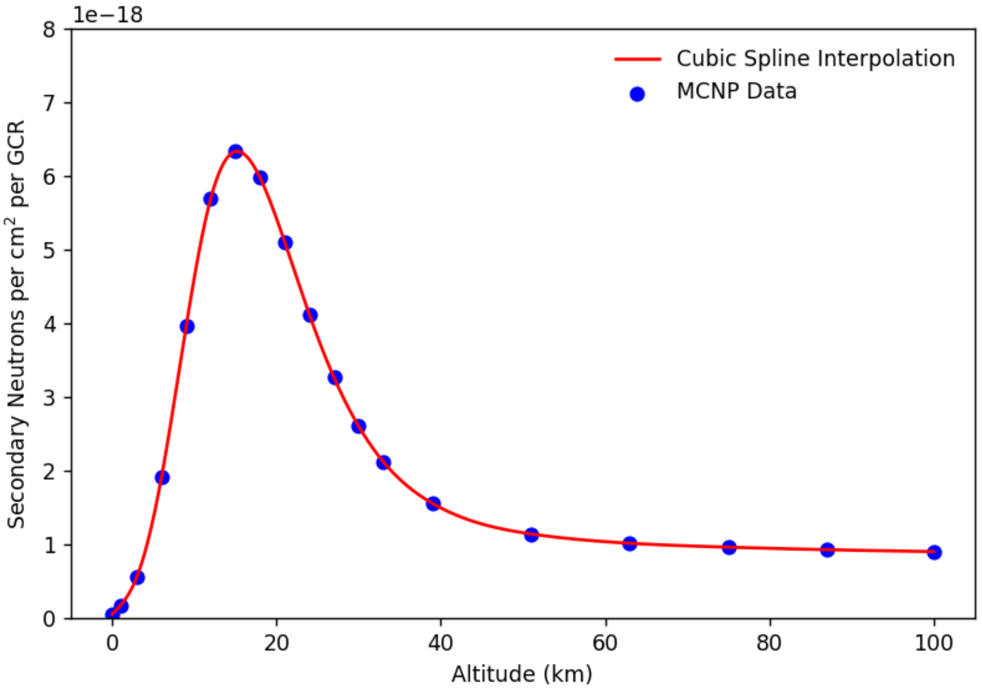

Figure 4.10: The neutron Φ_{MCNP} tallied in MCNP simulations along with a cubic spline interpolation of the data.

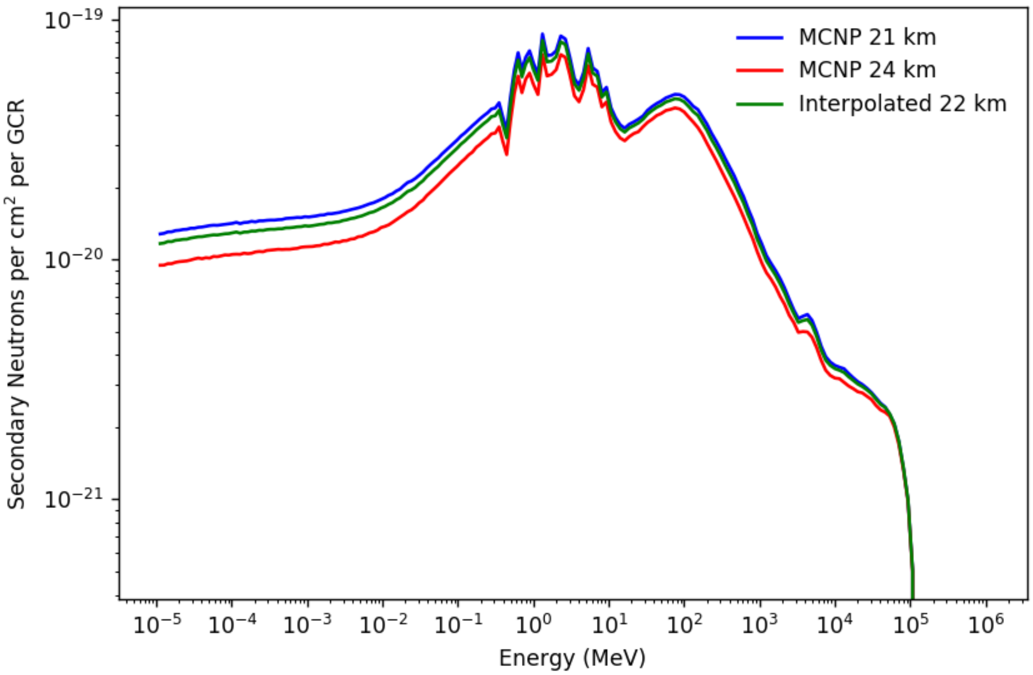

Figure 4.11: An interpolated secondary neutron flux spectrum at 22 km compared to MCNP secondary neutron spectra tallied at 21 km and 24 km. All displayed spectra resulted from 100 GeV GCR protons.

4.4. The Galactic Cosmic Ray Flux

Referring back to the flowchart of Figure 3.3, models for three physical phenomena were required: EAS, GCR incident at the top of the Earth's atmosphere, and the geomagnetic field. The MCNP simulations of EAS and the interpolation of the MCNP data returned the secondary particle flux that results from a single GCR primary particle of a given species and energy $\left(\frac{secondaries}{cm^2\ GCR}\right)$. The International Standards Organization (ISO) and International Geomagnetic Reference Field (IGRF) models were used to calculate the GCR incident at the top of the Earth's atmosphere and the geomagnetic field strength, respectively. The ISO GCR model was used to calculate the GCR flux spectrum as a function of time. The time is relevant, because as shown in Chapter 2 Figure 2.4, the GCR flux spectrum varies inversely with solar intensity. Once the GCR flux spectrum is determined as a function of time, the global coordinate (latitude, longitude, altitude) must be considered. The geomagnetic field strength varies as a function of both the coordinate and time. The IGRF model is used to calculate the geomagnetic rigidity for the time and coordinates of interest.

Figure 4.12 displays the GCR proton flux spectrum for June 2010. The figure also shows the minimum energy necessary for protons to enter the atmosphere at several different latitudes with constant longitude of 0° and constant altitude of 20 km. This minimum energy was calculated by converting the vertical cutoff rigidity (VCR) to the corresponding energy. Although the GCR flux energy spectrum of Figure 4.10 appears to be continuous, in practice, for AIREC calculations the ISO GCR flux spectrum is divided into 100 discrete energy bins. The VCR acts as a high pass filter; if the GCR flux in the bin has an energy greater than the energy corresponding to the VCR, it contributes to the SSAIRE, otherwise it does not. For example, in Figure 4.12 at a latitude of 30° only the GCR primary particles with energy greater than 10^4 MeV contribute to the SSAIRE. If only a portion of the bin has particle rigidity greater than the VCR, then only that fraction contributes to the SSAIRE. For example, if the VCR is 5.5 GV, and the GCR flux bin ranges from 5 GV to 6 GV, then only half of the flux in that bin contributes to the SSAIRE.

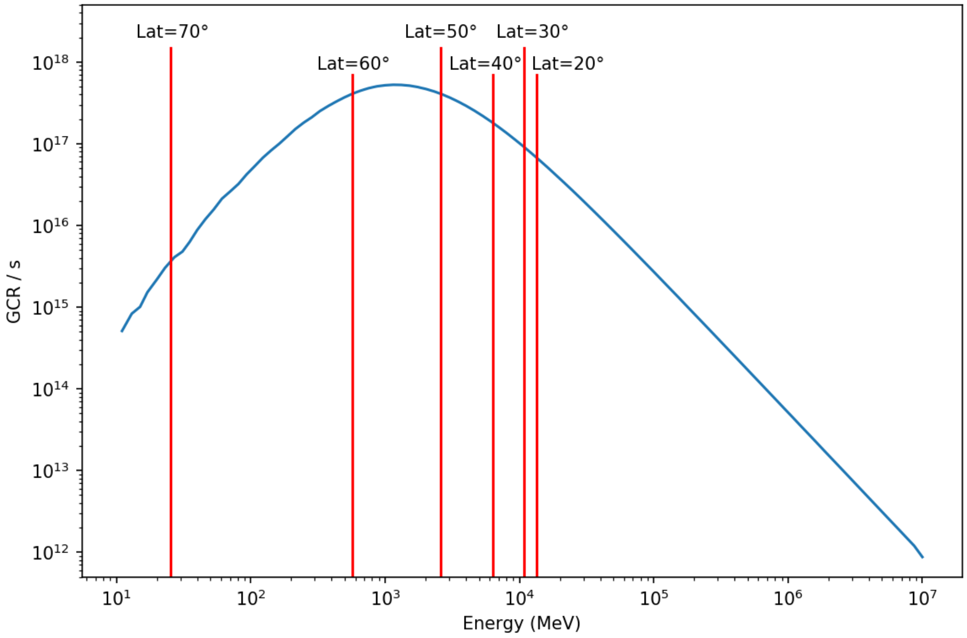

Figure 4.12: The ISO model GCR proton flux spectrum, and the VCR converted to energy for several latitudes with constant longitude of 0° and constant altitude of 20 km.

For each GCR flux spectrum energy region that contributes to the SSAIRE, the GCR flux is multiplied by the corresponding MCNP secondary particle flux per GCR to determine the magnitude of its contribution

$$\Phi_{MCNP} \times \Phi_{GCR} = \Phi = \left(\frac{secondaries}{cm^2\ GCR}\right)\left(\frac{GCR}{s}\right) = \frac{secondaries}{cm^2\ s}$$

The total secondary particle flux is found by adding the secondary particle flux due to each GCR particle species in each energy region,

$$\Phi_{tot} = \sum_{GCR\ Species}\left(\sum_{GCR\ Energy} \Phi_{MCNP} \times \Phi_{GCR}\right).$$

4.5. Uncertainty in Results

As stated in section 4.2.5 MCNP statistics, the uncertainty in the MCNP tally results is uncertainty due to counting statistics, not real world uncertainty. This statistical uncertainty can be propagated throughout the interpolation of the MCNP tally results as described in section 4.3, i.e. the uncertainty due to each of the MCNP tally values used in interpolation could be used as inputs in a function to determine the net statistical uncertainty, but this calculation would not provide the desired real-world uncertainty.

The discrepancy between the statistical uncertainty and the real-world uncertainty results from the lack of reported uncertainties in reaction cross sections used in radiation transport codes. In MCNP simulations every time a projectile particle interacts with a target particle, MCNP looks up the relevant reaction cross sections in order to determine the probabilities of different outcomes resulting from the interaction. Each interaction result should have an accompanying uncertainty due to the cross section uncertainty. One simulated projectile particle may undergo many interactions throughout its history and each interaction result is calculated from a cross section that should have an accompanying uncertainty. The uncertainty from each interaction should be propagated to determine a total uncertainty for the particle. However, neither MCNP nor any other Monte Carlo radiation transport code has data on reaction cross section uncertainty.

The determination of the uncertainties in cross section values has been a long standing problem in the Monte Carlo radiation transport code community. The MCNP cross sections result either from experiment or from theory. In the case of experimentally verified cross section values, it is feasible that uncertainties for the cross sections could be determined. In theoretical calculations it is less clear how the cross section uncertainty could be determined. This large scale problem of determining reaction cross section uncertainties is intractable and lies beyond the scope of the work of this thesis.

Although the cross section uncertainties are unknown, it is believed that the total uncertainty in AIREC results is primarily due to the uncertainty in the cross sections rather than the uncertainty in MCNP counting statistics. This conclusion was reached by consideration of the reported uncertainty in results from atmospheric radiation dosimetry codes [Bottollier-Depois et al., 2012]. The EURADOS Report on the comparison of multiple radiation exposure codes found that the codes were generally in agreement with the median value of all tested codes to within ±20% [Bottollier-Depois et al., 2012]. Although this is a considerable amount of uncertainty, radiation dosimetry experimental measurements generally have uncertainties of ±20% to ±30% [Bottollier-Depois et al., 2012].

In light of the EURADOS Report estimate of ±20%, it is reasonable to use this uncertainty for AIREC values. However, the AIREC uncertainty should be lower than that of radiation dosimetry codes. Radiation dosimetry codes convert radiation flux to dose rate by the use of fluence to dose conversion factors. These fluence to dose conversion factors often have a large amount of uncertainty in their value, adding additional uncertainty to the radiation dose value. Because AIREC returns the secondary particle flux spectrum and not a dose, the additional uncertainty due to fluence to dose conversion factors is never introduced. Nevertheless, all AIREC results are conservatively assumed to have an uncertainty of ±20%.

4.6. Concluding Remarks

The MCNP output files resulting from Copeland's development of CARI-7 were expanded through interpolation to include secondary particle fluxes that were not tallied in the original simulations. From these interpolations the secondary particle flux per GCR could be calculated at any altitude from 0 to 100 kilometers due to any GCR from hydrogen (Z=1) to iron (Z=26) of any energy from 1 MeV to 1 TeV. This secondary particle flux per GCR information when combined with the GCR spectrum model described in Chapter 4 gives an accurate description of the atmospheric radiation environment absent the geomagnetic field.

CHAPTER V

VERIFICATION AND VALIDATION OF AIREC

AIREC is one of the first computer models designed to estimate the secondary particle flux from GCR-initiated air showers in the atmosphere. To properly validate the model, it is important to compare AIREC results with empirical measurements made in the atmosphere. Unfortunately, there is a serious lack of such measurements on which to base such comparisons and in some cases, the required experimental data would be nearly impossible to obtain due to practical difficulties in operating large radiation detectors and high altitudes for sufficiently long periods of time to obtain statistically useful measurements. For example, AIREC can return the secondary pion flux spectrum at 70 kilometers above the equator. For January 2020 at 0° N, 0° E, and 70 km, AIREC calculates the secondary pion flux to be 3.4×10^{-6} pions $(\text{cm}^2\ \text{s})^{-1}$, i.e. about 2 pions would cross a 1 cm^2 detector per week. Experimental verification of this result would require a detector capable of discriminating between pions and other charged particles and of measuring the pion energy spectrum. A detector capable of making such a measurement would be quite large, consisting of multiple independent detectors separated by layers of high density material such as lead and perhaps using a powerful magnet operating as a particle velocity selector. Due to the low flux, this hypothetical pion detector would require months of measurements to obtain statistically significant results. The detector would require an apparatus to maintain its position during those months. The cost and infeasibility of such an experiment make it all but impossible to ever carry out.

An extensive review of the literature revealed atmospheric radiation environment data from a modest number of experiments and model simulations that can be compared with AIREC results. This data includes only a discrete number of dates and locations in the atmosphere. These results from the literature are compared to the corresponding AIREC results in this chapter.

5.1. Experiments

Neutron ground monitors are used to detect the secondary neutron flux at the surface of the Earth as a way to measure primary GCR flux at the top of the atmosphere and as a monitor of space weather, i.e. solar activity-induced interactions between the interplanetary and geomagnetic fields. The neutron monitor operated in Thule, Greenland has publicly available data of neutron flux over time, which is displayed in Figure 5.1, alongside comparable data calculated using AIREC. The sinusoidal variation in secondary neutron intensity results from solar modulation of the GCR flux. The Thule neutron monitor data variation is a measurement that varies as a direct result of the solar modulation of GCR flux. In AIREC the ISO model is used to determine the solar effects on the GCR flux. The sunspot number is used as a proxy for solar wind intensity, i.e. the sunspot number is used as an input for a model of solar modulation of GCR flux. Thus, the AIREC method of calculating the effects of solar modulation and the Thule ground monitor measurements are independent of one another, yet both show the same sinusoidal variation in neutron flux versus time. The Thule data shows more variation in peak and trough height from cycle to cycle than does the AIREC data. The AIREC peaks are generally broader, plateauing across time at the maxima. Ultimately, this comparison is demonstrative of the ISO model's accuracy in tracking the GCR intensity, and gives negligible information about AIREC as a whole. The difference between the sunspot and neutron monitor methods for tracking solar activity indicates that a future version of AIREC would benefit from having an option to use either method.

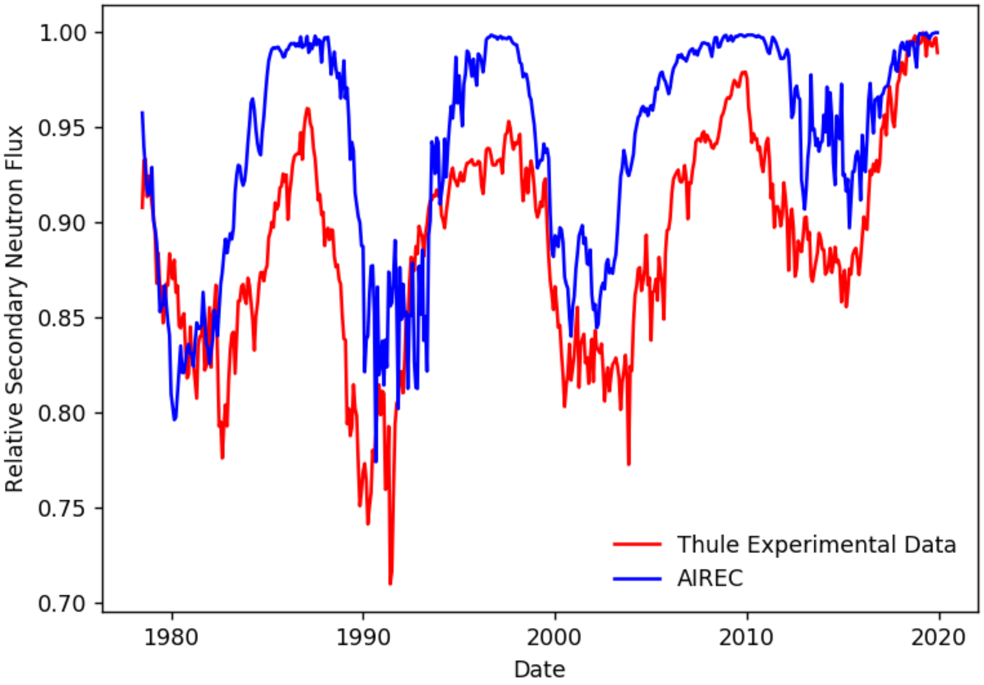

Figure 5.1: Experimental data and AIREC calculated data for relative neutron flux versus time at Thule, Greenland (76.5° N, 68.7° W, 26 m) [Bartol Institute].

Experiments to determine a neutron spectrum are difficult, because neutrons do not directly ionize matter. Thus, secondary events resulting from neutron nuclear reactions that produce charged particles or gammas must be detected, and the original neutron energy is inferred from these secondary particles [Krane, 1988]. Neutron spectrum measurements are generally conducted using a Bonner sphere spectrometer (BSS). These detectors consist of an array of spheres of different diameters, each of which has different amounts of shielding. The varying amount of shielding are used to slow incident neutrons of various energies sufficiently, such that they will undergo nuclear interactions, producing secondary particles that can be detected. Thus, each sphere is selected to be sensitive to a different energy range of neutrons.

The pulse height spectrum that results from a neutron spectral experiment using a BSS does not match the shape of the actual neutron spectrum. In order to interpret a BSS measurement, there must be prior knowledge as to the sensitivity of each Bonner Sphere to neutrons of different energies. For a given sphere the count rate versus energy is known as the response function of the sphere. The collection of response functions for all of the spheres of the BSS is known as the response matrix. Originally, response functions were determined experimentally by exposing spheres of various diameters to neutrons of different energies [Bramblett et al., 1960]. Currently, response functions are generally determined from Monte Carlo radiation transport simulations. Each sphere of a given diameter is exposed to monoenergetic neutron beams in a variety of simulations, covering a range of neutron energies [Mares et al., 1991; Goldhagen et al., 2002].

Once the response functions and pulse height spectrum from the experiment are known, the actual incident neutron spectrum is determined by a process known as unfolding. The unfolding process requires an initial guess of the neutron spectrum shape. This hypothetical neutron spectrum is then used as an input into the response functions, which results in a model pulse height spectrum. If this model pulse height spectrum matches the actual pulse height spectrum acquired from the experiment, then it is assumed that the hypothetical neutron spectrum matches the actual neutron spectrum, and the unfolding process ends. If the model pulse height spectrum does not match the actual pulse height spectrum, then the initial guess of the neutron spectrum is adjusted, and the process is repeated. This continues until the hypothetical neutron spectrum results in a model pulse height spectrum that matches the experimental pulse height spectrum [Goldhagen et al., 2002; Goldhagen et al., 2002; Perey, 1977; Reginatto, 2010].

Thus, any BSS neutron spectrum measurement is highly dependent upon *a priori* assumptions, namely the cross sections used by the Monte Carlo radiation transport code used in determining the response functions, the unfolding algorithm used, and the initial guess of the neutron energy spectrum. Results from an experiment are therefore not unique. The results of neutron spectral measurements are often plotted as lethargy versus energy. Recall from chapter 3 section 3.2 that the lethargy is the product of the differential flux (y-value) and the average bin energy (x-value). This exaggerates distinctions between features of the spectrum, making the lethargy a useful plot for visualization.

A neutron spectral experiment was conducted at the High Altitude Research Station in Jungfraucjoch, Switzerland at the coordinates 46.55° N, 7.98° E, and 3.585 km using a BSS [Mares et al., 2020]. These experimental results, together with the corresponding AIREC calculations, are displayed as lethargy spectra in Figure 5.2. The Jungfraucjoch experimental results have a peak between 1 and 10 MeV and a second, higher peak above 100 MeV. In contrast, the AIREC results have a higher peaked region from 1-10 MeV and a second, lower peak above 100 MeV. The AIREC peak from 1-10 MeV is much wider and has several local minima and maxima throughout this energy region, while the Mares data in this energy range contains a single peak that is nearly symmetrical.

For each spectrum the peak near 1 MeV results from evaporation neutrons [Goldhagen et al., 2004]. Evaporation neutrons can result following nuclear interactions between energetic hadrons and target nuclei. A target nucleus can absorb a projectile particle or a portion of its kinetic energy, enter an excited state, then emit another particle (or particles). The process of the nucleus emitting particles following excitation is referred to as evaporation, and if the emitted particle is a neutron it is referred to as an evaporation neutron [Krane, 1988; Russell, 1990]. The intermediate state of the nucleus is referred to as a compound nucleus. This interaction is represented symbolically as

$$a + X \rightarrow C^{*} \rightarrow Y + b.$$

Here, a is the initial projectile particle, X is the target nucleus, C^{*} is the compound nucleus (the asterisk indicates an excited state), Y is the nucleus following de-excitation, and b is an evaporation particle [Krane, 1988]. Evaporation neutron energies are typically below 20 MeV [Russell, 1990], which makes evaporation neutrons a plausible explanation for the peak seen around 1 MeV in the neutron spectral data.

Each of the AIREC and [Mares et al., 2020] neutron spectra contain a peak around 100 MeV. This peak is most likely the result of neutrons produced through intranuclear cascades. An energetic projectile hadron with sufficient energy can cause spallation of a target nucleus, releasing the constituent hadrons of the nucleus as energetic secondary particles [Schraube, et al. 1997; Russell, 1990]. The hadrons resulting from intranuclear cascades typically have energies greater than 20 MeV [Russell, 1990], making intranuclear cascades a plausible explanation for the peak seen around 100 MeV in the neutron spectral data.

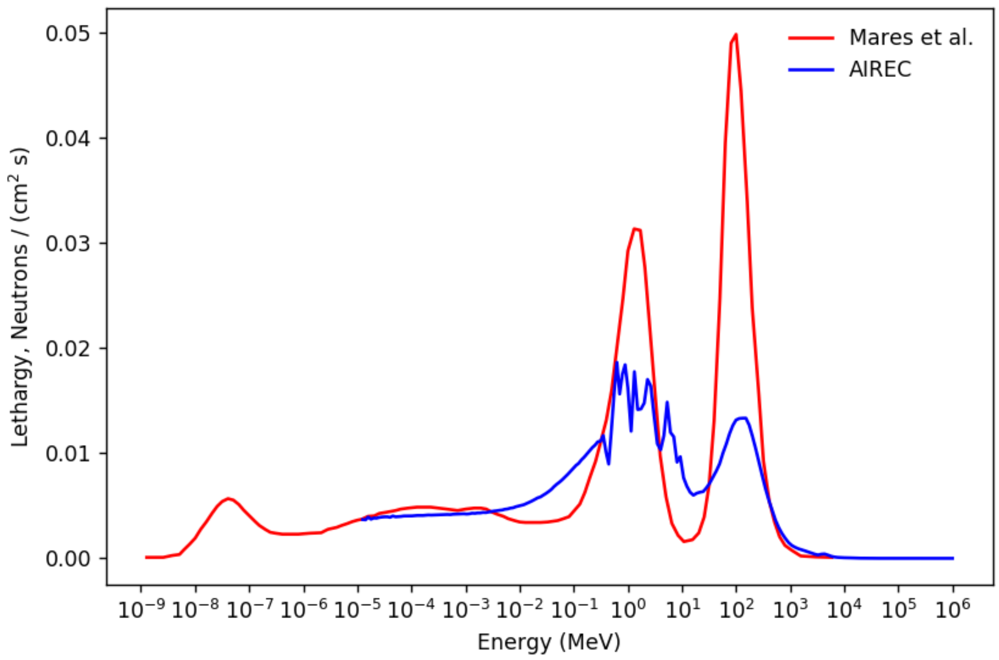

Figure 5.2: Experimental data and AIREC calculated data for the neutron spectrum at the High Altitude Research Station in Jungfraucjoch, Switzerland at the coordinates 46.55° N, 7.98° E, and 3.585 km in September of 2018 [Mares et al., 2020].

There are several potential causes of the discrepancies between the [Mares et al., 2020] experiments and AIREC results. [Mares et al., 2020] used MCNP4 and LAHET Monte Carlo radiation transport codes for calculating Bonner sphere response functions [Mares et al., 1998; Mares et al., 2020]. The data on from which AIREC was developed resulted from MCNPX simulations. The Mares data was unfolded using an in house version of the MSANDB code, and different unfolding methods can produce different results [Mares et al., 2020]. The most likely source of disagreement is that the Mares measurements were made at an altitude of 3.585 km, but these were still ground based measurements. In the MCNP simulations used to develop AIREC, the surface of the Earth is treated as a uniform sphere of water at an altitude of 0 km. Hence, 3.585 km in AIREC is in the air well away from the Earth's surface. The Mares data likely includes back scatter radiation from the ground that is not present in the AIREC data. The [Mares et al., 2020] paper also describes the difficulty with backscattered neutrons due to snow at the site. Figure 5.3 includes a normalized AIREC neutron spectrum for the same latitude and longitude but at ground level. Because the surface of the Earth in the MCNP simulations used to develop AIREC was water, this provides a good comparison to the Mares data where the ground was covered in snow.

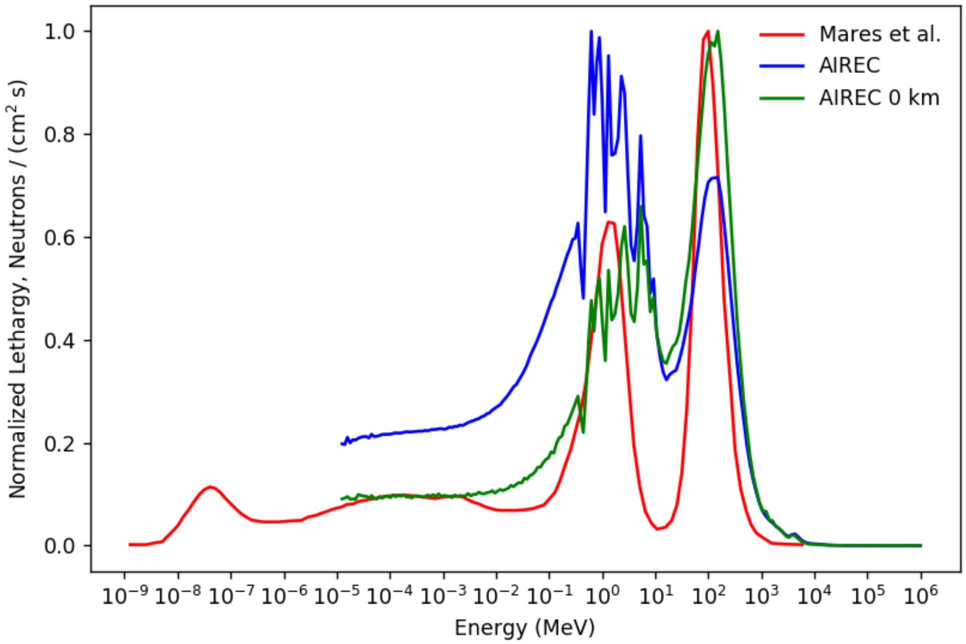

Figure 5.3: Experimental data and AIREC calculated data for the neutron spectrum at the High Altitude Research Station in Jungfraucjoch, Switzerland [Mares et al., 2020]. Also included is AIREC data at ground level.

This data raises the question as to why the neutron spectrum peak around 100 MeV is relatively higher than the 1 MeV peak near the ground. Figure 5.4 displays the total reaction cross sections versus energy for neutrons incident on nitrogen-14 and oxygen-16. The total reaction cross section of a 1 MeV nitrogen on nitrogen-14 is 2.34 barns [Chadwick and Young, 2011] and on oxygen-16 is 8.15 barns [Hale et al., 2011]. The total reaction cross section of a 100 MeV nitrogen on nitrogen-14 is 0.55 barns [Chadwick and Young, 2011] and on oxygen-16 is 0.64 barns [Hale et al., 2011]. The much lower cross sections of higher energy neutrons result in less absorption and deflection of these neutrons as an EAS propagates towards the surface of the Earth. Figure 5.5 displays unnormalized AIREC neutron lethargy spectra from 3.585 km, the height of the [Mares et al., 2020] experiment, down to 0 km. Note that the 1 MeV neutron peak decreases more rapidly than the 100 MeV peak does, as expected given the reaction cross sections. This results in the observed shift in relative peak heights.

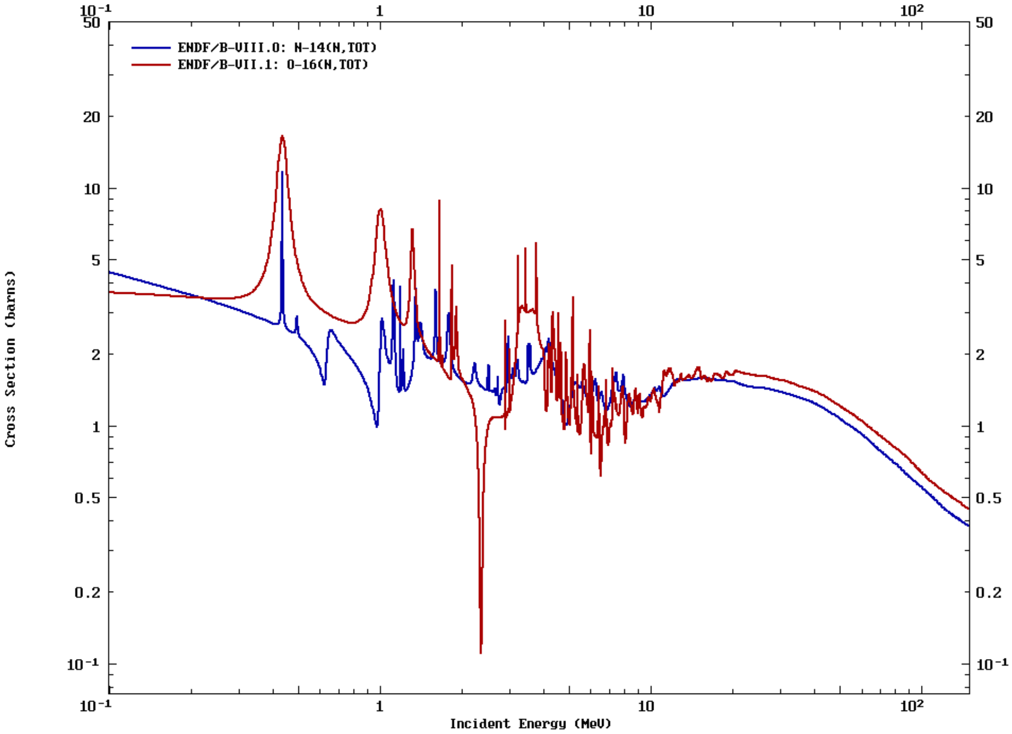

Figure 5.4: Total reaction cross sections for neutrons on nitrogen-14 [Chadwick and Young, 2011] and oxygen-16 [Hale et al., 2011].

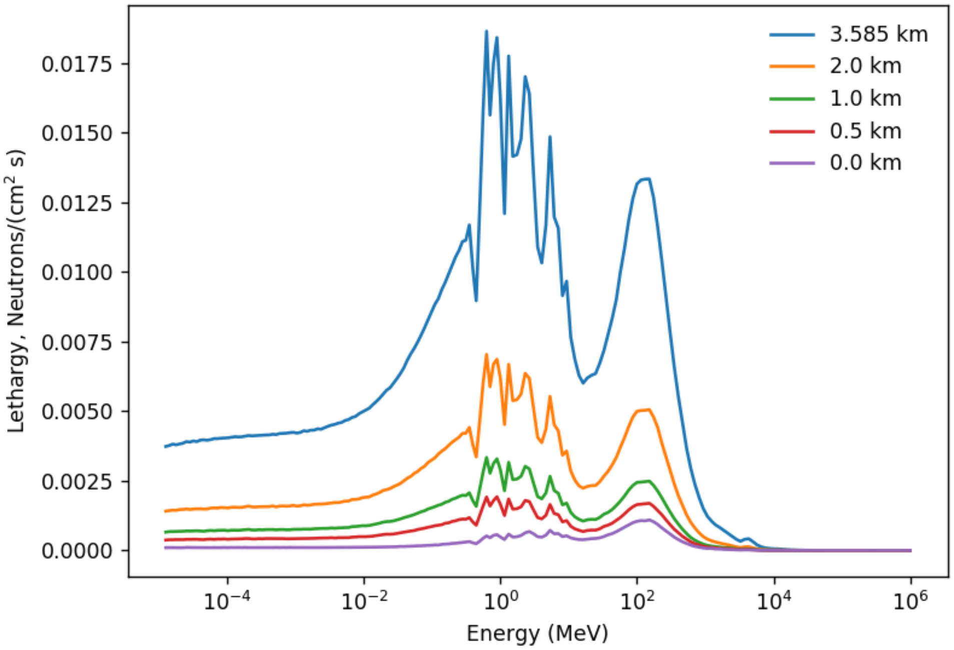

Figure 5.5: Unnormalized AIREC neutron lethargy spectra from 3.585 km to 0 km at latitude 46.55° N, longitude 7.98° E, and date September of 2018.

A neutron spectral experiment using a Bonner sphere spectrometer was conducted at the summit of the mountain Zugspitze, located along the southern border of Germany. The summit is located at the coordinates 47.4° N, 11° E, and 2.963 km [Schraube et al., 1997]. The measured neutron spectrum, the results of a simulation of the experiment conducted using the Monte Carlo code FLUKA, and the corresponding AIREC results are displayed in Figure 5.6. All three spectra have an evaporation neutron peak around 1 MeV, and an intranuclear cascade peak above 100 MeV, as was seen in the AIREC [Mares et al., 2020] comparison. Here, the experimental evaporation peak has a lower lethargy than does the intranuclear cascade peak. The experimental curve is smooth across all energies. In contrast, the AIREC results have a higher evaporation neutron peak and a lower intranuclear cascade peak. The FLUKA curve likewise has a higher evaporation neutron peak near 1 MeV and a smaller intranuclear cascade peak at an energy just above 100 MeV. The FLUKA curve has more variation throughout. The AIREC curve is in closer agreement with the

FLUKA curve than it is the experimental results, although the AIREC curve is smoother than the FLUKA curve, excepting the plateaued region from 1-10 MeV.

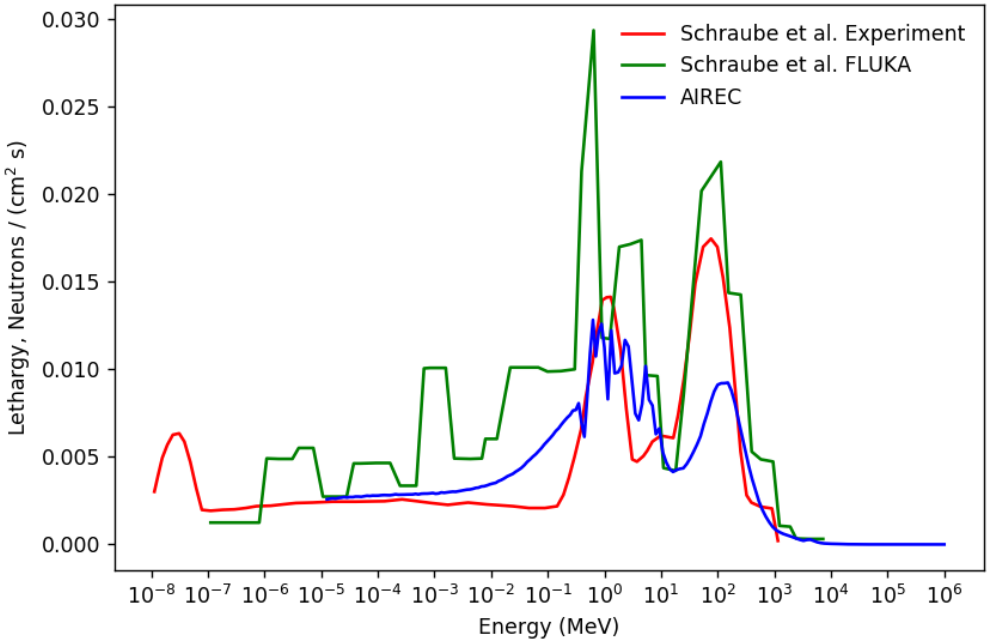

Figure 5.6: Experimental data, FLUKA simulated data, and AIREC calculated data for the neutron spectrum at the summit of the mountain Zugspitze (47.42° N, 10.9854° E, 2.963 km) in 1997 [Schraube et al., 1997].

The discrepancies between the AIREC results and those of the [Schraube et al., 1997] experiment are similar to those present between the AIREC results and the [Mares et al., 2020] experiment. The response functions for the [Schraube et al., 1997] BSS were determined using HADRON code. Although this differs from MCNPX, which was used to develop AIREC, [Schraube et al., 1997] compared the HADRON results to MCNP results and found them to be in agreement. Two different unfolding codes were used on the [Schraube et al., 1997] data, the SAND II code and the BON95 code. Considerable changes in air pressure were detected throughout the experiment, which affected the count rate, although post experiment corrections to the data to account for this variation were made. As with the [Mares et al., 2020] experiment, the AIREC neutron spectrum shape more closely resembles the shape of the [Schraube et al., 1997] neutron spectrum nearer to the ground. Interestingly, the FLUKA simulation of the Schraube experiment likewise has a higher peak at 1 MeV and a lower peak near 100 MeV.

A neutron spectral study was conducted during the AIR ER-2 flights that took place in June 1997 at a latitude of 54° N, longitude of 117° W, and an altitude of 20 kilometers. The detection system used was a multisphere, i.e. Bonner sphere, neutron spectrometer [Goldhagen et al., 2004]. The results of the experiment are displayed in Figure 5.7, along with the results from AIREC using the dates and coordinates of the experiment as inputs. Note that both the [Goldhagen et al., 2004] experiment and the AIREC have an evaporation neutron peak around 1 MeV, and an intranuclear cascade peak above 100 MeV, as was seen in the AIREC [Mares et al., 2020] comparison. Both curves contain several local peaks in the peaked region from 1-10 MeV.

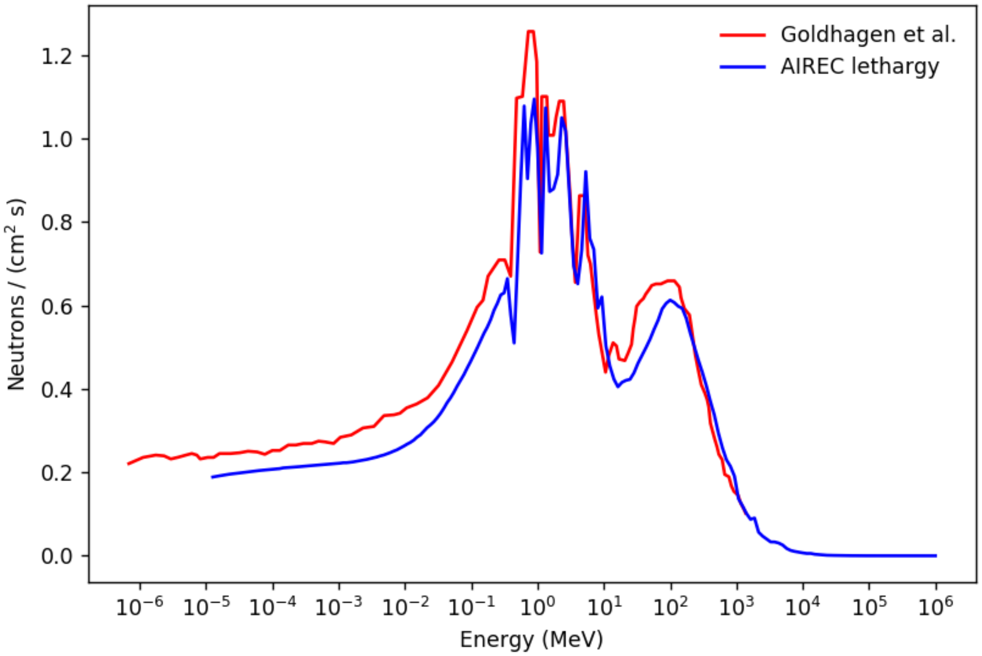

Figure 5.7: Experimental data and AIREC calculated data for the neutron lethargy spectrum at the coordinates 54° N, 117° W, and 20 km in June of 1997 [Goldhagen et al., 2004].

The extraordinary agreement between the AIREC calculated code and the [Goldhagen et al., 2004] experiment is in part due to common assumptions held by both approaches. The BSS response functions used by [Goldhagen et al., 2004] were calculated in MCNPX, the same version of MCNP used in developing AIREC. [Goldhagen et al., 2004] made stronger assumptions about the shape of the neutron spectrum than did either [Mares et al., 2020] or [Schraube et al., 1997]. The result of a FLUKA simulation were used as the initial guess for unfolding the data of the [Goldhagen et al., 2004] data [Clem et al., 2004]. This FLUKA neutron spectrum had finer features present in its peaks than the smoother peaks seen in the [Mares et al., 2020] and [Schraube et al., 1997] data, and this led to such features being present in the [Goldhagen et al., 2004] data. The [Goldhagen et al., 2004] data was taken aboard a flight at 20 km, removing backscatter present in ground based measurements. This is also approximately the altitude of the Pfotzer maximum, and the higher count rate in this region provides better statistics for the AIREC spectral results.

5.2. Model Simulations

One such data set resulted from simulations using the Monte Carlo radiation transport code CORSIKA. The secondary electron spectrum was calculated at various altitudes above Stillwater, OK (36.1° N, 97° W) [Lindy et al., 2018] and are displayed in Figure 5.8 along with the comparable spectra as calculated in AIREC. The curves are largely in agreement in terms of overall shape. However, the CORSIKA calculated spectra are generally of higher flux than the comparable AIREC spectra.

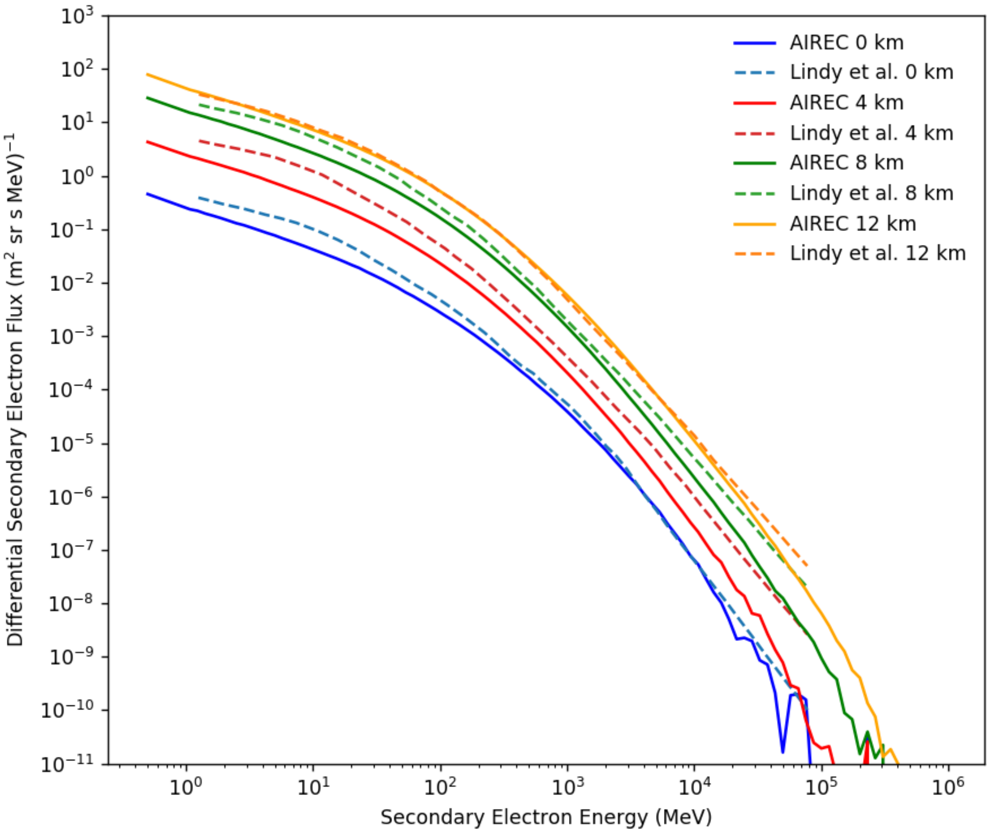

Figure 5.8: The secondary electron flux above Stillwater, OK (36.1° N, 97° W) at several altitudes as calculated using CORSIKA and AIREC [Lindy et al. 2018].

The percent difference between each AIREC and CORSIKA spectrum is displayed in Figure 5.9. There is no obvious trend in the percent difference versus the secondary electron energy. There are several potential reasons for discrepancies between the CORSIKA and AIREC data. AIREC was developed using the results of MCNPX simulations, and data from these simulations was interpolated to determined novel results. [Lindy et al. 2018] considered only a few discrete locations, and a novel CORSIKA simulation was used for each. CORSIKA was developed specifically to model extensive air showers (EAS) in the Earth's atmosphere, while MCNPX has broader applications. These CORSIKA simulations only used GCR primary protons and no higher Z elements. The maximum GCR energy simulated in the AIREC MCNPX simulations was 1 TeV, while the CORSIKA simulations included GCR protons with energies up to 10 PeV [Lindy et al. 2018]. CORSIKA was developed with these higher energy particles in mind, while MCNP is generally not considered to be reliable in transporting particles with energy beyond 1 TeV [Mashnik et al., 2017]. This in part explains the consistently higher CORSIKA secondary electron fluxes.

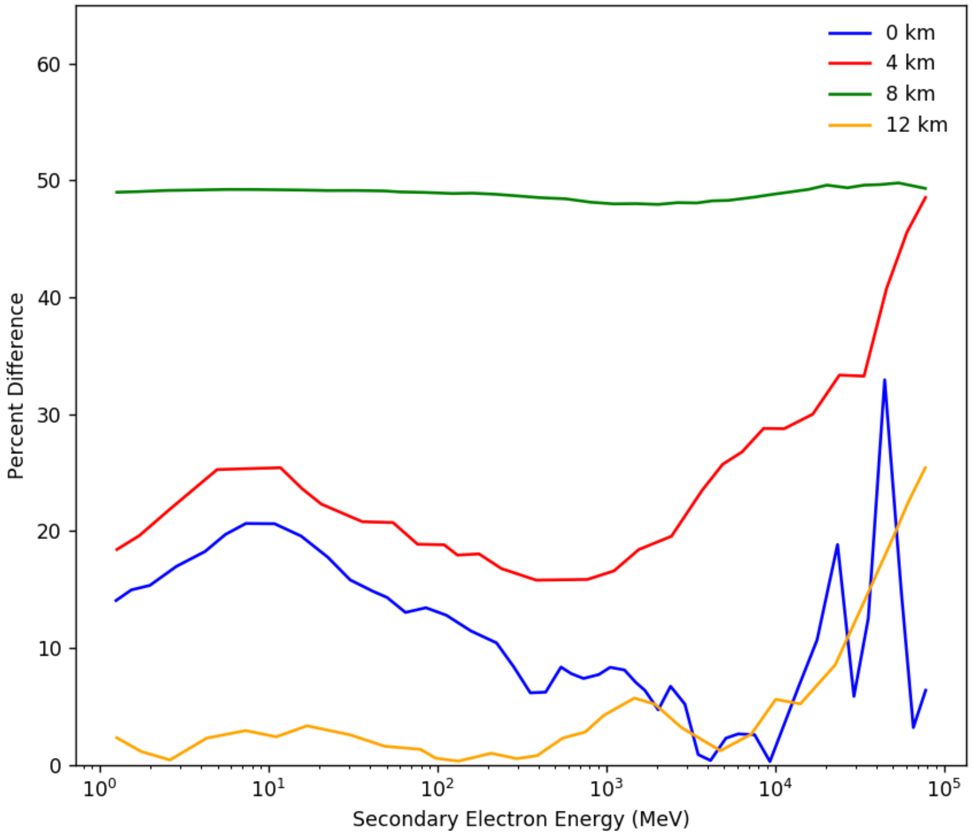

Figure 5.9: The percent difference between electron spectra at several altitudes above Stillwater, OK as calculated using CORSIKA and AIREC [Lindy et al. 2018].

Another set of comparison data available for a limited number of parameters is the secondary particle flux versus altitude calculated by [Ferrari et al., 2001]. FLUKA simulations were conducted to determine the flux versus altitude for protons (Figures 5.10 and 5.11), electrons (Figures 5.12 and 5.13), photons (Figures 5.14 and 5.15), muons (Figures 5.16 and 5.17), pions (Figures 5.18 and 5.19), and neutrons (Figures 5.20 and 5.21). The flux versus altitude was determined for geomagnetic rigidity of 0.4 GV during solar minimum and solar maximum and for geomagnetic rigidity of 17.6 GV during solar minimum [Ferrari et al., 2001]. Each figure also displays a corresponding AIREC produced spectrum.

The AIREC and [Ferrari et al., 2001] spectra are largely in agreement in terms of general shape of the flux versus altitude curves. Given differences in GCR models used, Monte Carlo transport codes used, the cross section libraries for each Monte Carlo transport code, and the statistical fluctuation inherent in the Monte Carlo method, the amount of disagreement between the models is to be expected. The [Ferrari et al., 2001] fluxes are consistently higher than the corresponding AIREC data during solar minimum for both geomagnetic cutoffs and consistently lower than the corresponding AIREC data during solar maximum. The [Ferrari et al., 2001] shows much greater variation due to changes between solar minimum and maximum than does the AIREC data. [Ferrari et al., 2001] used neutron ground monitors to calculate solar cycle, while AIREC used the ISO model, which uses sunspot numbers. The [Ferrari et al., 2001] fluxes contain more outlier data points than do the AIREC fluxes. Particularly, the pion flux data from the FLUKA simulations displays large amounts of variation. Such variation, particularly in the lower flux pions, is generally indicative of an insufficient number of starting particles in the Monte Carlo radiation transport simulations, leading to poor counting statistics. Given the publication date of the [Ferrari et al., 2001] data, time and hardware constraints may have limited the number of starting particles that were run. As there is no experimental data with which to compare these two models, there is no way to know which is closer to reality, although there is no reason to expect the variation seen in the FLUKA generated pion flux or the outlier data in the electron and muon fluxes.

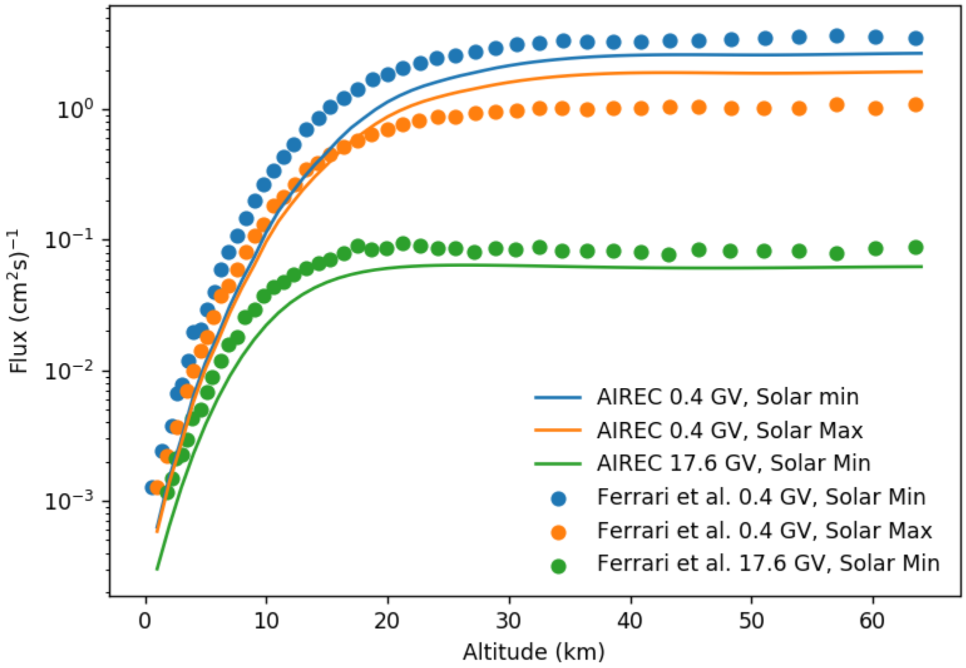

Figure 5.10: Comparison of AIREC and [Ferrari et al., 2001] proton flux versus altitude.

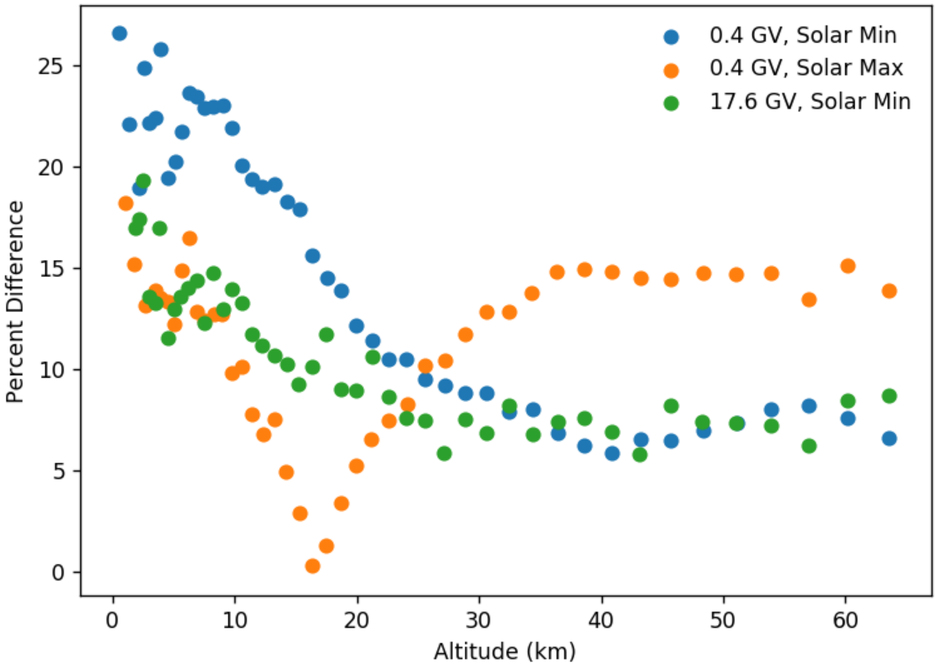

Figure 5.11: Percent difference between AIREC and [Ferrari et al., 2001] proton fluxes.

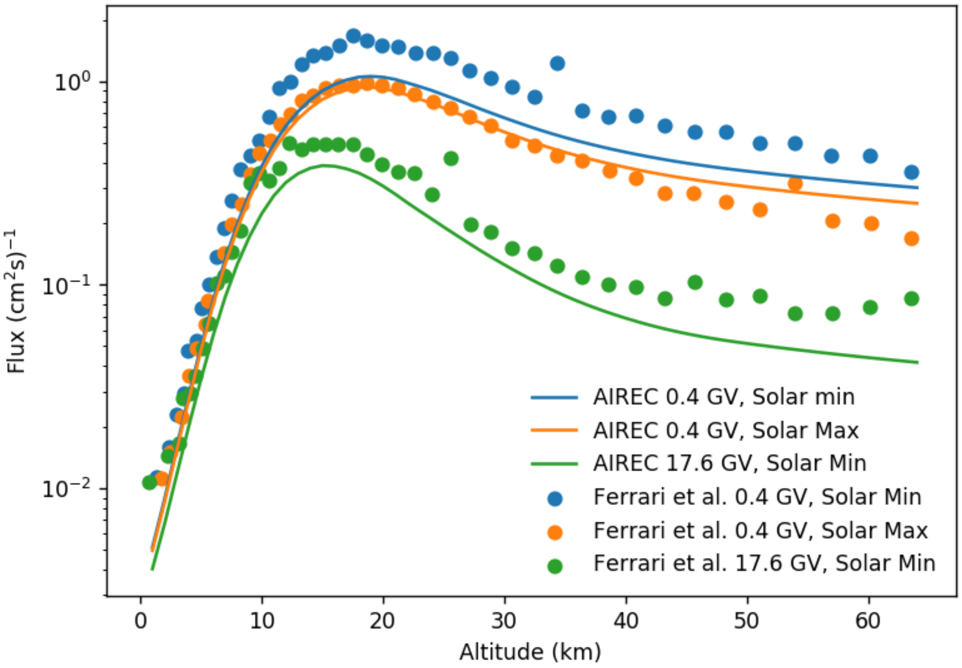

Figure 5.12: Comparison of AIREC and [Ferrari et al., 2001] electron flux versus altitude.

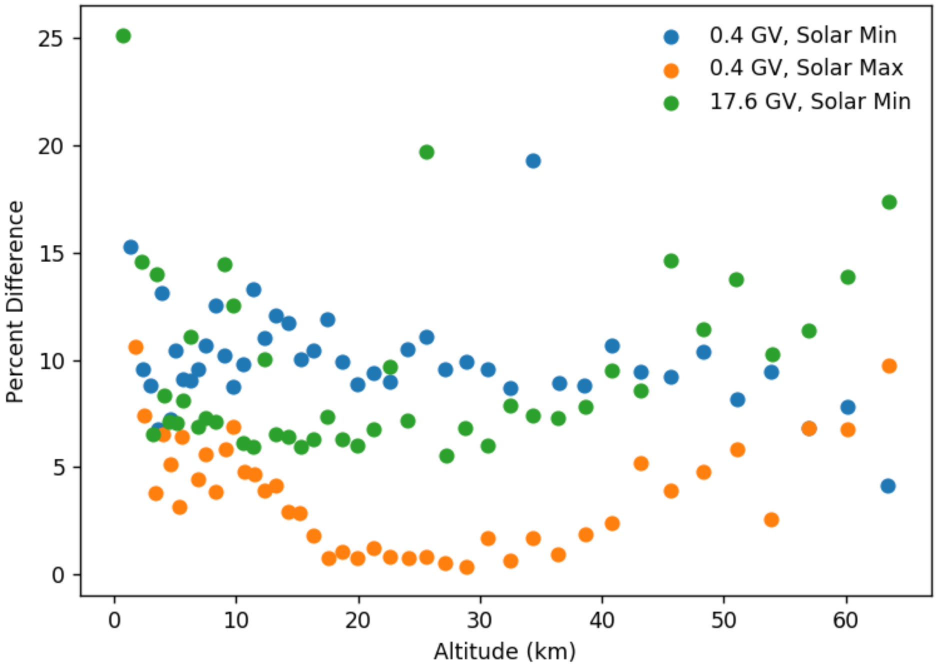

Figure 5.13: Percent difference between AIREC and [Ferrari et al., 2001] electron fluxes.

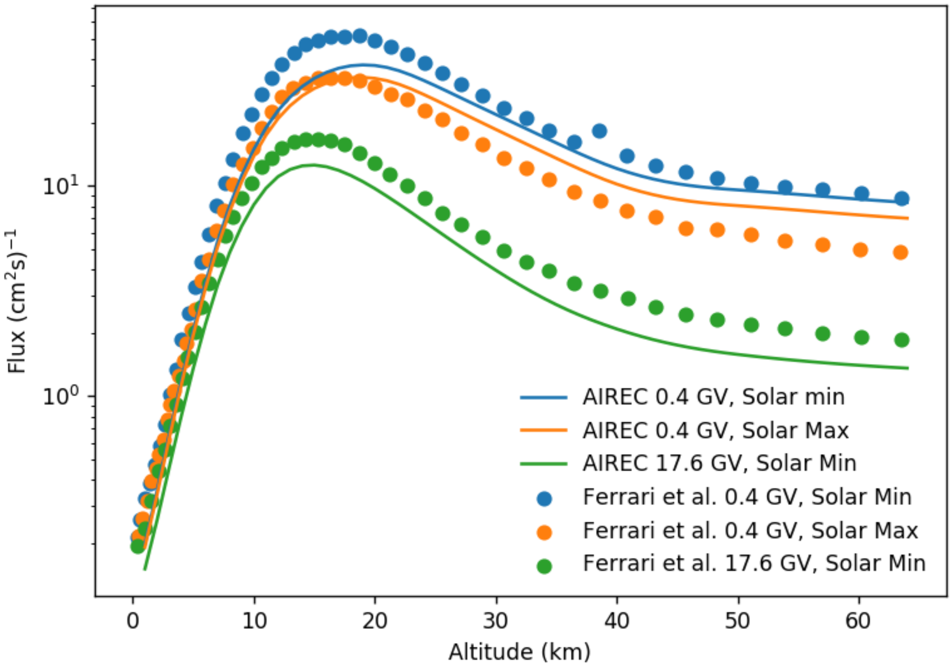

Figure 5.14: Comparison of AIREC and [Ferrari et al., 2001] photon flux versus altitude.

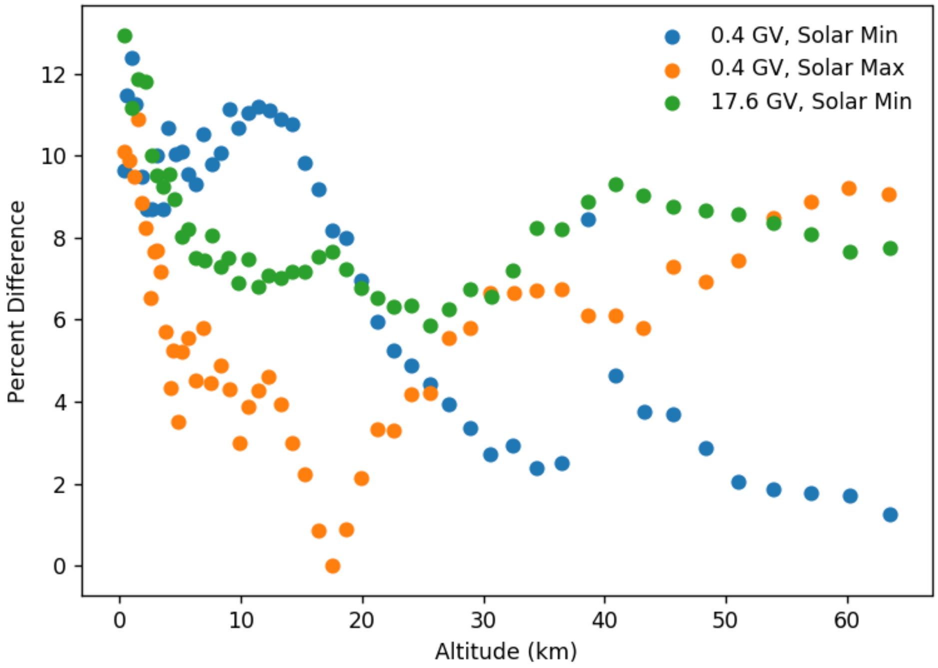

Figure 5.15: Percent difference between AIREC and [Ferrari et al., 2001] photon fluxes.

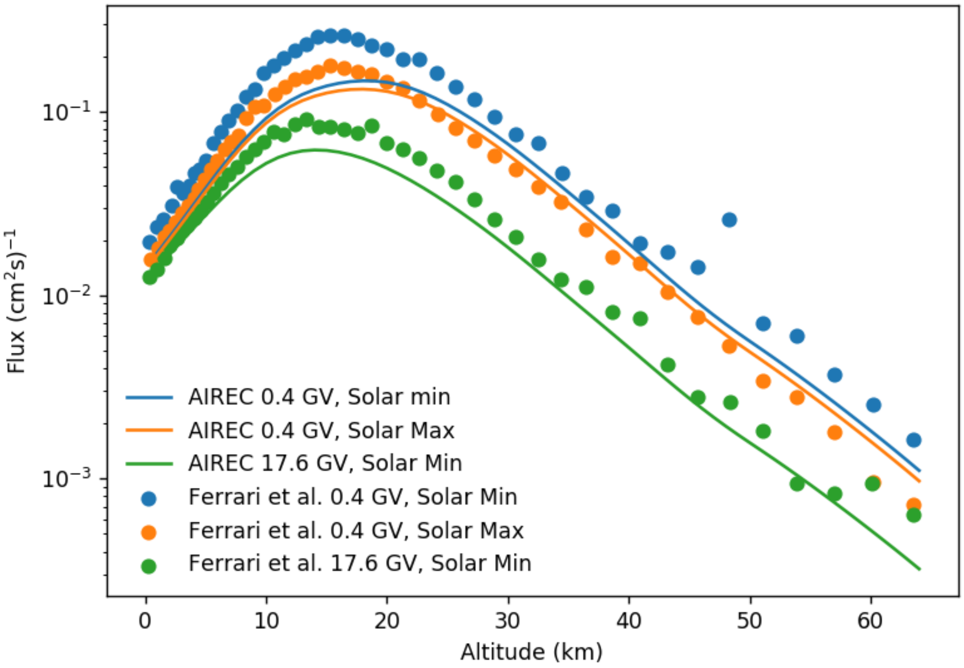

Figure 5.16: Comparison of AIREC and [Ferrari et al., 2001] muon flux versus altitude.

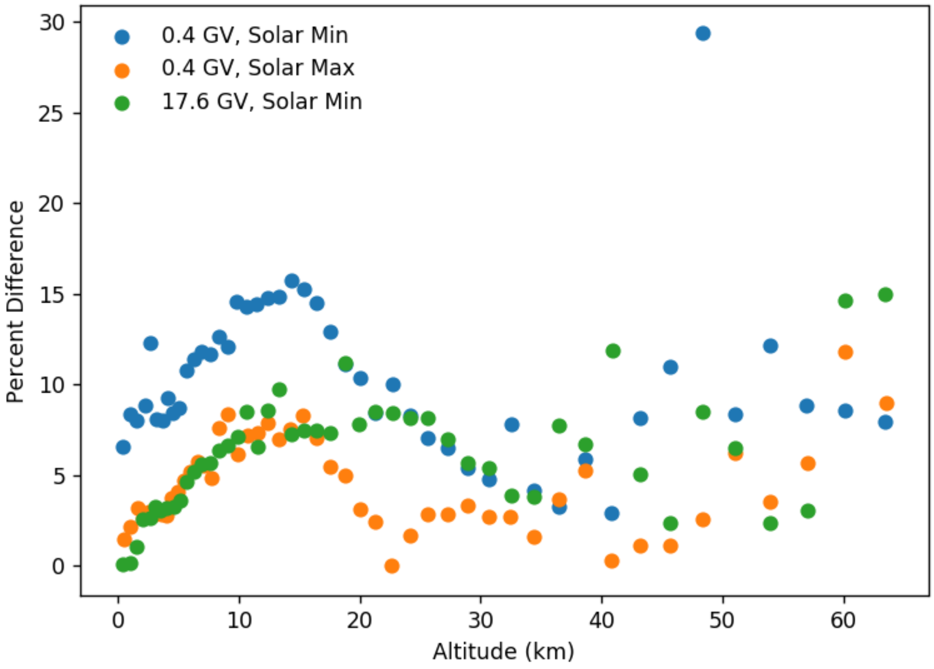

Figure 5.17: Percent difference between AIREC and [Ferrari et al., 2001] muon fluxes.

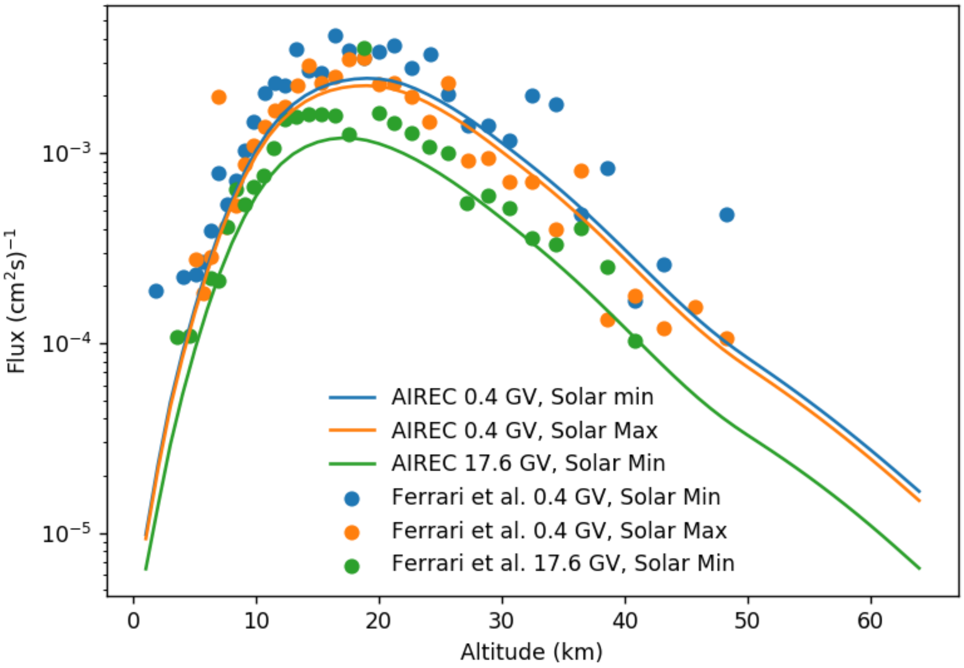

Figure 5.18: Comparison of AIREC and [Ferrari et al., 2001] pion flux versus altitude.

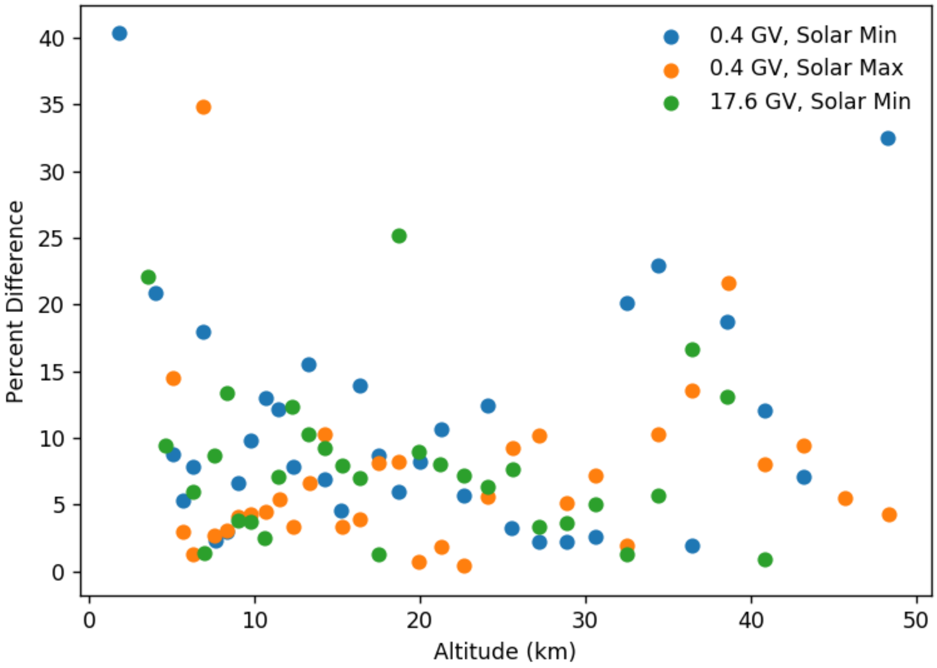

Figure 5.19: Percent difference between AIREC and [Ferrari et al., 2001] pion fluxes.

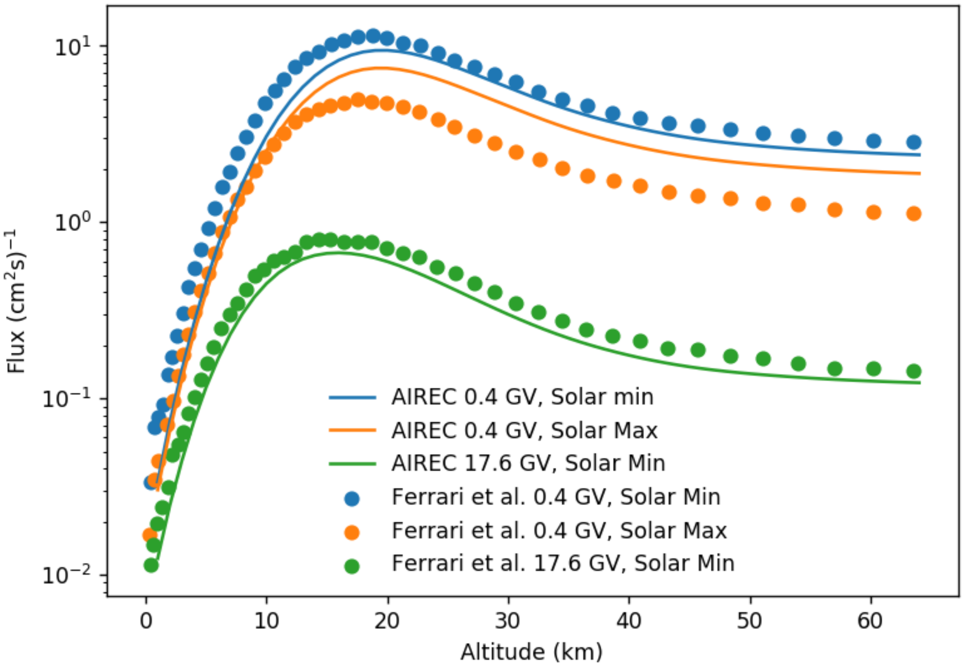

Figure: 5.20: Comparison of AIREC and [Ferrari et al., 2001] neutron flux versus altitude.

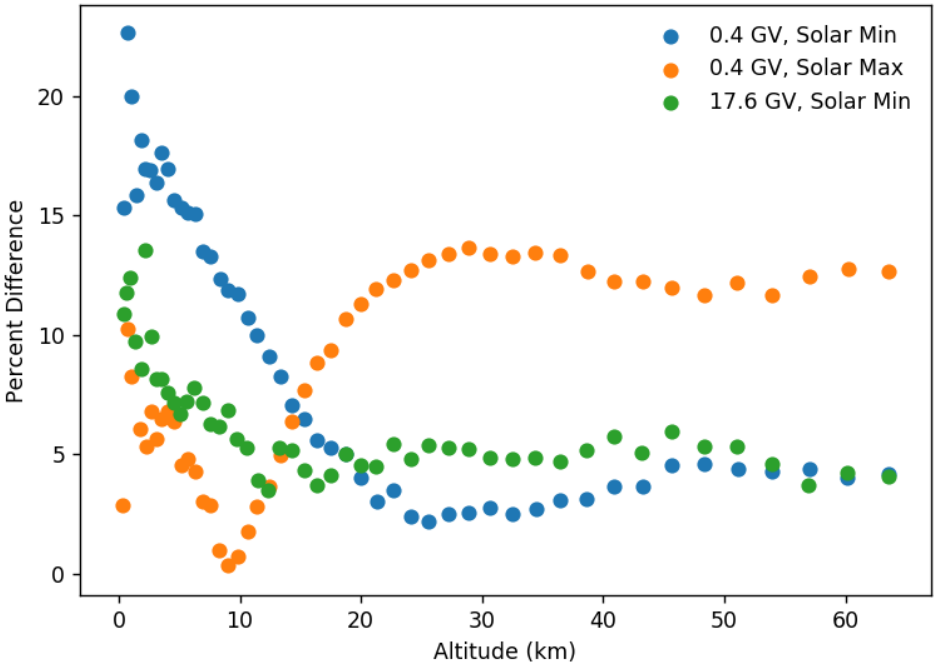

Figure: 5.21: Percent difference between AIREC and [Ferrari et al., 2001] neutron fluxes.

5.3. Conclusions

For the experiments and simulations shown in this chapter, AIREC was seen to largely be in agreement. However, there were significant areas of disagreement, particularly at altitudes below 10 km, as shown by comparisons to the data from [Lindy et al. 2018], [Schraube et al., 1997], and [Mares et al., 2020]. Disagreement was also found when neutron ground monitor data was used to calculate the solar effects on GCR rather than a sunspot model as AIREC uses. These disagreements were demonstrated by the comparisons to the data from [Ferrari et al., 2001] and [Bartol Institute]. The secondary fluxes calculated using neutron monitor solar cycle models demonstrated a stronger dependence on the variation in the solar cycle. This also presents an opportunity for future work to include an option in AIREC to use a neutron monitor based solar cycle model. In neutron measurements, assumptions about cross sections, response functions, and unfolding algorithms can cause significant variation in results, and there is no agreed upon unique neutron spectrum that results from BSS measurements. The lack of additional data available for comparison demonstrates the impetus for developing AIREC. The lack of data also makes thorough verification of AIREC impossible, as the vast majority of possible AIREC results have no comparable data available.

CHAPTER VI

APPLICATIONS OF AIREC TO RADIATION DOSIMETRY EXPERIMENTS

This chapter includes examples of how an output secondary flux spectrum produced by AIREC can be used to lend insight into the physical mechanisms of radiation interactions taking place in an experimental setting. In particular, AIREC generated spectra can be used as source particle inputs in MCNP simulations. These AIREC spectra and simulations yield insight into experimental results that would not have otherwise been possible. Simulations of experiments that took place at the Los Alamos Neutron Science Center (LANSCE) and aboard the Deep Space Test Bed (DSTB) flight are discussed in the following sections.

6.1. The ATED Experiment at LANSCE

Experiments were conducted at the Los Alamos Neutron Science Center (LANSCE) to test the response of an active tissue equivalent dosimeter (ATED). Tissue equivalent detectors like ATED have been used for aircraft and spacecraft dosimetry for many years. The sensitive region of ATED is comparable to a human cell, so experiments using ATED lend insight into how radiation deposition in small volumes of tissue [Hayes, 2020]. The LANSCE ATED experiments were conducted to better understand the ATED response, which in turn improves understanding of radiation dosimetry. One application of ATED is as a dosimeter for personnel aboard an aircraft. Because the LANSCE facility has a neutron beam with a spectrum that resembles the spectrum atmospheric neutrons but orders of magnitude more intense, it was used as a proxy to test the ATED response to atmospheric neutrons.

6.1.1. LANSCE Facility and Neutron Energy Spectrum

The LANSCE facility produces spallation neutrons from an 800 MeV pulsed proton beam incident on a tungsten target. The proton-tungsten collisions also result in other species of particles each with a spectrum of energies. The product particles are passed through sweep magnets, which filters out the charged particles, leaving only uncharged gammas and neutrons [Gersey et al., 2003; Gersey et al., 2007]. Of these neutral particles, the neutrons dominate in terms of contribution to the ATED signal. Several buildings at the LANSCE facility can be used to conduct experiments along different neutron flight paths, and the neutron spectra differ along different flight paths. The ICE House Flight Path 30L flight path consists of neutrons with an energy spectrum that is similar in shape to that of the energy spectrum of atmospheric neutrons but five to six orders of magnitude greater than the secondary neutron flux at an altitude of 12 kilometers [Gersey, 2003; Gersey, 2007; Nowicki et al., 2017]. Figure 6.1 shows a diagram of the production of neutrons at the LANSCE ICE House. The neutrons along the ICE House Flight Path 30L were measured during past experiments at LANSCE via fission chamber time of flight (TOF) measurements in a range from 1 to 800 MeV. The results of such a TOF spectral measurement were provided by LANSCE scientists for this work and are shown in figure 6.2

[LANL, 2018]. The 1 MeV lower energy range of neutrons represents a limitation of the experiment. Neutrons with sub MeV neutrons are actually present in the beam.

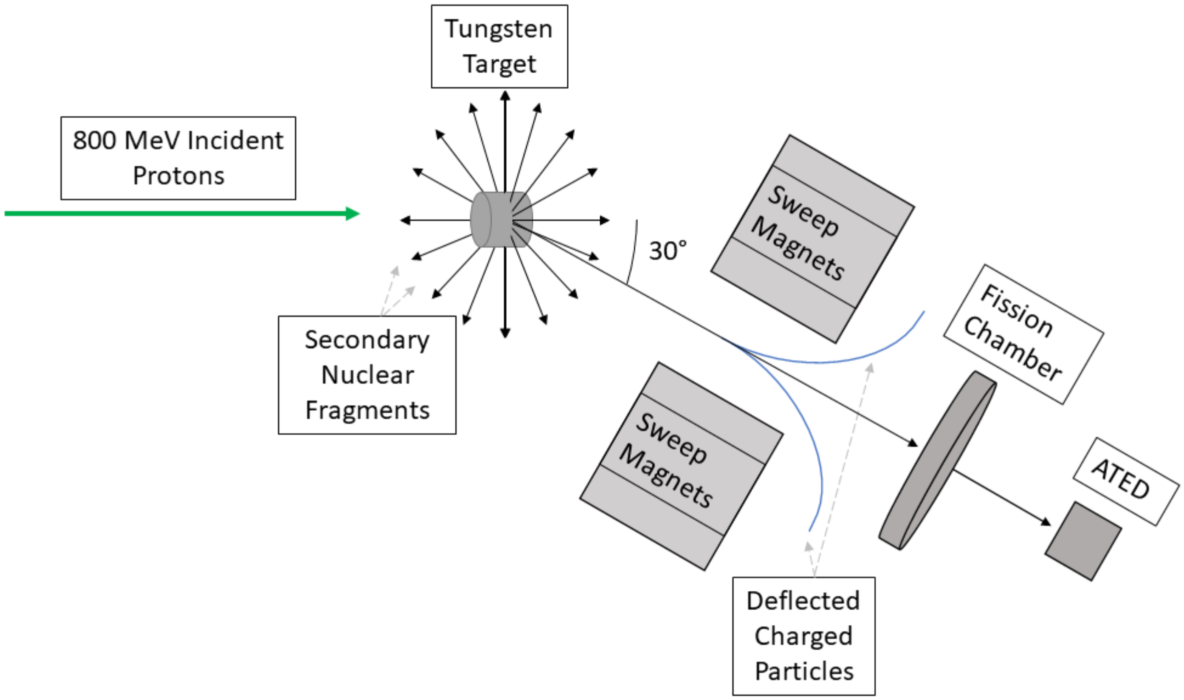

Figure 6.1: This diagram details the production of neutrons along the ICE House Flight Path 30L beamline at LANSCE [Hayes, 2020].

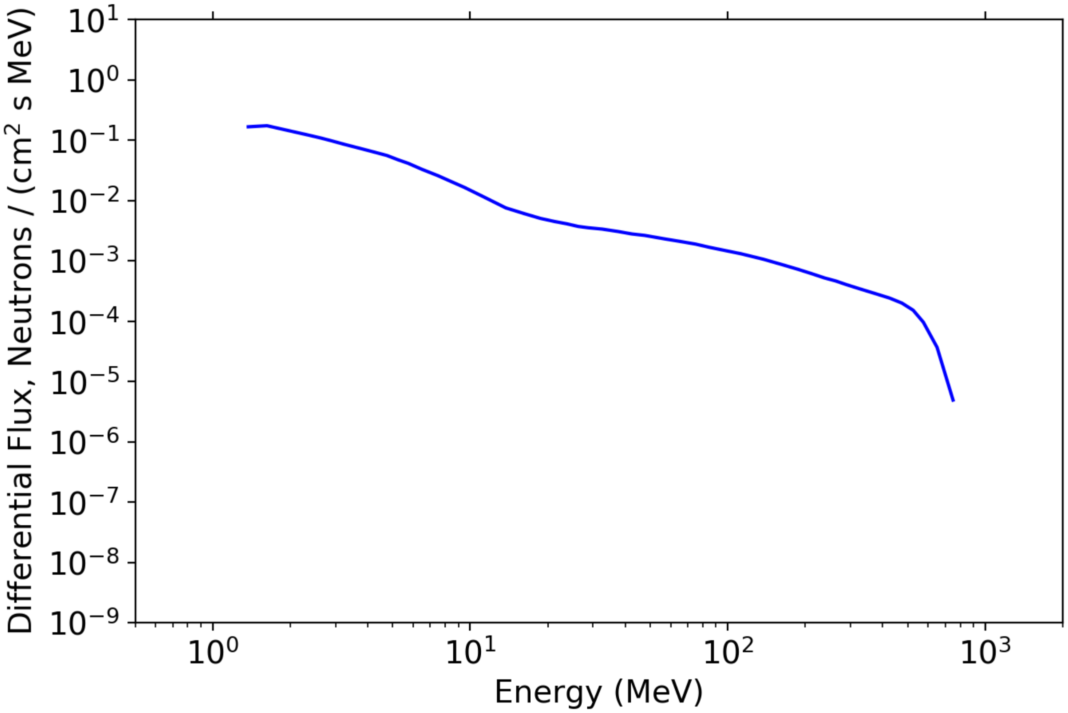

Figure 6.2: The figure displays the ICE House Flight Path 30L beamline neutron spectrum as measured from TOF measurements at the LANSCE facility [LANL, 2018].

6.1.2. Description of the ATED and the ATED Experiment Performed at LANSCE.

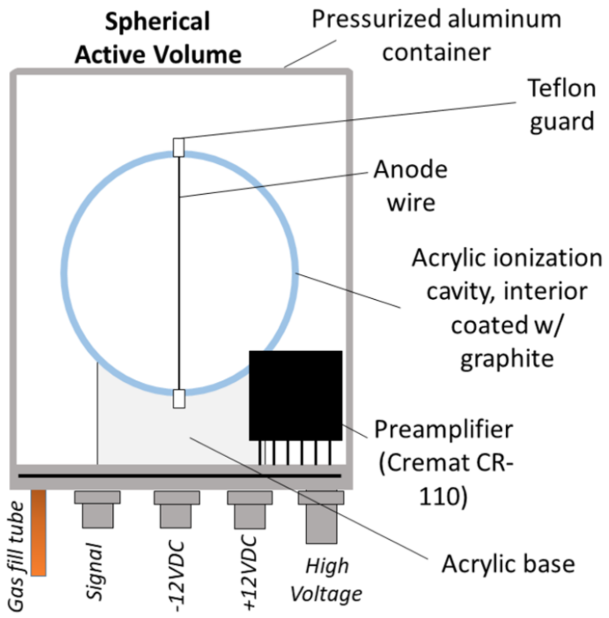

Figure 6.3: A schematic of the ATED detector [Hayes, 2020].

ATED was placed in the ICE House Flight Path 30L neutron beam as shown in Figure 6.1. A measured lineal energy spectrum is displayed in Figure 6.4 [Hayes, 2020]. Lineal energy is the energy deposited in the medium divided by the mean chord length of the interior of the sphere. Lineal energy has units keV/μm and is given by the equation,

$$y = \frac{\epsilon}{\bar{l}} . \tag{6.1}$$

Here, y is the lineal energy, ϵ is the energy deposited in the volume of interest, and $\bar{l}$ is the mean chord length of the volume of interest [Rossi, 1996; Booz, 1983]. The sensitive volume of ATED is a sphere, hence the mean chord length is given by

$$\bar{l} = \frac{2}{3} d \ . \tag{6.2}$$

Here, *d* is the diameter of the sphere. The lineal energy spectrum y-axis is in terms of the product *yd(y)*, where *d(y)* is the dose probability density. The area under the *yd(y)* curve, i.e. the integral of *yd(y)*, is directly proportional to absorbed dose [Booz, 1983; Hayes, 2020]. The right edge of the spectrum is known as the proton edge and corresponds to the maximum lineal energy that a proton can deposit in the active volume of the ATED [Hayes, 2020].

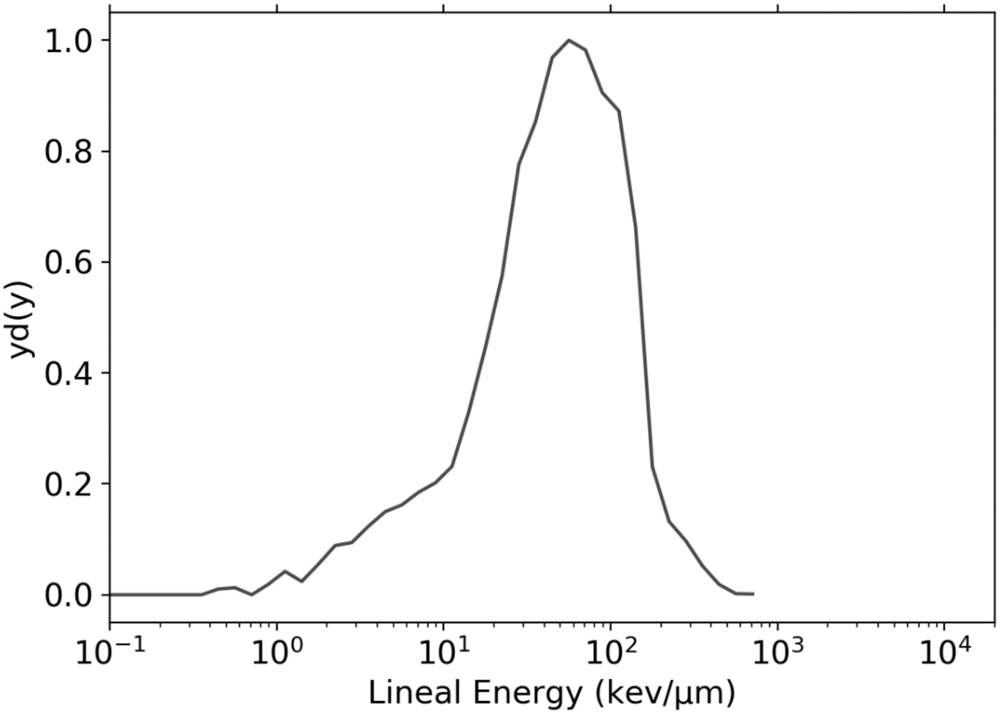

Figure 6.4: The lineal energy spectrum as measured by ATED from exposure to the LANSCE ICE House Flight Path 30L neutron beam [Hayes, 2020].

Additional exposures of the ATED were made with shielding materials placed between the ATED and the incident neutron beam. These shielding materials included 5.34 g/cm^2 of aluminum, 5.38 g/cm^2 of high density polyethylene (HDPE), and a simulated air craft wall, which consisted of 5.3 g/cm^2 of aluminum plus 3.2 g/cm^2 of HDPE [Hayes, 2020]. The absorbed doses resulting from each shielding configuration normalized to that of the nominal (unshielded) beam are displayed in Table 6.1.

Material	**Absorbed Dose Relative to Nominal Beam**
Nominal Beam	1
5.34 g/cm^2 Al	0.772 ± 0.049
5.38 g/cm^2 HDPE	0.470 ± 0.030
5.3 g/cm^2 Al + 3.2 g/cm^2 HDPE	0.636 ± 0.041

Table 6.1: The relative absorbed doses resulting from exposing the ATED to the LANSCE ICE House 30L neutron beam given different shielding configurations.

6.1.3. Simulating the Experiment in MCNP

The ATED LANSCE experiment was simulated using MCNP 6.2. A schematic of the simplified ATED geometry used in MCNP simulations is displayed in Figure 6.5. The aluminum of the outer ATED cylindrical had density of 2.7 g/cm^3. The inner acrylic sphere had density of 1.19 g/cm^3. The tissue equivalent gas inside the sphere and between the sphere and the aluminum cylinder had mass composition of 0.101 hydrogen, 0.472 carbon, 0.388 oxygen, and 0.0312 nitrogen and density 3.44×10^{-5} g/cm^3. Incident neutrons originated 10 cm from the center of the sphere and were generated on a disc source of area equal to the cross sectional area of the acrylic sphere. Dry air filled the space between the source neutrons and ATED [Hayes, 2020]. The time of flight measured neutron spectrum of Figure 6.2 was used for the MCNP source particle distribution function.

The MCNP simulation was used to determine a spectrum of counts versus energy deposited, i.e. a calibrated pulse height distribution, which experimentally was produced by a multichannel analyzer. More details on using MCNP to simulate detector response can be found in the literature [Ali, 2014; Ali et al., 2014; Taylor et al., 2015; Booz et al., 1983; Werner, 2017; Wilcox, 2014; X-5 Monte Carlo Team, 2003].

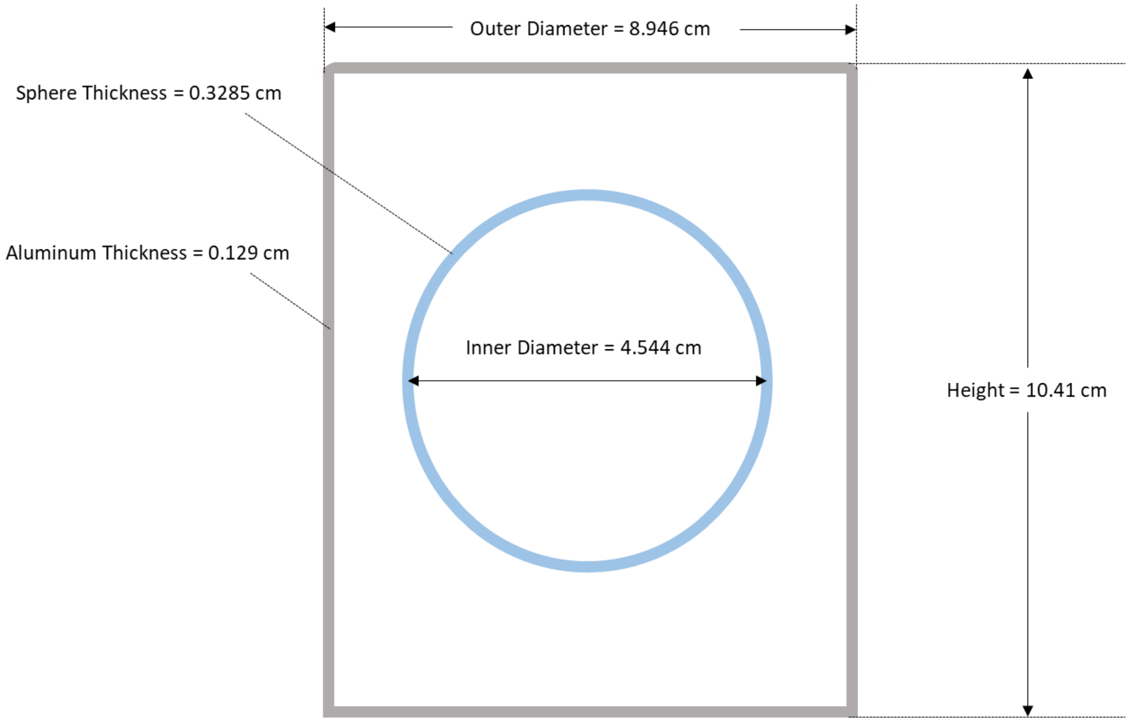

Figure 6.5: The simplified geometry of the ATED used in MCNP simulations of the ATED LANSCE experiment.

6.1.4. Preliminary Comparison of Experimental and Simulated Results

When simulated in MCNP the LANSCE incident neutron spectrum resulted in the ATED signal labeled LANSCE in Figure 6.4. Also displayed is the ATED signal measured during the experiment, which is labeled ATED.

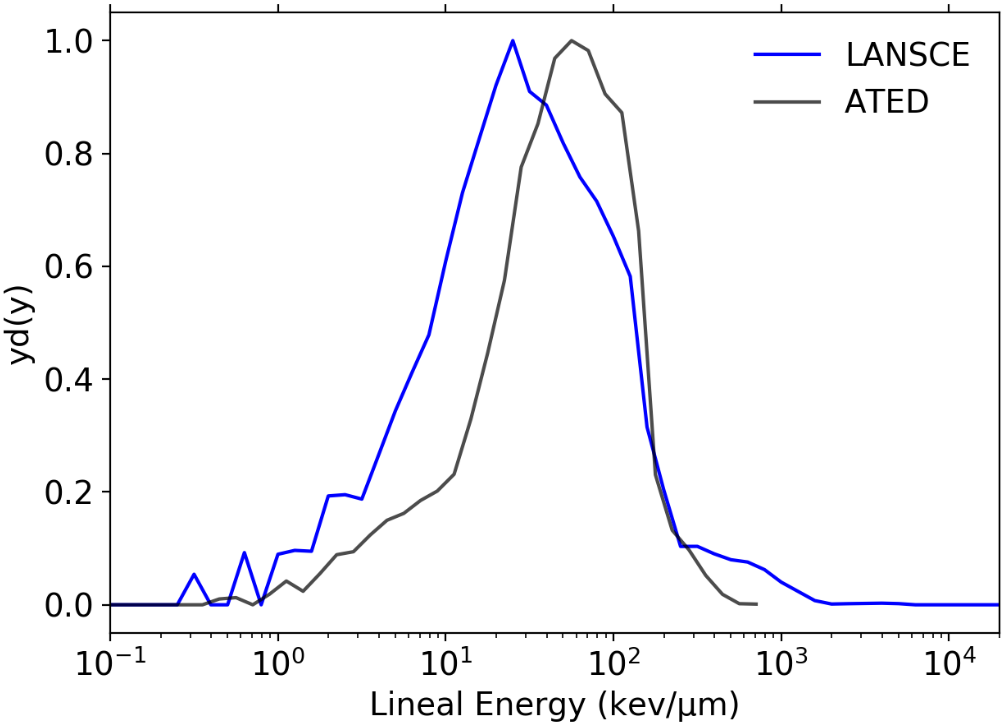

Figure 6.6: Displayed is the ATED signal calculated from MCNP simulations using the LANSCE time of flight measured neutron spectrum as an input (LANSCE) compared to the experimental data (ATED).

Although the shapes of the experimental and measured lineal energy spectra are similar, the simulated spectrum is shifted to considerably lower lineal energy. The right edge of the peak of the spectrum represents the maximum lineal energy that a proton can deposit in the sensitive region of the detector and is referred to as the proton edge. Ideally, the proton edge calculated from the simulation would more closely align with the measured proton edge.

6.1.5. MCNP Additional Incident Neutron Spectra

Because the LANSCE provided neutron spectrum did not include sub MeV neutrons, additional incident neutron spectra that included lower energy neutrons were used as input spectra for

MCNP simulations. These additional neutron spectra included a spectrum that resulted from MCNP simulations of the LANSCE facility [Sutton et al., 2000]. Because the ICE HOUSE flight path 30L neutron spectrum is approximately the same shape as that of atmospheric secondary neutrons, one of the spectra used was a measurement of atmospheric neutrons using Bonner sphere neutron spectrometers [Goldhagen et al., 2004]. Lastly, one of the input neutron spectra was calculated using AIREC. These spectra, along with the original neutron spectrum provided at the LANSCE facility are displayed in Figure 6.5.

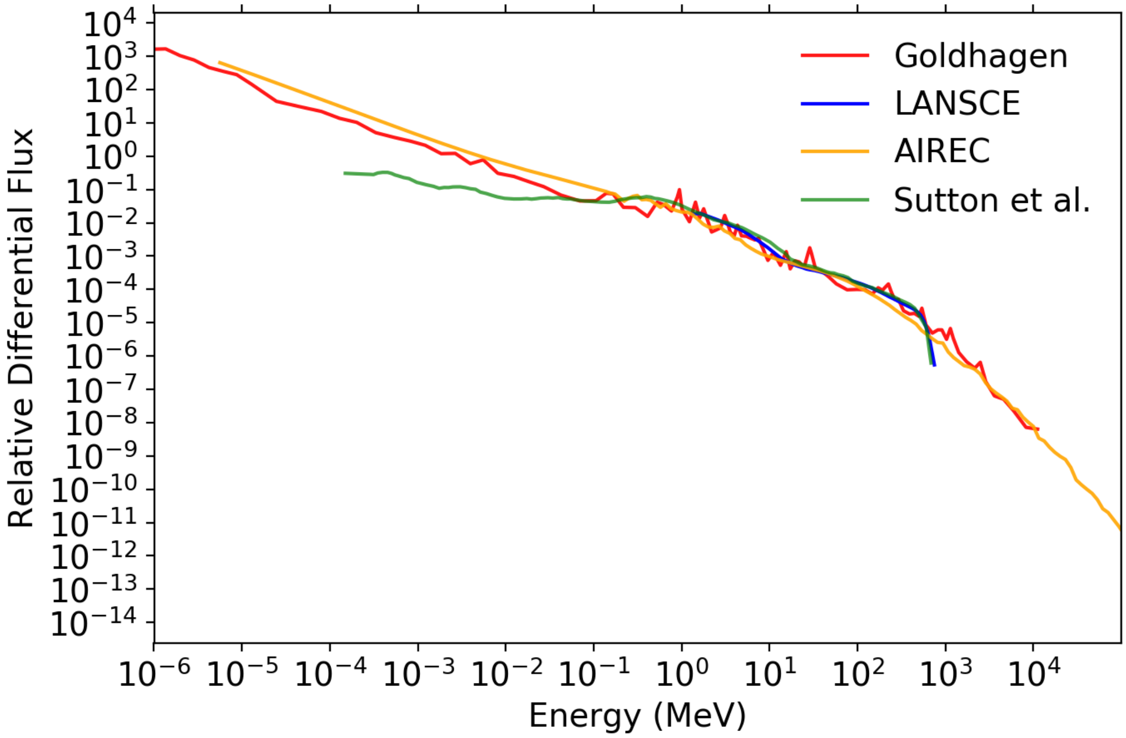

Figure 6.7: Displayed are the neutron spectrum provided at the LANSCE facility (LANSCE), measured by [Goldhagen et al., 2004], calculated by AIREC, and calculated from MCNP simulations of the LANSCE facility [Sutton et al., 2000].

6.1.6. Comparison of Experimental and Simulated Results

The ATED lineal energy spectra resulting from using the different incident neutron spectra of Figure 6.5 as inputs in MCNP simulations are displayed in Figure 6.6. Also shown is the spectrum from the ATED experiment.

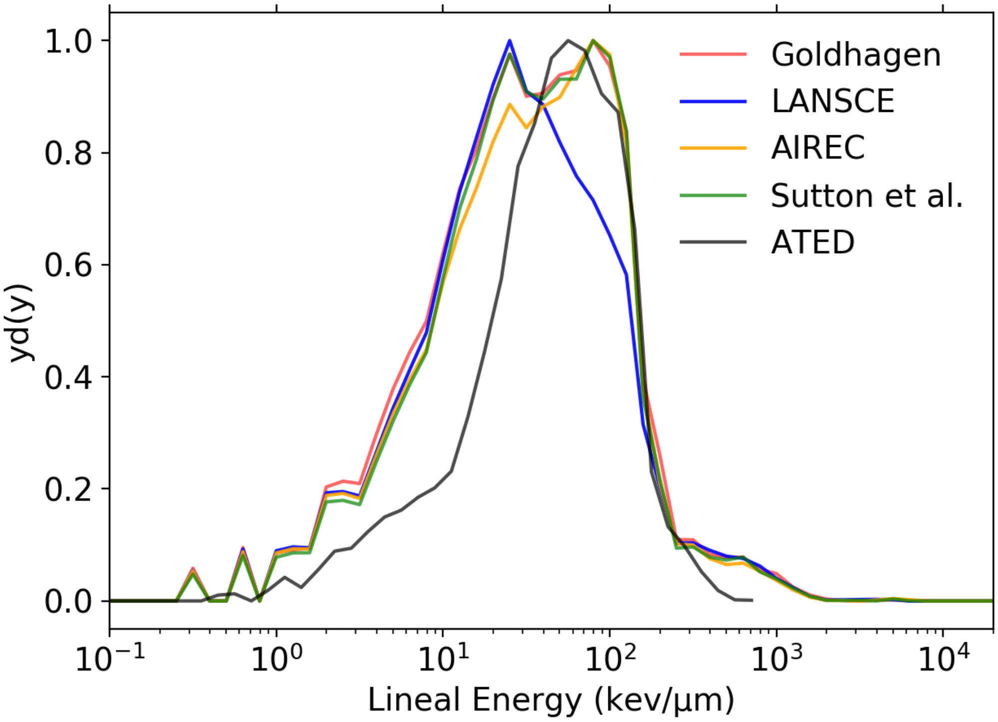

Figure 6.8: Displayed is the ATED signal resulting from experiment and from using the input neutron spectra of Figure 6.5 in MCNP simulations of ATED.

The MCNP simulations offer insights into the underlying physics that are not available from the experiment. The exclusion of the sub 1 MeV neutrons in the LANSCE spectrum shifted the lineal energy spectrum recorded by the simulated ATED to lower lineal energies. The [Goldhagen et al., 2004], AIREC, and [Sutton et al., 2000] input spectra all included sub 1 MeV neutrons in their spectra, and each of these input spectra resulted in simulated lineal energy spectra that better matched experimental results. The curves are in particularly good agreement along the proton edge, i.e. the edge to the right of the peak of the spectrum. The agreement between these particular MCNP and experimental results provides evidence of agreement between the two methods more generally, and gives confidence in the results of future simulations.

Because neutrons generated by a spallation source result in a broad energy spectrum, it is not possible to isolate specific energies of neutrons to perform dosimetry response experiments. Therefore, another insight from simulations unavailable from the experiment is the dose contribution that would result from each of the energy regions of the broad neutron spectrum. The AIREC neutron spectrum of Figure 6.7 was divided by energy decade, i.e. 10^{-5} to 10^{-4} MeV, 10^{-4} to 10^{-3} MeV, …, 10^{5} to 10^{6} MeV. Each decade was used as the source particles for a separate MCNP simulation, and the dose was tallied. Each calculated dose due to a neutron energy decade was weighted by the fraction of the total neutron spectrum the neutrons in that decade comprised. Doses were then normalized such that the total dose equaled one, resulting in the fraction of the total dose from incident neutrons of each energy decade. These results are displayed in Figure 6.7.

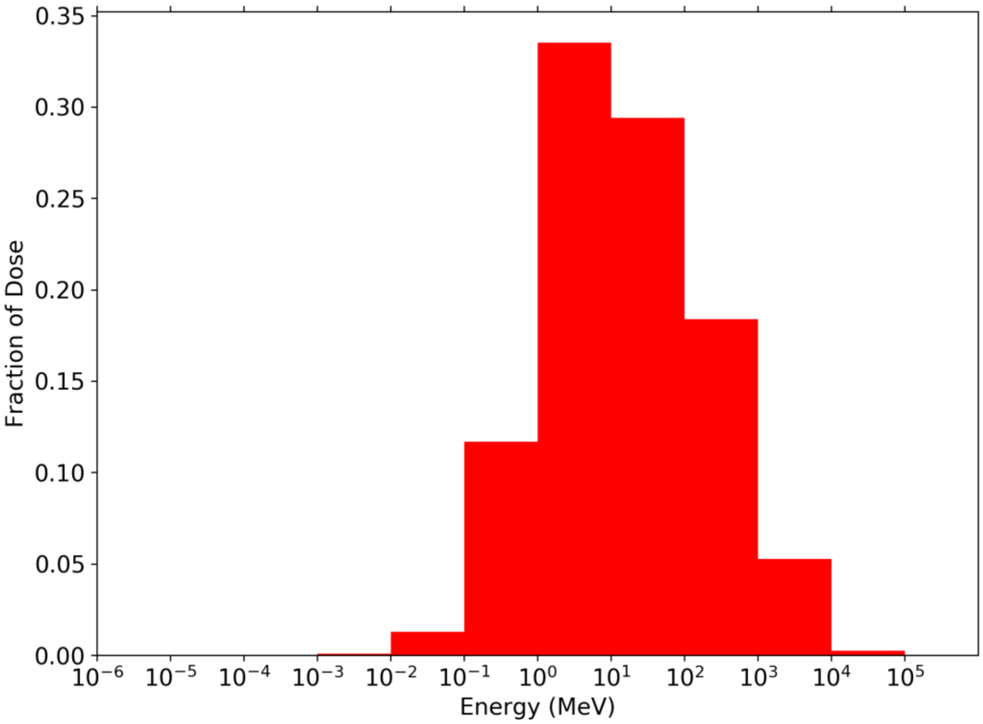

Figure 6.9: The fraction of the dose due to incident neutrons in different energy decades.

From the results shown in Figure 6.9, it was determined that only about 0.1% of the absorbed dose is due to neutrons with energy below 10^{-2} MeV, despite the fact that these neutrons account for over 25% of the incident neutrons. This indicates that the incident neutrons with energies below 10^{-2} MeV can generally be ignored in simulations pertaining to radiation dosimetry at aviation altitudes. Neutrons with energies from 10^{-2} to 1 MeV account for nearly 15% of the dose. These neutrons were excluded from the LANSCE provided neutron energy spectrum, but their contribution to dose is too high to ignore in any dosimetry experiment or simulation.

The results of the experimental exposures to the LANSCE ICE House 30L neutron beam behind different shielding materials and the corresponding results of MCNP simulations are displayed in Table 6.2.

Material	Absorbed Dose Relative to Nominal Beam, Experiment	Absorbed Dose Relative to Nominal Beam, Simulation
Nominal Beam	1	1
5.34 g/cm^2 Al	0.772 ± 0.049	0.776 ± 0.155
5.38 g/cm^2 HDPE	0.470 ± 0.030	0.507 ± 0.101
5.3 g/cm^2 Al + 3.2 g/cm^2 HDPE	0.636 ± 0.041	0.481 ± 0.096

Table 6.2: The relative absorbed doses resulting from exposing the ATED to the LANSCE ICE House 30L neutron beam given different shielding configurations as well as the corresponding MCNP simulations.

The experimental and simulated results for ATED exposures behind different shielding are in close agreement for the 5.34 g/cm^2 Al and 5.38 g/cm^2 HDPE shielding configurations. However, the experimental data indicates a higher relative dose for the 5.3 g/cm^2 Al + 3.2 g/cm^2 HDPE shielding than does the corresponding MCNP data. There are several possible causes for the discrepancy between results. One potential cause of the disagreement is the uncertainty of the experimental beam spectrum and constituent particles. An AIREC calculated neutron spectrum was used in MCNP simulations, and the degree to which this differed from the LANSCE beam is unknown. Photons were present in the LANSCE beam, but prior testing has demonstrated that they contribute less than 2% of the total dose [Gersey, 2021]. As a result of their minimal contribution, photons were not included as source particles in MCNP simulations.

6.2. The Deep Space Test Bed Experiment.

6.2.1. Description of the Deep Space Test Bed Experiment.

In the Deep Space Test Bed (DSTB) experiment, a gondola designed to carry multiple instruments on high altitude balloon flights, was developed [Adams et al., 2007]. One DSTB experiment was conducted on June 8, 2005 in Ft. Sumner, New Mexico (34.5° N, 104.2° W). The goal of this experiment was to expose radiation detectors to the ionizing radiation present in the atmosphere and determine their effectiveness as dosimeters. Multiple detectors were flown aboard a balloon flight for 12 hours, and the majority of this time was spent at an altitude of ~120,000 ft. The detectors on the flight included three Liulin-4 Mobile Dosimetry Unit (MDU) portable silicon spectrometers exposed under different quantities of shielding: no shielding, 5 g/cm^2 aluminum, and a shielding carousel that rotated shielding materials throughout the flight [Benton, 2005].

6.2.2. Description of the Liulin-4 Mobile Dosimetry Unit

The Liulin-4 MDU was designed and manufactured by the Solar/Terrestrial Influences Laboratory in Sophia, Bulgaria. The active volume of the Liulin-4 MDU is a 2 cm^2 by 300 µm thick silicon chip. The silicon chip was housed between an aluminum case containing electronics and a 5 g/cm^2 aluminum shielding cap [Benton, 2005].

6.2.3. MCNP Materials and Geometry

Three separate MCNP simulations were run for each particle species, one with the Liulin-4 MDU behind no shielding, one with the Liulin-4 MDU behind a 1-meter inner radius shielding sphere containing 2.65 g/cm^2 of aluminum plus 1.5 g/cm^2 polyethylene, and one with the Liulin-4 MDU behind a shielding sphere containing 5.3 g/cm^2 of aluminum plus 3.0 g/cm^2 polyethylene, which approximates an aircraft wall. In the simulations with no shielding, the surrounding air density was 6.7266×10^{-6} g/cm^3, which corresponds to the air density at 120,000 ft [NOAA, 1976]. In the simulations with the aluminum and polyethylene shielding spheres, the interior air was at STP. The Liulin-4 MDU was modeled as a 300 μm thick, 2 cm^2 slab of silicon with an aluminum base of 10 g/cm^2 representing the electronics, and a 0.1 cm aluminum covering on top. Starting particles were generated uniformly on an outer spherical surface with an angle in the range from -90° to 90° with respect to an interior normal vector. The MCNP input geometry is shown in Figure 6.10.

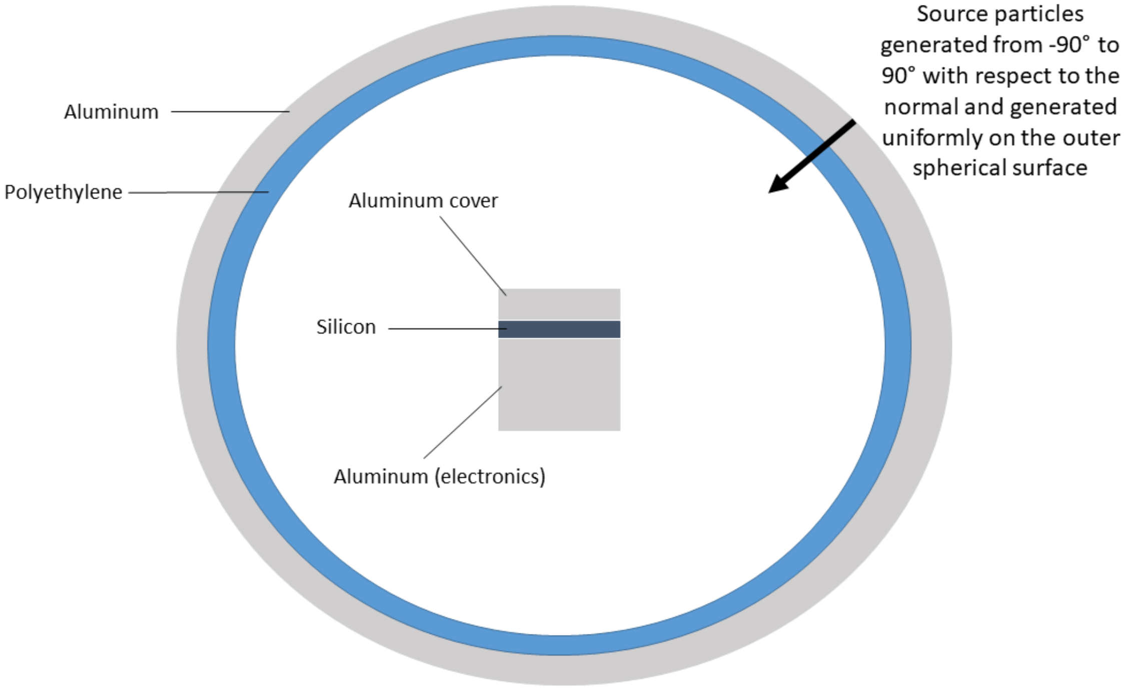

Figure 6.10: The Liulin-4 MDU geometric model for MCNP simulations of the DSTB flight.

Also simulated was a NASA Space Shuttle Tissue Equivalent Proportional Counter (TEPC) [Gersey et al., 2007]. The geometry of the Shuttle TEPC is displayed in Figure 6.11 and a simplified geometry of this TEPC was used in MCNP simulations. The same three shielding scenarios used in simulating the Liulin-4 MDU were used to simulate the Shuttle TEPC.

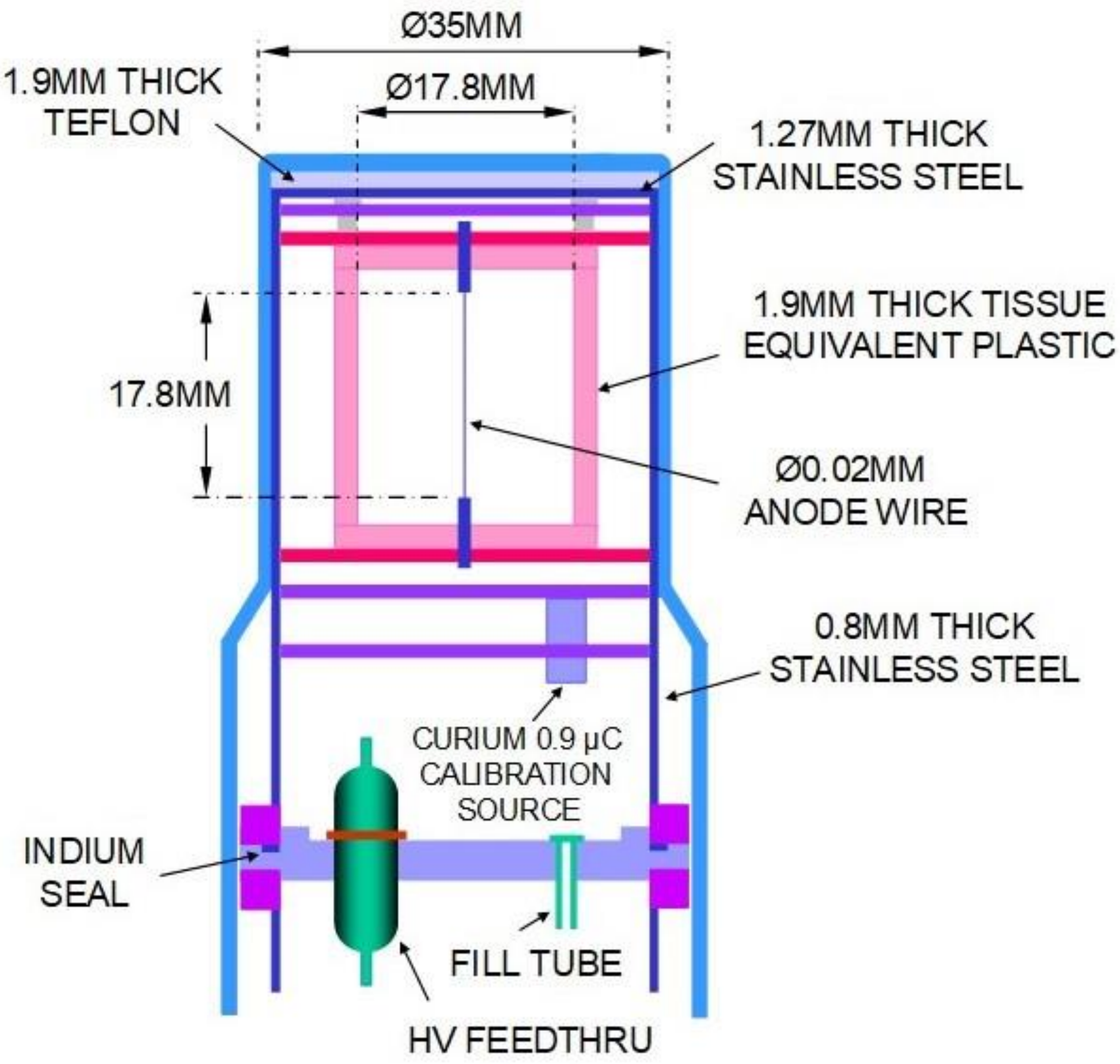

Figure 6.11: Diagram of the Shuttle TEPC [Gersey, 2020].

6.2.4. MCNP Incident Secondary Particle Spectra

AIREC was used to calculate the secondary flux spectra for the geographic coordinates and date of the DSTB flight for neutrons, photons, electrons and positrons, muons, charged pions, protons, deuterons, tritons, helions, and alphas, and these spectra are displayed in Figure 6.12. Each of these calculated spectra were used in separate simulations. This allowed for the determination of the contribution to the total absorbed dose due to each particle species individually as well as the total dose due to all secondary particle species. Sharp increases in flux in the proton and alpha particle spectra are observed between 10^3 MeV and 10^4 MeV. The peak represents the lowest energy GCR primary particles that can pass through the geomagnetic field and initiate EAS, while lower energy GCR are deflected away. Any protons or alpha particles with energies below the corresponding peak are secondary particles.

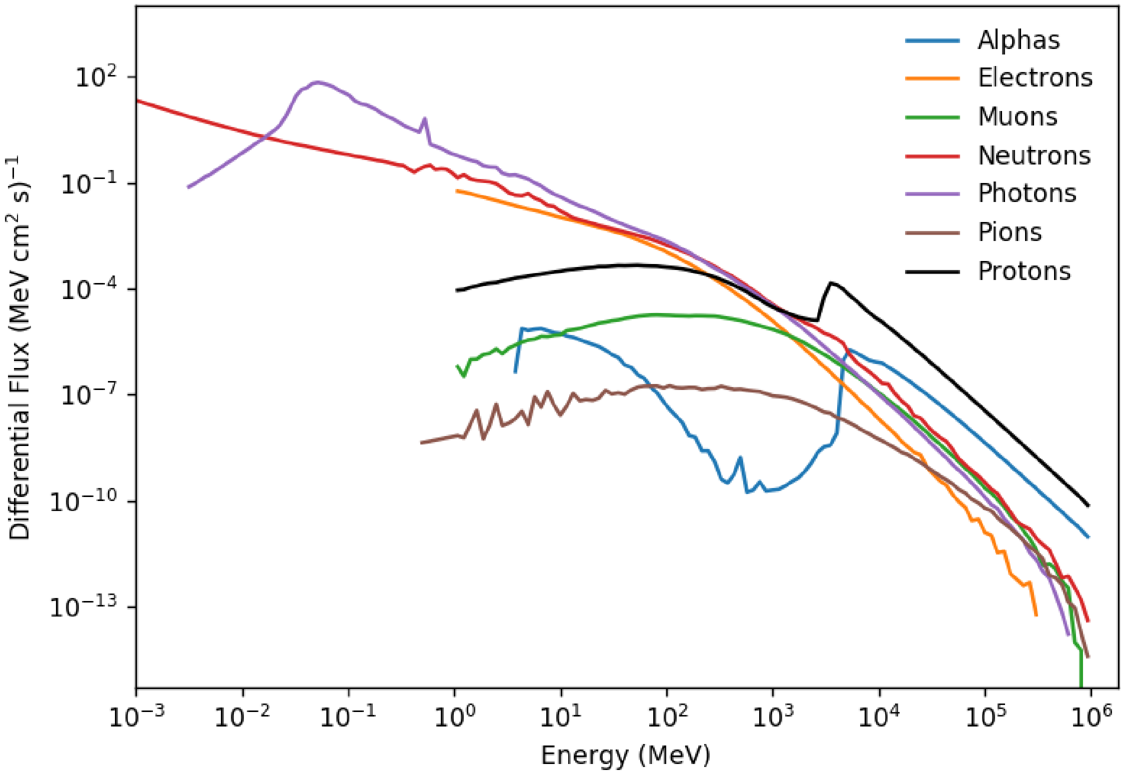

Figure 6.12: The AIREC calculated secondary flux spectra used in MCNP simulations of the DSTB experiment.

6.2.5. Comparison of Experiment to MCNP Simulated Results

Table 6.3 displays the average dose rates that resulted from the DSTB Liulin-4 MDU measurements and simulations. The MCNP simulation results agree with the DSTB experimental measurements within the range of the simulation and experimental uncertainties. Notably, it can be seen that additional shielding results in a higher absorbed dose rate, contrary to a naive *a priori* expectation. The increase in dose rate with additional shielding is due to the fact that many high energy secondary particles that are unshielded have low interaction probabilities with the Liulin-4 MDU Si detector. Addition of shielding increases the likelihood of some interaction taking place between the incident secondary particles near the Liulin-4 MDU, producing additional particles at lower average energies. These lower energy particles are more likely to interact with the Liulin-4 MDU. Furthermore, the interaction cross sections between neutron and silicon are relatively small [Weili and Watanabe, 2011], resulting in a small neutron dose rate registered by the unshielded Liulin-4 MDU. However, neutrons can produce secondary charged particles through nuclear interactions with the shielding material, and these secondary charged particles are much more likely to be detected than are the neutrons.

Data Type	Dose Rate (µGy/hr)
Experiment, unshielded	2.28 ± 0.78
Experiment, 5 g/cm^2 Al	2.55 ± 0.86
Experiment, shielding carousel	3.27 ± 1.07
MCNP, unshielded	2.06 ± 0.50
MCNP, 2.65 g/cm^2 Al + 1.5 g/cm^2 Poly	2.52 ± 0.61
MCNP, 5.3 g/cm^2 Al + 3.0 g/cm^2 Poly	3.03 ± 0.73

Table 6.3: The average dose rates (µGy/hr) resulting from the DSTB Liulin-4 MDU measurements along with the comparable MCNP simulation results.

The MCNP simulations provide insight that is not available from the experiment. MCNP can tally the dose for each particle species, revealing the which secondary particles are responsible for what fraction of the absorbed dose. The relevant secondary particle species and their contribution to the total absorbed dose rate as determined from MCNP simulations is diplayed for the unshielded Liulin-4 MDU, the Liulin-4 MDU with 2.65 g/cm^2 Al plus 1.5 g/cm^2 Polyethylene shielding, and the Liulin-4 MDU with 5.3 g/cm^2 Al + 3.0 g/cm^2 Polyethylene shielding in Tables 6.4, 6.5, and 6.6, respectively.

The four particle species that contributed the most to absorbed dose were neutrons, protons, electrons/positrons, and photons. The general trend of these particles in the different shielding configurations is described here. The total neutron dose rate increases by more than an order of magnitude from the unshielded Liulin-4 MDU simulation to the simulation of the Liulin-4 MDU with 5.3 g/cm^2 Al + 3.0 g/cm^2 Polyethylene shielding. Unshielded neutrons have a low interaction probability with the silicon of the Liulin-4 MDU, but the added shielding provides opportunities for the neutrons to interact and produce charged particles that are much more likely to contribute to the dose. The proton dose rate increased with increased shielding in the simulations. The incident protons are slowed by the shielding, increasing the linear energy transfer (LET) of the protons. The increased LET leads to more dose deposited in the detector. Both the 2.65 g/cm^2 Al + 1.5 g/cm^2 Polyethylene and 5.3 g/cm^2 Al + 3.0 g/cm^2 Polyethylene shields resulted in a decrease the electron dose rate compared to the nominal beam, but interestingly, the electrons dose rate was lower with less shielding. When electrons are slowed in the shielding material they release Bremsstrahlung photons, and the silicon detector is less sensitive to photons than to electrons, decreasing dose rate. With increased shielding as in the case of 5.3 g/cm^2 Al + 3.0 g/cm^2 Polyethylene shielding, the Bremsstrahlung photons produced by the initial shielding of the electrons have more opportunities to interact with the shielding material to produce additional electrons and positrons, thus increasing the dose rate as compared to the 2.65 g/cm^2 Al + 1.5 g/cm^2 Polyethylene shielding scenario. The photon dose rate increases with the added shielding, as the additional shielding material allows more opportunities for the photons to undergo Compton scattering, photoelectric effect, and pair production interactions, producing electrons and pair production positrons. The silicon detector is more sensitive to these charged particles than to the photons, increasing the dose rate.

Particle Species	Dose Rate (μGy/hr)	Percentage of Total
Neutrons	0.032	1.54%
Protons	1.07	52.13%
Electrons	0.643	31.29%
Negative Muons	0.011	0.53%
Positive Muons	0.014	0.69%
Photons	0.188	9.13%
Positive Pions	2.82×10^{-4}	0.01%
Negative Pions	2.11×10^{-4}	0.01%
Deuterons	0.030	1.44%
Tritons	0.002	0.13%
Helions	0.002	0.09%
Alphas	0.062	3.01%

Table 6.4: MCNP simulated Liulin-4 MDU with no shielding

Particle Species	Dose Rate (μGy/hr)	Percentage of Total
Neutrons	0.151	5.98%
Protons	1.416	56.11%
Electrons	0.505	20.00%
Negative Muons	0.011	0.44%
Positive Muons	0.015	0.58%
Photons	0.317	12.57%
Positive Pions	4.190×10^{-4}	0.02%
Negative Pions	3.015×10^{-4}	0.01%
Deuterons	0.012	0.47%
Tritons	0.001	0.05%
Helions	0.002	0.09%
Alphas	0.093	3.70%

Table 6.5: MCNP simulated Liulin-4 MDU with 2.65 g/cm^2 Al + 1.5 g/cm^2 Polyethylene shielding.

Particle Species	Dose Rate (μGy/hr)	Percentage of Total
Neutrons	0.448	14.78%
Protons	1.533	50.53%
Electrons	0.531	17.52%
Negative Muons	0.011	0.36%
Positive Muons	0.015	0.49%
Photons	0.373	12.30%
Positive Pions	4.86×10^{-4}	0.02%
Negative Pions	3.43×10^{-4}	0.01%
Deuterons	0.008	0.27%
Tritons	0.002	0.05%
Helions	0.003	0.08%
Alphas	0.109	3.59%

Table 6.6: MCNP simulated Liulin-4 MDU with 5.3 g/cm^2 Al + 3.0 g/cm^2 Polyethylene shielding.

Figures 6.13, 6.14, and 6.15 display energy deposition frequency spectra for protons, neutrons, electrons, and photons for each of the three Liulin-4 MDU shielding scenarios. These figures give a visual representation of the data presented in Tables 6.4, 6.5, and 6.6. Additionally, the data in the tables is integrated, while Figures 6.13, 6.14, and 6.15 display spectra. In each case the protons dominate the contribution, but just as seen in Tables 6.4-6.6, the relative contributions from photons and neutrons increase when shielding is added.

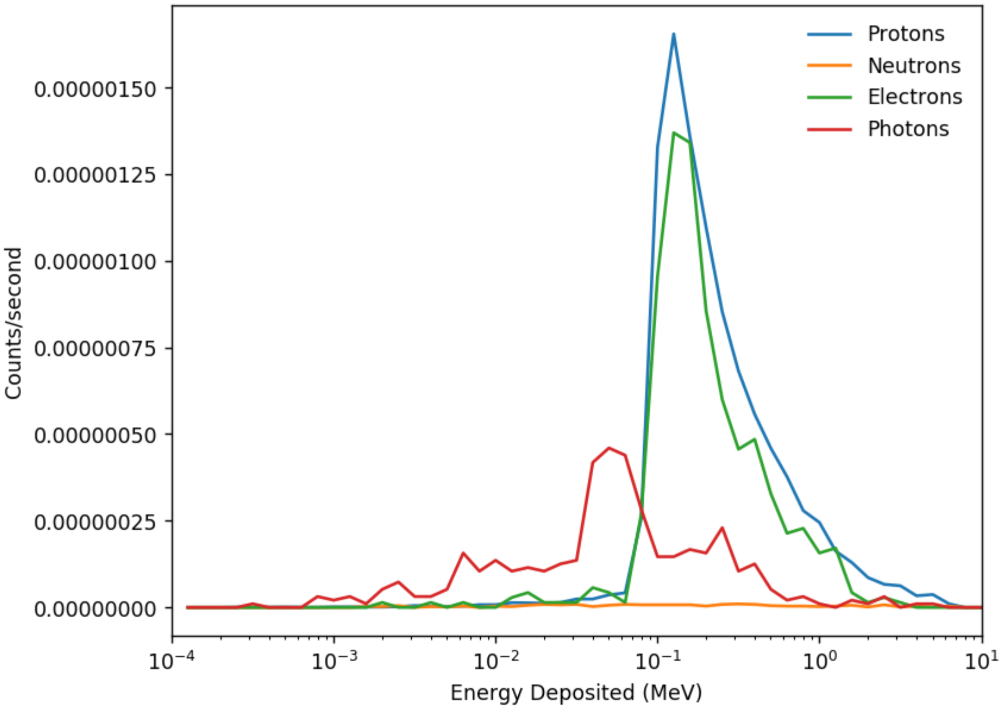

Figure 6.13: MCNP simulated energy deposition spectrum for the unshielded Liulin-4 MDU.

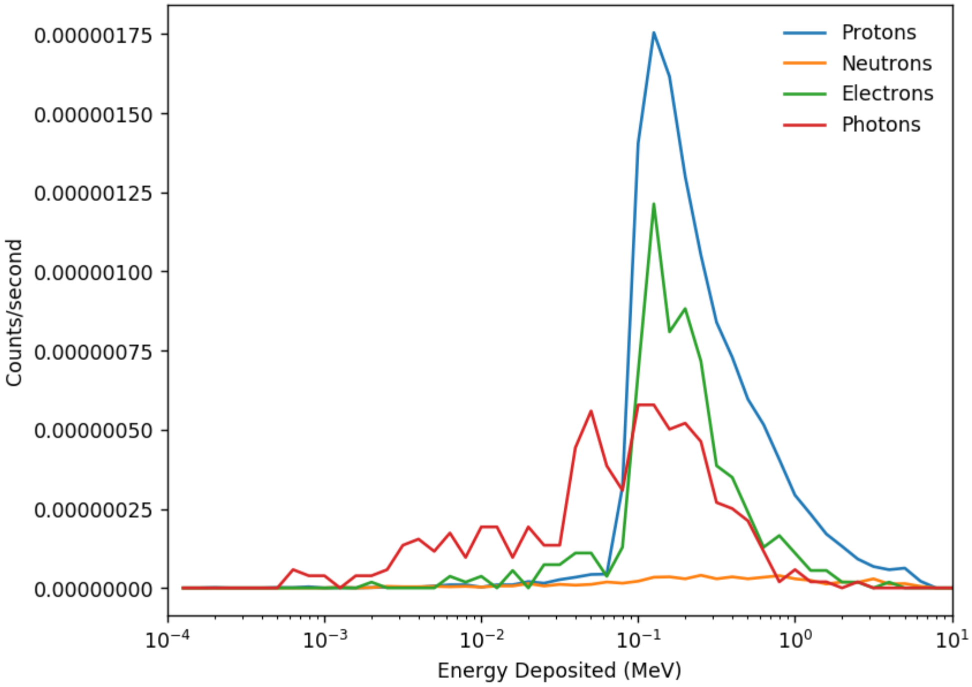

Figure 6.14: MCNP simulated energy deposition spectrum for the Liulin-4 MDU with 2.65 g/cm^2 Al + 1.5 g/cm^2 Polyethylene shielding.

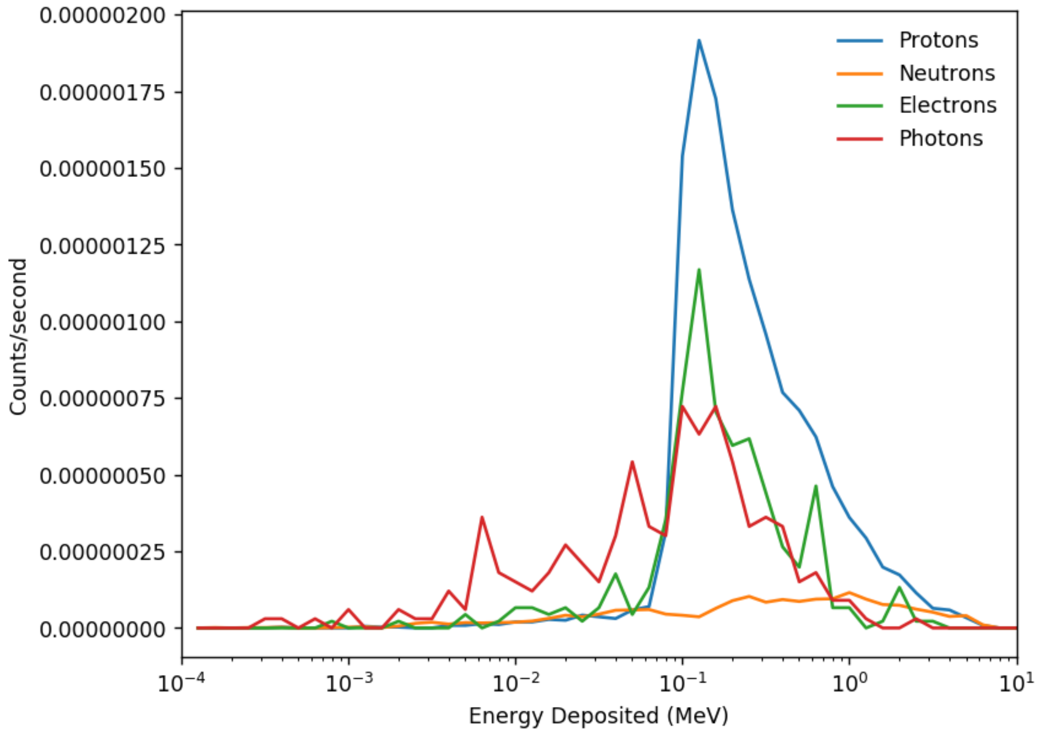

Figure 6.15: MCNP simulated energy deposition spectrum for the Liulin-4 MDU with 5.3 g/cm^2 Al + 3 g/cm^2 Polyethylene shielding.

The results of the Shuttle TEPC simulations are displayed in Figures 6.14, 6.15, 6.16 and Tables 6.7, 6.8, and 6.9. Each figure displays a yd(y) versus lineal energy curve, similar to the curve shown for the ATED simulations in Figure 6.6. For Figure 6.6, neutrons were the only source present, while for Figures 6.14, 6.15, and 6.16 the protons, electrons, and photons curves are also shown. As mentioned when discussing the ATED experiment at LANSCE, the area under the yd(y) versus lineal energy curve is proportional to absorbed dose.

Additional shielding increased the absorbed dose tallied by the simulated Shuttle TEPC when compared to the unshielded case. Shielding shifts the energy spectrum of the incident particles to lower energies where interaction cross sections are higher, making interactions more likely. The shielding also increased the percentage contribution due to neutrons and photons as compared to the unshielded case. The neutrons and photons can produce charged particles in the shielding that are more easily detected by the Shuttle TEPC.

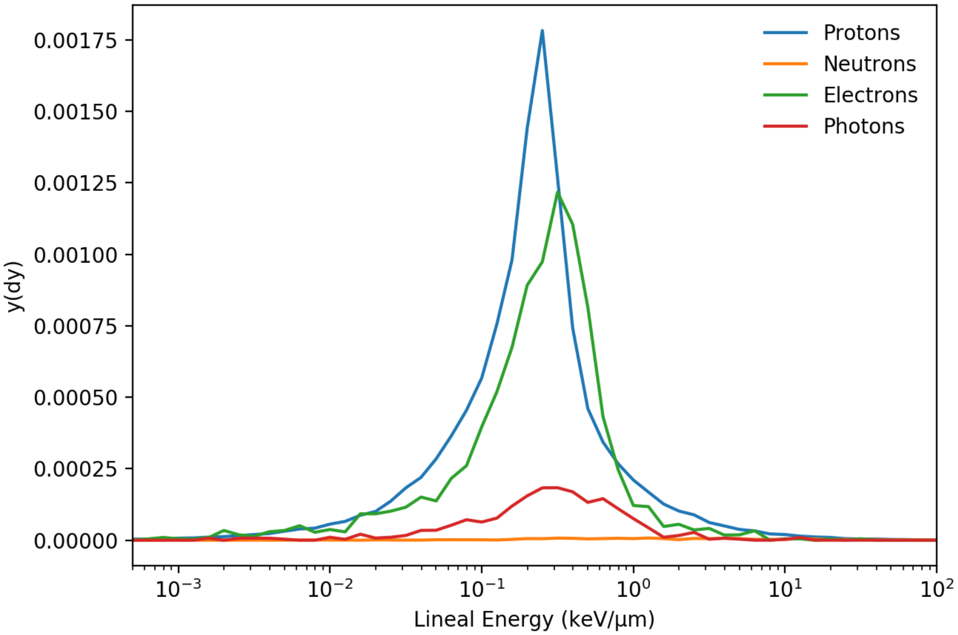

Figure 6.16: The lineal energy spectra due to secondary protons, neutrons, electrons, and photons as recorded in simulations of an unshielded TEPC aboard a DSTB balloon flight.

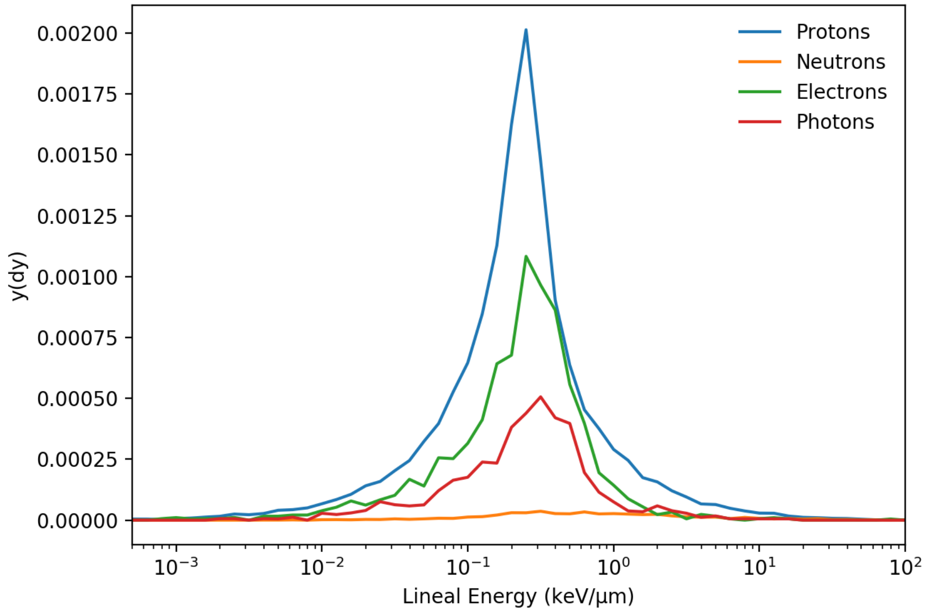

Figure 6.17: The lineal energy spectra due to secondary protons, neutrons, electrons, and photons as recorded in simulations of a TEPC behind 2.65 g/cm^2 Al + 1.5 g/cm^2 Polyethylene shielding aboard a DSTB balloon flight.

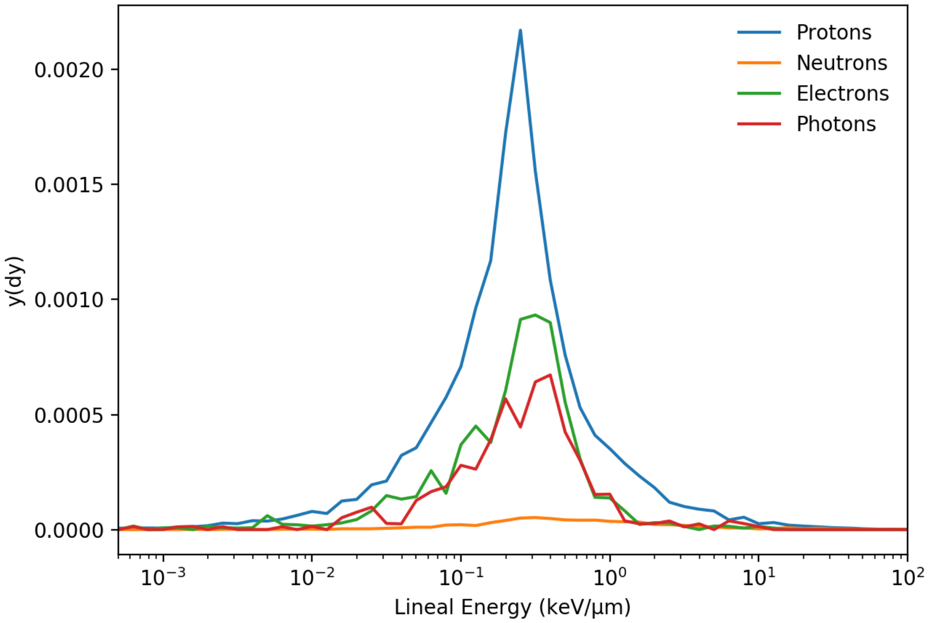

Figure 6.18: The lineal energy spectra due to secondary protons, neutrons, electrons, and photons as recorded in simulations of a TEPC behind 5.3 g/cm^2 Al + 3.0 g/cm^2 Polyethylene shielding aboard a DSTB balloon flight.

In real-world measurements made using the Shuttle TEPC, lineal energy readings below 1 keV/μm are indistinguishable from background noise in the instrument, so only lineal energies above this are considered. Tables 6.7, 6.8, and 6.9 display the contribution to the total dose due to each particle, but only contributions greater than or equal to 1 keV/μm were included in these calculations.

Particle Species	Percentage of Total
Neutrons	3.96%
Protons	50.06%
Electrons	26.05%
Negative muons	0.22%
Positive muons	0.28%
Negative pions	0.01%
Positive pions	0.01%
Photons	10.25%
Deuterons	2.23%
Tritons	0.14%
Helions	0.19%
Alphas	6.60%

Table 6.7: Dose contribution from each particle species as determined from MCNP simulations of the Shuttle TEPC with no shielding.

Particle Species	Percentage of Total
Neutrons	8.31%
Protons	55.09%
Electrons	16.28%
Negative muons	0.17%
Positive muons	0.23%
Negative pions	0.01%
Positive pions	0.01%
Photons	12.77%
Deuterons	0.75%
Tritons	0.06%
Helions	0.15%
Alphas	6.17%

Table 6.8: Dose contribution from each particle species as determined from MCNP simulations of the Shuttle TEPC with 2.65 g/cm^2 Al + 1.5 g/cm^2 Polyethylene shielding.

Particle Species	Percentage of Total
Neutrons	8.27%
Protons	57.90%
Electrons	12.88%
Negative muons	0.15%
Positive muons	0.20%
Negative pions	0.01%
Positive pions	0.01%
Photons	13.68%
Deuterons	0.47%
Tritons	0.06%
Helions	0.15%
Alphas	6.20%

Table 6.9: Dose contribution from each particle species as determined from MCNP simulations of the Shuttle TEPC with 5.3 g/cm^2 Al + 3.0 g/cm^2 Polyethylene shielding.

6.3. Conclusions

The ability to use AIREC to calculate the secondary particle flux that detectors are subject to in the atmosphere provides previously unavailable insights into the physics of these experiments. Monte Carlo radiation transport simulations of these experiments provide details about which particle species are of primary concern. This insight can be used to solve practical problems such as when it is appropriate to use shielding. The DSTB flight simulations demonstrate that even a significant amount of shielding can actually increase the dose compared to an unshielded detector. It might be expected that the neutron dose rate would increase with added shielding, but the proton dose rate increased as well.

The combination of AIREC spectra and MCNP simulations proved effective for experiments in both the controlled environment of the LANSCE facility and in an uncontrolled environment during the DSTB experiments. This combination likewise proved effective for two completely different detectors, the ATED and the Liulin-4 MDU. This provides optimism for use in future analysis of atmospheric radiation detection experiments.

CHAPTER VII

CONCLUSIONS

7.1. Scope of This Work

The goal of this research to develop a tool that returns the secondary particle flux given coordinates on the globe, a date, and particle(s) of interest was satisfied with the development of AIREC. AIREC is the most complete model of the SSAIRE that has been developed to date. The ability to calculate secondary flux spectra also allows for higher fidelity modeling of atmospheric radiation detection experiments than previously was possible. As shown in chapter 6, AIREC calculated spectra can be used as inputs in Monte Carlo radiation transport codes, and the response of a detector can be accurately simulated. Not only can experimental results be reproduced, but additional insights can also be gained. For example, the contribution to the detector signal due to each species of particle can be determined. Such information is useful when determining whether to shield radiation, as different types of radiation are more easily shielded by different materials. In some cases, the chapter 6 data showed that added shielding actually increases the dose, so in those cases it may be better not to shield at all. Understanding the SSAIRE will only become more relevant as suborbital flights become more common and more technologies involve electronics in the atmosphere where they are exposed to elevated radiation levels.

Because AIREC can be used to determine the secondary particle flux for any location and date, it has broad applicability. In chapter 6 a few examples were given in which AIREC was used to better understand the results of radiation detection experiments. However, AIREC could be used to better understand a wide variety of fields including avionics, lightning initiation, cosmic ray effects on climate change, and more.

7.2. Future Work

7.2.1. Further Development of AIREC

The only GCR model currently available in AIREC is the ISO model. The ISO model calculates the solar modulation of GCR using the observed sunspot number as an input. Other GCR models, such as the Badhwar O'Neil model, have also been developed. The Badhwar O'Neil GCR model uses neutron ground monitor data to determine the solar modulation of GCR. Having the choice between two different GCR models that employ two different methods for tracking the solar modulation of GCR is a feature that should be added to AIREC. Of the future developments of AIREC discussed in this section, the addition of the Badhwar O'Neil GCR model is the foremost priority, and it can be incorporated into AIREC without running additional MCNP simulations.

Throughout this research, areas for improvement of AIREC were discovered. In the MCNPX simulations that provided the data used to develop AIREC, the highest energy GCR simulated were 1 TeV. Although >1 TeV GCR are rare, they can produce interesting events. MCNP is not well suited for >1 TeV energy particle transport, but a code such as FLUKA is more geared towards the transport of these high energy particles. Future versions could include data for the transport of >1 TeV GCR primary particles.

Similarly, GCR primary particles with atomic number greater than 26 were not included in AIREC calculations. As is the case with greater than 1 TeV GCR, greater than 26 atomic number GCR have minimal contribution to the SSAIRE, but they can produce rare events worthy of study. Further simulations could be conducted to model the EAS produced by these higher atomic number GCR, and these results could be included in future versions of AIREC.

Solar particle events (SPE) can produce high energy particles, primarily consisting of protons, and it is possible for particles resulting from SPE to have a greater flux in a region of the atmosphere than the flux of GCR. This results in more secondary particles due to SPE than due to GCR. Such high energy and high flux SPE are relatively rare, and there is no model available for predicting when such SPE will occur. However, historical data could be analyzed to approximate either the spectrum of incident solar particles or the secondary flux that resulted from each SPE. The SPE produced secondary particles would be added to the GCR produced secondary particles for the time and location in which the SPE occurred.

Only fully ionized nuclei were considered as GCR primary particles. While these do account for the vast majority of air showers, there are both gamma ray and electron/positron initiated EAS. Recall from chapter 2 that the three components of an EAS, the hadronic, muonic, and electromagnetic components, can be treated as independent from one another. When EAS are initiated by GCR primary gamma rays, only an electromagnetic component is present. These gamma ray initiated showers account for well under 1% of all showers, and they are often indistinguishable from the electromagnetic component of hadron initiated EAS in experiments [Greider, 2010]. Electron and positron initiated showers are likewise minimally contributing to the SSAIRE as a whole and generally cannot be distinguished from the electromagnetic component of hadron initiated showers. Although the electromagnetic component of the GCR primary particles produce much smaller EAS than do fully ionized nuclei, their inclusion would give a more complete description of the SSAIRE, and they could be incorporated into future versions of AIREC.

AIREC can be used to calculate secondary particle spectra at any altitude up to 100 km. The 1976 US Standard Atmosphere model was referenced in constructing the MCNP simulations that were used in developing AIREC. The 1976 US Standard Atmosphere includes atmospheric data for altitudes up to 1,000 km [NOAA, 1976]. Novel MCNP simulations could be run to generate data for altitudes over 100 km, and these results could be used to raise the AIREC altitude ceiling.

Comparisons of AIREC results to experimental results in chapter 5 revealed inconsistencies at low altitudes. In the original MCNPX simulations that provided the data on which AIREC was built, the Earth was modeled as a sphere of water. In most experiments that take place on the ground, the surface is soil, concrete, or some other solid material. The degree to which the surface material affects secondary particle back scatter has not yet been determined. Further simulations could be conducted in MCNP with different ground materials to determine how the secondary flux spectrum changes with material changes. A surface material option for inputs at low altitudes could be added to AIREC to account for these ground material changes.

The day versus night variation in secondary particle flux, i.e. the diurnal variation, is a phenomenon that is known to occur, but it is not well understood at a fundamental level. There is no current consensus model for the calculation of diurnal variation, making the implementation of the diurnal effect into AIREC less straight forward than the previously mentioned additions. However, past experimental data could be analyzed and further experiments could be conducted to determine the amount of diurnal variation on a regional basis, and this variation could be incorporated in future versions of AIREC.

7.2.2. Further Use of AIREC in Analyzing the SSAIRE

One of the difficulties in validating AIREC is the lack of experimental and computer model data with which to make a comparison. Future work needs to be done in validating results as additional atmospheric radiation detection experiments are conducted and more models are developed.

In chapter 6, two examples of the novel use of AIREC were explored. One of these examples was using AIREC spectra as inputs into MCNP simulations to model the silicon based radiation detectors aboard the Deep Space Test Bed (DSTB) balloon flight. Further uses of AIREC in this capacity are already underway. Past experiments exposing silicon based radiation detectors to atmospheric ionizing radiation were conducted aboard NASA ER-2 flights [Benton, 2004]. The NASA ER-2 aircraft are designed for altitudes of 20,000 feet to 70,000 feet, and data was collected at several different altitudes during the experiments conducted by [Benton, 2004]. The availability of data across a variety of altitudes allows for further points of verification of AIREC.

REFERENCES

[Aartsen et al., 2016] The IceCube Collaboration, Aartsen, M.G. et al., “Anisotropy in Cosmic-Ray Arrival Directions in the Southern Hemisphere with Six Years of Data from the IceCube Detector,” The Astrophysical Journal 826 2. 2016. arxiv.org/abs/1603.01227

[Adams et al., 2007] Adams, J. et al. “Deep Space Test Bed for Radiation Studies,” Nuclear Instruments and Methods in Physics Research Section A: Accelerators, Spectrometers, Detectors and Associated Equipment, Volume 579, Issue 1, Pages 522-525, ISSN 0168-9002. 2007. https://doi.org/10.1016/j.nima.2007.04.114.

[Aharonian, 2019] Aharonian, F., Yang, R., and Wilhelmi, E. “Massive Stars as Major Factories of Galactic Cosmic Rays,” Nature Astronomy, 3. Pages 561-567. 2019. https://doi.org/10.1038/s41550-019-0724-0

[Ali, 2014] Ali, F. “Design and Characterization of Next-Generation Tissue Equivalent Proportional Counters for Use in Low Energy Neutron,” Faculty of Energy Systems and Nuclear Science University of Ontario Institute of Technology. Fields Thesis. 2014.

[Ali et al., 2014] Ali, F., Waker, A., Waller, E. “Intercomparison of Monte Carlo radiation transport codes to model TEPC response in low-energy neutron and gamma-ray fields,” Radiation Protection Dosimetry. 2014. 161(1-4):257-260. doi:10.1093/rpd/nct260

[Amenomori, 2006] Amenomori et al. “Anisotropy and Corotation of Galactic Cosmic Rays,” Science, Volume 314, Issue 5798, Pages 439-443. 2006. 10.1126/science.1131702

[Ameri, 2019] Ameri D. et al. “Properties of High-Energy Solar Particle Events Associated with Solar Radio Emissions,” Springer, Solar Physics 294, Article number 122. 2019.

[Anderson, 1932] Anderson, C. “The Apparent Existence of Easily Deflectable Positives,” Science, Volume 76, Pages 238-239. 1932.

[ATLAS Collaboration, 2012] Aad, G. et al. “Observation of a new particle in the search for the Standard Model Higgs boson with the ATLAS detector at the LHC,” Physics Letters B. Volume 716, Issue 1, Pages 1-29. 2012. https://doi.org/10.1016/j.physletb.2012.08.020.

[Auger et al., 1939] Auger, P., et al. “Extensive Cosmic Ray Showers.” Reviews of Modern Physics, Volume 11, Pages 288-291. 1939. https://doi.org/10.1103/RevModPhys.11.288

[Beatty et al., 2019] Beatty, J.J., Matthews, J., and Wakely, S.P. “Cosmic Rays,” The Review of Particle Physics, 2019. https://pdg.lbl.gov/2019/reviews/rpp2019-rev-cosmic-rays.pdf

[Beaujean, 1993] Beaujean R. “Influence of the Geomagnetic Field and of the Solar Activity Cycle on the Cosmic Ray Energy Spectrum,” In: Swenberg C.E., Horneck G., Stassinopoulos E.G. (eds) Biological Effects and Physics of Solar and Galactic Cosmic Radiation. NATO ASI Series (Series A: Life Sciences), Volume 243B. Springer, Boston, MA. 1993. https://doi.org/10.1007/978-1-4615-2916-3_2

[Benton, 2004] Benton E. Radiation Dosimetry at Aviation Altitudes and in Low-Earth Orbit. Thesis, University College, Belfield, Dublin 4, Ireland. 2004.

[Benton, 2005] Benton, E. Test of the DSTB Passive Dosimeter System on the DSTB Certification Flight. ERI Report No. 050901. 2005.

[Benton and Benton, 2001] Benton, E.R. and Benton, E.V. “Space radiation dosimetry in low-Earth orbit and beyond,” Nuclear Instruments and Methods in Physics Research Section B: Beam Interactions with Materials and Atoms, Volume 184, Issues 1–2, Pages 255-294, ISSN 0168-583X. 2001. https://doi.org/10.1016/S0168-583X(01)00748-0.

[Beringer, 2012] Beringer, J. et al. Particle Data Group. PR D86, 010001. 2012. http://pdg.lbl.gov

[Bird et al., 1995] Bird, H.E. et al. “Detection of a cosmic ray with measured energy well beyond the expected spectral cutoff,” Astrophysics Journal, Volume 441. Pages 144–150. arXiv:astro-ph/9410067

[Blasi, 2013] Blasi, P. “The origin of galactic cosmic rays,” Astronomy Astrophysics Review, Volume 21, Article number 70. 2013. https://doi.org/10.1007/s00159-013-0070-7

[Böhlen et al., 2014] Böhlen, T.T. et al. "The FLUKA Code: Developments and Challenges for High Energy and Medical Applications." Nuclear Data Sheets 120, Pages 211-214. 2014.

[Booz et al., 1983] Booz, J., et al. “Microdosimetry.” ICRU Report 36. International Commission on Radiation Units and Measurement. 1983.

[Bottollier-Depois et al., 2012] European Radiation Dosimetry Group, Bottollier-Depois et al., “Comparison of Codes Assessing Radiation Exposure of Aircraft Crew due to Galactic Cosmic Radiation,” EURADOS Report. 2012.

[Bramblett et al., 1960]. Bramblett, R., Ewing, R., Bonner, T. “A New Type of Neutron Spectrometer,” Nuclear Instruments and Methods. Volume 9, Issues 1, Pages 1-12. 1960. https://doi.org/10.1016/0029-554X(60)90043-4

[Brunberg and Dattner, 1954] Brunberg, E. A. and Dattner, A. “On the Interpretation of the Diurnal Variation of Cosmic Rays,” Tellus, Volume 6, Issue 1, Pages 73-83, 1954. 10.3402/tellusa.v6i1.8705

[Bütikofer, 2018] Bütikofer, R. “Cosmic Ray Particle Transport in the Earth’s Magnetosphere,” In: Malandraki O., Crosby N. (eds) Solar Particle Radiation Storms Forecasting and Analysis. Astrophysics and Space Science Library, Springer, Volume 444. 2018. https://doi.org/10.1007/978-3-319-60051-2_5

[Cane et al., 2003] Cane, H., Vonrosenvinge, T., Cohen, C., and Mewaldt, R. “Two Components in Major Solar Particle Events,” Geophysical Research Letters, Volume 30, Issue 12. 2003. https://doi.org/10.1029/2002GL016580

[Carlson and Watson, 2014] Carlson, P. and Watson, A. A. “Erich Regener and the ionisation maximum of the atmosphere,” History of Geo- and Space Sciences, Volume 5, Pages 175-182, 2014. https://doi.org/10.5194/hgss-5-175-2014

[Castellina and Donato, 2013] Castellina A, Donato F. “Astrophysics of Galactic Charged Cosmic Rays,” In Planets, Stars and Stellar Systems. Volume 5, Pages 725-788. 2013.

[Cliver et al., 1990] Cliver E.W. et al. “An estimate of the maximum speed of the solar wind 1938–1989,” Journal of Geophysical Research, Space Physics, Volume 95, Issue A10, Pages 17103-17112. 1990. https://doi.org/10.1029/JA095iA10p17103

[Chadwick and Young, 2011]. Chadwick, M., Young, P. ENDF/B-VIII.0. N-14(N,TOT), SIG 2011.

[Clem, 2004] Clem, J. M., De Angelis, G., Goldhagen, P. and Wilson, J. W. “New calculations of the atmospheric cosmic radiation field—results for neutron spectra,” Radiation Protection Dosimetry, Volume 110, Issue 1–4, Pages 423–428. 2004. https://doi.org/10.1093/rpd/nch175

[Cooper, 2012] Cooper, N. G., “The Invisible Neutron Threat,” National Security Science, Issue 1, Pages 12–17, 2012. https://www.lanl.gov/science/NSS/issue1_2012/story4full.shtml

[Copeland, 2014] Copeland, K. “Cosmic Ray Particle Fluences in the Atmosphere Resulting From Primary Cosmic Ray Heavy Ions and Their Resulting Effects on Dose Rates to Aircraft Occupants as Calculated with MCNPX 2.7.0” [Report]. –Royal Military College of Canada, 2014.

[Copeland, 2017] Copeland, K. “CARI-7A: Development and Validation,” Radiation Protection Dosimetry, Volume 175, Issue 4, Pages 419-431, 2017. https://doi.org/10.1093/rpd/ncw369

[Cronin, 1999] Cronin J.W. “Cosmic Rays: The Most Energetic Particles in the Universe,” In: Bederson B. (eds) More Things in Heaven and Earth. Springer, New York, NY. 1999. https://doi.org/10.1007/978-1-4612-1512-7_17

[DONUT Collaboration, 2001] Kodama, K. et al. “Observation of Tau Neutrino Interactions,” Physics Letters B, Volume 504, Issue 3, Pages 218-224. 2001. https://doi.org/10.1016/S0370-2693(01)00307-0.

[Drury, 2012] Drury, Luke O. ‘C., “Origin of Cosmic Rays,” Astroparticle Physics, Volume 39, Pages 52-60, 2012. https://arxiv.org/abs/1203.3681

[Dupree and Fraley, 2002] Dupree, S. and Fraley, S. “A Monte Carlo Primer - A Practical Approach to Radiation Transport,” Kluwer Academic, NY. 2002.

[Dyer and Truscott, 1999] Dyer, C. and Truscott, P. “Cosmic Radiation Effects on Avionics,” Radiation Protection Dosimetry, Volume 86, Issue 4, Pages 337-342, 1999. https://doi.org/10.1093/oxfordjournals.rpd.a032970

[Engel et al., 2011] Engel R. et al. “Extensive Air Showers and Hadronic Interactions at High Energy,” Annual Review of Nuclear and Particle Science, Volume 61, Pages 467-489. 2011. https://doi.org/10.1146/annurev.nucl.012809.104544

[E.V. Benton RPL, 2019] The E.V. Benton Radiation Physics Laboratory at Oklahoma State University. “Studies in Cosmic Ray Muons.” 2019. https://physics.okstate.edu/news/93-pages/540-benton-rpl-studies-in-cosmic-ray-muons

[Ferrari et al., 1997] Ferrari A. et al. “Fluence to Effective Dose Conversion Coefficients for Neutrons up to 10 TeV.” Radiation Protection Dosimetry. Volume 71, Issue number 3, Pages 165-173. 1997.

[Ferrari et al., 2000]. Ferrari, A., Pelliccioni, M., and Rancati, T. “Calculation of the Radiation Environment Caused by Galactic Cosmic Rays for Determining Air Crew Exposure,” Radiation Protection Dosimetry, Volume 93, Issue number 2, Pages 101-114. 2001.

[Ferrari et al., 2005] A. Ferrari et al. "FLUKA: a multi-particle transport code." CERN-2005-10, INFN/TC_05/11, SLAC-R-773. 2005.

[Gersey et al., 2003]. Gersey, B., et al. “Correlation of Neutron Dosimetry Using a Silicon Equivalent Proportional Counter Microdosimeter and SRAM SEU Cross Sections for Eight Neutron Energy Spectra,” IEEE Transactions on Nuclear Science, Volume 50, Issue number 6. 2003.

[Gersey et al., 2007]. Gersey, B., et al. “Comparison of a Tissue Equivalent and a Silicon Equivalent Proportional Counter Microdosimeter to High-Energy Proton and Neutron Fields,” IEEE Transactions on Nuclear Science, Volume 54, Issue number 6, 2007.

[Gersey, 2020]. Gersey, B. Private communication. 2020.

[Gersey, 2021]. Gersey, B. Private communication. 2021.

[Goldhagen et al., 2002] Goldhagen, P., Reginatto, M., Kniss, T., Wilson, J., Singleterry, R., Jones, I., Van Steveninck, W. “Measurement of the energy spectrum of cosmic-ray induced neutrons aboard an ER-2 high-altitude airplane,” Nuclear Instruments and Methods in Physics Research Section A: Accelerators, Spectrometers, Detectors and Associated Equipment, Volume 476, Issues 1–2, Pages 42-51, ISSN 0168-9002. 2002. https://doi.org/10.1016/S0168-9002(01)01386-9

[Goldhagen et al., 2003] Goldhagen, P., Clem, J., Wilson, J. “Recent results from measurements of the energy spectrum of cosmic-ray induced neutrons aboard an ER-2 airplane and on the ground,” Advances in Space Research, Volume 32, Issue 1, Pages 35-40, ISSN 0273-1177. 2003. https://doi.org/10.1016/S0273-1177(03)90367-X

[Goldhagen et al., 2004]. Goldhagen, P. et al. “The Energy Spectrum of Cosmic-Ray Induced Neutrons Measured on an Airplane over a Wide Range of Altitude and Latitude,” Radiation Protection and Dosimetry. Volume 110, Issue 1-4, Pages 387-392. 2004. https://doi.org/10.1093/rpd/nch216

[Grieder, 2001] Grieder P. “Cosmic Rays at Earth: Researcher’s Reference Manual and Data Book,” Elsevier. 2001.

[Grieder, 2010] Grieder P. “Extensive Air Showers: High Energy Phenomena and Astrophysical Aspects - A Tutorial,” Reference Manual and Data Book. Springer. 2010.

[Griffiths, 1987] Griffiths, D. J. “Introduction to Elementary Paricles,” 1st Edition. John Wiley & Sons, Inc. 1987.

[Gurevich et al., 1992] Gurevich, A., Milikh, G., Roussel-Dupre, R. “Runaway electron mechanism of air breakdown and preconditioning during a thunderstorm,” Physics Letters A, Volume 165, Issues 5–6, Pages 463-468, ISSN 0375-9601, 1992. https://doi.org/10.1016/0375-9601(92)90348-P.

[Hale et al., 2011]. Hale, Young, Chadwick, Caro, Lubitz. ENDF/B-VII.1. O-16(N,TOT), SIG 2011.

[Hands et al., 2016] Hands A.D.P. et al. “The disappearance of the pfotzer-regener maximum in dose equivalent measurements in the stratosphere,” Space Weather, Volume 14, Issue 10, Pages 776-785. 2016. https://doi.org/10.1002/2016SW001402

[Haungs and Roth, 2003] Haungs A., Rebel H., and Roth M. “Energy Spectrum and Mass Composition of High-Energy Cosmic Rays,” Reports on Progress in Physics, Volume 66, Number 7, 2003.

[Hayes, 2020] Hayes, Bryan. “Analysis of Measurements and Improvements upon the Active Tissue Equivalent Dosimeter,” Oklahoma State University, Doctoral Thesis. 2020.

[Hess, 1912]. Hess, V. “On the Observations of the Penetrating Radiation,” Translated by Angelis, A. and Schultz C. 1912. arXiv:1808.02927

[Hughes and James, 2014] Hughes, H.G. and James, M.R. "Advanced Tallies", 2014. LA-UR-14-21281, pp. 223-282

[ISO, 2004] ISO (International Standards Organization). “Space environment (natural and artificial) --Galactic cosmic ray model,” ISO 15930:2004. Geneva, Switzerland: ISO; 2004

[Jokipii, 1971] Jokipii, J. R., “Propagation of cosmic rays in the solar wind,” Reviews of Geophysics, Volume 9, Issue 1, Pages 27–87. 1971. 10.1029/RG009i001p00027.

[Kampert and Watson, 2012] Kampert, KH., Watson, A.A. “Extensive air showers and ultra high-energy cosmic rays: a historical review,” The European Physical Journal H, Volume 37, Pages 359–412. 2012. https://doi.org/10.1140/epjh/e2012-30013-x

[Kimura, 2019]. Kimura S. “High-energy emission from neutron star mergers,” European Physical Journal Web of Conferences. Volume 210. 2019. https://arxiv.org/abs/1903.06221

[Knoll, 2010] Knoll G. “Radiation Detection and Measurement,” Fourth Edition. John Wiley & Sons, Inc. 2010.

[Krane, 1988] Krane, Kenneth. “Introductory Nuclear Physics,” John Wiley & Sons, Inc. 1988.

[Knuth, 1981] Knuth, Donald. “The Art of Computer Programming, Vol. 2: Semi-numerical Algorithms,” 2nd Edition, Addison-Wesley, Reading, MA. 1981.

[Lang, 2010] Lang, K. ”NASA’s Cosmos,” Tufts University. 2010. https://ase.tufts.edu/cosmos/view_picture.asp?id=326

[LANL, 2018] LANSCE 2018 Run Cycle Report.

[Lattes et al., 1947] Lattes, C., Muirhead, H., Occhialini, G., and Powell, C. “Processes Involving Charged Mesons,” Nature, Volume 159, Pages 694-697. 1947.

[LHC, 2018]. “LHC Season 2 facts & figures.” 2018. https://home.cern/sites/home.web.cern.ch/files/2018-07/factsandfigures-en_0.pdf

[Lindborg et al., 1999]. Lindborg, L., Kyllönen, J., Beck, P., Bottollier-Depois, J., Gerdung, S., Grillmaier, R., Schrewe U. “The Use of TEPC for Reference Dosimetry,” Radiation Protection Dosimetry, Volume 86, Issue 4, Pages 285–288. 1999. https://doi.org/10.1093/oxfordjournals.rpd.a032959

[Lindy, 2014] Lindy N. “The Role of Cosmic Rays in Lightning Initiation,” Oklahoma State University. 2014. https://hdl.handle.net/11244/14971

[Lindy et al., 2018] Lindy, N., Benton, E. Beasley, W., Petersen, D. “Energetic cosmic-ray secondary electron distribution at thunderstorm altitudes,” Journal of Atmospheric and Solar-Terrestrial Physics, Volume 179, Pages 435-440, ISSN 1364-6826, 2018. https://doi.org/10.1016/j.jastp.2018.10.003.

[Little, 2012] Little, R. “V&V of MCNP and Data Libraries at Los Alamos.” 2012. LA-UR-12-26307

[Loon, 2021] https://loon.com/technology/

[Lowes, 2007] Lowes F. “Geomagnetic Dipole Field,” In: Gubbins D., Herrero-Bervera E. (eds) Encyclopedia of Geomagnetism and Paleomagnetism. Springer, Dordrecht. 2007. https://doi.org/10.1007/978-1-4020-4423-6_114

[Lowes, 1994] Lowes, F. J. “The geomagnetic eccentric dipole: facts and fallacies,” Geophysical Journal International, Volume 118, Issue 3, September 1994, Page 671-679, https://doi.org/10.1111/j.1365-246X.1994.tb03992.x

[Mares et al., 1991]. Mares, V., Schraube, G., Schraube, H. “Calculated neutron response of a Bonner sphere spectrometer with ^{3}He counter,” Nuclear Instrumentation and Methods in Physics Research Section A, Volume 307, Issues 2-3, Pages 398-412. 1991. https://doi.org/10.1016/0168-9002(91)90210-H

[Mares et al., 1998]. Mares, V., Sannikov, A., Schraube, H. “The response functions of a ^{3}He-Bonner spectrometer and their experimental verification in high energy neutron fields,” SATIF-3 Proceedings, Sendai, Japan, Pages 237-248. 1998. https://www.oecd-nea.org/upload/docs/application/pdf/2019-12/826-satif-3.pdf

[Mares et al., 2020]. Mares, V. et al. “Influence of environmental parameters on secondary cosmic ray neutrons at high-altitude research stations at Jungfraujoch, Switzerland, and Zugspitze, Germany,” Radiation Physics and Chemistry, Volume 168. March 2020. https://doi.org/10.1016/j.radphyschem.2019.108557

[Mashnik et al., 2017] Mashnik, S.G., Kerby, L.M., et al. "Production of Energetic Light Fragments in CEM, LAQGSM, and MCNP6," Physical Review C, Volume 95, Issue 3. 2017. LA-UR-16-24713

[Matthiä et al., 2013] Matthiä, D., Berger, T., Mrigakshi, A., Reitz, G. “A ready-to-use galactic cosmic ray model,” Advances in Space Research, Volume 51, Issue 3, Pages 329-338, ISSN 0273-1177, 2013. https://doi.org/10.1016/j.asr.2012.09.022.

[Mészáros, 2006] Mészáros P. “Gamma-ray bursts. Reports on Progress in Physics,” Volume 69, Number 8. 2006. https://doi.org/10.1088/0034-4885/69/8/R01

[Miroshnichenko and Nymmik, 2013] Miroshnichenko L.I. and Nymmik R.A. “Extreme fluxes in solar energetic particle events: Methodological and physical limitations,” Radiation Measurements, Volume 61, Pages 6-15. 2013. https://doi.org/10.1016/j.radmeas.2013.11.010

[Nagpal and Samdani, 2017] Nagpal, L. and Samdani, K. "Project Loon: Innovating the connectivity worldwide," 2017 2nd IEEE International Conference on Recent Trends in Electronics, Information & Communication Technology (RTEICT), Bangalore, Pages 1778-1784. 2017. 10.1109/RTEICT.2017.8256905

[Nakamura, 2008] Nakamura, T. “Cosmic-ray Neutron Spectrometry and Dosimetry,” Journal of Nuclear Science and Technology, Volume 45, Issue sup5, Pages 1-7. 2008. https://doi.org/10.1080/00223131.2008.10875772

[Neddermeyer and Anderson, 1937] Neddermeyer, S. and Anderson, C. “Note on the Nature of Cosmic-Ray Particles,” Physics Review, Volume 51, Issue 10, Pages 884-886. 1937. https://link.aps.org/doi/10.1103/PhysRev.51.884

[NOAA, 1976] NOAA, NASA, and USAF (National Oceanic and Atmospheric Administration, National Aeronautics and Space Administration, and United States Air Force). U.S. Standard Atmosphere, 1976. NOAA-S/T 76-1562. Washington, DC: NOAA; 1976.

[NOAA, 2020] NOAA (National Oceanic and Atmospheric Administration). Geomagnetic Calculators, Maps, Models and Software. 2020. https://www.ngdc.noaa.gov/geomag/models.shtml

[Nowicki et al., 2017] Nowicki, S., Wender, S., Mocko, M. “The Los Alamos Neutron Science Center Spallation Neutron Sources,” Physics Procedia, Volume 90, Pages 374-380, ISSN 1875-3892. 2017. https://doi.org/10.1016/j.phpro.2017.09.035.

[Norman et al., 2016] Norman R.B., Mertens C.J., Slaba T.C. “Evaluating galactic cosmic ray environment models using RaD-X flight data,” Space Weather, Volume 14, Issue 10. 2016.

[Oehler et al., 2018] Oehler, J., Rouxel, D. & Lequentrec-Lalancette, M. “Comparison of global geomagnetic field models and evaluation using marine datasets in the north-eastern Atlantic Ocean and western Mediterranean Sea,” Earth Planets Space, Volume 70, Article number 99, 2018. https://doi.org/10.1186/s40623-018-0872-y

[O’Neill et al., 2015] O'Neill, P., Golge, S., Slaba, T. “Badhwar - O’Neill Galactic Cosmic Ray Flux Model Description,” Technical Report TP-2015-218569, NASA Technical Report, 2015.

[Owens and Forsyth, 2013] Owens, M.J., Forsyth, R.J. “The Heliospheric Magnetic Field,” Living Reviews in Solar Physics, Volume 10, Issue 5. 2013. https://doi.org/10.12942/lrsp-2013-5

[Parker, 1958] Parker, E.N., 1958, “Dynamics of the Interplanetary Gas and Magnetic Fields,” Astrophysics Journal, Volume 128, Pages 664–676. 1958.

[Parker, 1964] E.N. Parker, “Theory of streaming of cosmic rays and the diurnal variation,” Planetary and Space Science, Volume 12, Issue 8, Pages 735-749, ISSN 0032-0633. 1964. https://doi.org/10.1016/0032-0633(64)90054-6.

[Perey, 1979]. Perey, F. “Spectrum Unfolding by the Least-Squares Method,” (IAEA-TECDOC--221). International Atomic Energy Agency (IAEA). 1979. https://www.osti.gov/servlets/purl/5207996

[The Pierre Auger Collaboration, 2007] The Pierre Auger Collaboration. “Correlation of the Highest-Energy Cosmic Rays with Nearby Extragalactic Objects,” Science, Volume 318, Issue 5852, Pages 938-943. 2007. https://doi.org/10.1126/science.1151124

[The Pierre Auger Collaboration, 2015] The Pierre Auger Collaboration. “The Pierre Auger Cosmic Ray Observatory,” Nuclear Instruments and Methods in Physics Research Section A: Accelerators, Spectrometers, Detectors and Associated Equipment. Volume 798, Pages 172-213. 2015. http://dx.doi.org/10.1016/j.nima.2015.06.058

[The Pierre Auger Collaboration, 2017] The Pierre Auger Collaboration. “Observation of a large-scale anisotropy in the arrival directions of cosmic rays above 8×10^{18} eV,” Science, Volume 357, Issue 6357, Pages 1266-1270. 2017. 10.1126/science.aan4338

[Pishro-Nik, 2014] Pishro-Nik, Hossein. “Introduction to Probability, Statistics, and Random Processes.” Kappa Research, LLC. 2014.

[Rao, 1998] Rao, M. V. S. and Sreekantan, B. V. “Extensive Air Showers,” World Scientific, Pages 1-5, 1998.

[Reames, 2020] Reams, D. “Solar Energetic Particles,” Second Edition. arXiv:2010.08517v2

[Regener, 1932] Regener, E. “Intensity of Cosmic Radiation in the High Atmosphere,” Nature, Volume 130, Page 364, 1932.

[Reginatto, 2010]. Reginatto, M. “Overview of spectral unfolding techniques and uncertainty estimation,” Radiation Measurements, Volume 45, Issue 10, Pages 1323-1329, ISSN 1350-4487. 2010. https://doi.org/10.1016/j.radmeas.2010.06.016

[Rochester and Butler, 1947] Rochester, G. and Butler, C. “Evidence for the Existence of New Unstable Elementary Particles,” Nature, Volume 160, Pages 855–857. 1947. https://doi.org/10.1038/160855a0

[Ross and Chaplin, 2019] Ross, E., Chaplin, W.J. “The Behaviour of Galactic Cosmic-Ray Intensity During Solar Activity Cycle 24,” Solar Physics, Volume 294, Issue 8. 2019. https://doi.org/10.1007/s11207-019-1397-7

[Rossi and Zaider, 1996] Rossi, H. H. and Zaider, M. “Microdosimetry and Its Applications.” 1996.

[Russell, 1990]. Russell, G. “Spallation Physics: An Overview. 11th Meeting of the International Collaboration on Advanced Neutron Sources,” Pages 291-299. 1990. https://inis.iaea.org/collection/NCLCollectionStore/_Public/23/015/23015552.pdf

[Schraube et al., 1997]. Schraube, H., et al. “The Cosmic Ray Induced Neutron Spectrum at the Summit of the Zugspitze,” Radiation Protection Dosimetry, Volume 70, Issues 1-4, Pages 405-408. 1997.

[Shultis and Faw, 2011] Shultis, J.K. and Faw, R.E. “An MCNP Primer.” 2011. http://krex.ksu.edu

[Smart and Shea, 1985] Smart D.F. and Shea M.A. “Galactic Cosmic Radiation and Solar Energetic Particles,” In Handbook of Geophysics and the Space Environment. Edited by Jursa, Adolph S. Air Force Geophysics Laboratory, Air Force Systems Command, United States Air Force, 1985.

[Smart and Shea, 1990] Smart D.F. and Shea M.A. “A summary of major solar particle events,” Sun in Time Conference, Tucson, AZ. Solar Physics (ISSN 0038-0938), Volume 127, Pages 297-320. 1990.

[Smart and Shea, 2005] Smart D.F. and Shea M.A. “A review of geomagnetic cutoff rigidities for earth-orbiting spacecraft,” Advances in Space Research, Volume 36, Issue 10, Pages 2012-2020, ISSN 0273-1177. 2005. https://doi.org/10.1016/j.asr.2004.09.015.

[Smart and Shea, 2003] Smart D.F. and Shea M.A. “The limitations of using vertical cutoff rigidities determined from the IGRF magnetic field models for computing aircraft radiation dose,” Advances in Space Research, Volume 32, Issue 1, Pages 95-102, ISSN 0273-1177. 2003. https://doi.org/10.1016/S0273-1177(03)90375-9.

[Solanki et al., 2000] Solanki, S. K., Schussler, M., and Fligge, M. “Evolution of the Sun's large-scale magnetic field since the Maunder minimum,” Nature, Volume 408, Pages 445-447. 2000. https://doi.org/10.1038/35044027

[SILSO, 2020] Sunspot data from the World Data Center SILSO, Royal Observatory of Belgium, Brussels, 2020. http://www.sidc.be/silso/datafiles

[Sutton et al., 2000] Sutton, M., Hertel, N., Waters, L. “A High-Energy Neutron Depth-Dose Experiment Performed at the LANSCE/WNR Facility.” Proceedings of the Fifth Meeting of the Task Force on Shielding Aspects of Accelerators, Targets and Irradiation Facilities. Paris, France. 2000.

[Stassinopoulos, 1987] Stassinopoulos, E. G. “The Earth’s Trapped and Transient Space Radiation Environment,” In: McCormack P.D., Swenberg C.E., Bücker H. (eds) Terrestrial Space Radiation and Its Biological Effects. Nato ASI Series (Series A: Life Sciences), Volume 154. Springer, Boston, MA. https://doi.org/10.1007/978-1-4613-1567-4_2

[Tanabashi et al., 2018] Tanabashi M. et al. Particle Data Group. Phys. Rev. D 98, 030001. 2018. http://pdg.lbl.gov

[Taylor, 1997] Taylor, John. “An Introduction to Error Analysis: The Study of Uncertainties in Physical Measurements.” 2nd Edition. University Science Books. 1997.

[Taylor et al., 2015] Taylor, G., Hawkes, N., Shippen, A. “Accurate Simulations of TEPC Neutron Spectra Using Geant4,” Radiation Physics and Chemistry. 2015.

[Thébault et al., 2015] Thébault, E., Finlay, C.C., Beggan, C.D. et al. “International Geomagnetic Reference Field: the 12th generation,” Earth Planet Volume 67, Article number 79. 2015. https://doi.org/10.1186/s40623-015-0228-9

[Thomas and Alevra, 2002]. Thomas, D.J., Alevra, A.V. “Bonner Sphere Spectrometers – A Critical Review,” Nuclear Instruments and Methods in Physics Research Section A: Accelerators, Spectrometers, Detectors and Associated Equipment. Volume 476, Issues 1-2, Pages 12-20. 2002. https://doi.org/10.1016/S0168-9002(01)01379-1

[Tsoulfanidis , 1995] Tsoulfanidis, Nicholas. “Measaurement and Detection of Radiation,” 2nd Edition. Tylor & Francis. 1995.

[Waters, 2020] Waters, Laurie. Los Alamos National Labs (retired), 2020. Personal communication.

[Weili and Watanabe, 2011] Weili, S. and Watanabe, Y. “Status of JENDL High Energy File, Journal of the Korean Physical Society,” Volume 59 (2), Pages 1040-1045. 2011. https://www-nds.iaea.org/exfor/endf.htm

[Wender et al., 2019] Wender, S., O'Donnell, J., Zavorka, L., and Bhuva, B. "Neutron Beam Attenuation Through Semiconductor Devices During SEU Testing," 2019 IEEE International Reliability Physics Symposium (IRPS), Monterey, CA, USA, Pages 1-4. 2019.

[Werner, 2017] Werner, C.J.(editor). "MCNP Users Manual - Code Version 6.2", LA-UR-17-29981 (2017).

[Whalen et al., 1991] Whalen D. J., Cardon D. A., Uhle J.L, and Hendricks J.S., "Neutron Benchmark Problems", 1991. LA-12212

[Wilcox, 2014] Wilcox, T. "MCNP6 Advanced Tallies Tutorial", ANS RPSD-2014, LA-UR-14-27128 (2014).

[X-5 Monte Carlo Team, 2003] X-5 Monte Carlo Team, “MCNP – A General N-Particle Transport Code, Version 5” Volume I: Overview and Theory, 2003. LA-UR-03-1987

[Zaczyk, 2013] Zaczyk, I., “Impact of Cosmic Radiation on Aviation Reliability and Safety,” Journal of Applied Engineering Science, Volume 11, Issue 4, Pages 217-223, Belgrade, Serbia. 2013.

VITA

Paul Edward Inman

Candidate for the Degree of

Doctor of Philosophy

Dissertation: MODELING THE IONIZING RADIATION ENVIRONMENT IN EARTH'S ATMOSPHERE

Major Field: Physics

Biographical:

Education:

Completed the requirements for the Doctor of Philosophy in Physics at Oklahoma State University, Stillwater, Oklahoma in May, 2021.

Completed the requirements for the Master of Science in Medical Physics at the University of Oklahoma Health Sciences Center, Oklahoma City, Oklahoma in August, 2016.

Completed the requirements for the Bachelor of Science in Physics and Mathematics at Oklahoma Baptist University, Shawnee, Oklahoma in 2014.